Title	Study on the Heat and Electron Transport Properties of Tungsten Oxide Films with Various Atomic Arrangements
Author(s)	金, 高韻
Citation	北海道大学. 博士(工学) 甲第14725号
Issue Date	2021-09-24
DOI	10.14943/doctoral.k14725
Doc URL	http://hdl.handle.net/2115/83220
Type	theses (doctoral)
File Information	Gowoon_Kim.pdf

Study on the heat and electron transport properties of tungsten oxide films with various atomic arrangements

By

GOWOON KIM

A dissertation submitted as a requirement for the degree of
Doctor of Philosophy in Engineering

Hokkaido University
Graduate School of Information Science and Technology

September 2021

Contents

List of Figures

List of Tables

List of Acronyms

AFM	Atomic forced microscopy
DOS	Density of states
ZT	Thermoelectric figure of merit
FWHM	Full width half maximum
HRXRD	High-resolution X-ray diffraction
LA	Longitudinal acoustical mode
LO	Longitudinal optical mode
1D	One-dimensional
P_{O2}	Partial oxygen pressure
PVD	Physical vapor deposition
PLD	Pulsed laser deposition
RHEED	Reflection high-energy electron Diffraction
RT	Room temperature
TDTR	Time-domain thermoreflectance
TEY	Total electron yield
TMO	Transition metal oxide
Trans.	Transmission
TA	Transverse acoustic mode
TO	Transverse optical mode
WO_x	Tungsten oxide
XANES	X-ray absorption near edge structure
XAS	X-ray absorption spectroscopy
XRD	X-ray diffraction
XLD	X-ray linear dichroism
XPS	X-ray photoelectron spectroscopy
XRR	X-ray reflectivity
YSZ	yttria-stabilized zirconia

List of Symbols

α	Absorption coefficient
E_a	Activation energy
θ	Angle
k_B	Boltzmann constant
n	Carrier concentration
T_c	Critical temperature
I	Current
J	Current density
E	Electric field
σ	Electrical conductivity
e	Electron charge
m^*	Effective mass
E	Energy
E_F	Fermi energy
ε	Free energies
C_p	Heat capacity per unit volume
j	Heat flux
U	Hubbard term
n	Integral
d	Interplanar distance
L	Lorenz factor
μ	Mobility
ω	Phonon frequency
υ	Phonon group velocity
l	Phonon mean free path
R	Reflectance
τ	Relaxation time

γ	Repeat distance force constant
R	Resistance
ρ	Resistivity
S	Seebeck coefficient, Thermopower
a	Spacing between planes
T	Temperature
ΔT	Temperature difference
κ	Thermal conductivity
ΔV	Thermo-electromotive force
d	Thickness
t	Time
Q	Transferred electron charge
A	Transport constant

Chapter 1. General Introduction

1.1 Background of thermal management technology

Today, utilizing waste heat has attracted attention as a way of achieving renewable cycle of energy, and research on energy recycling using waste heat is steadily increasing as shown in **Figure 1-1**. In modern devices and energies, less than 1/3 of primary energy is used, and the rest of energy is dissipated as waste heat. [1] For instance, in electronic circuits, the heat sink and Peltier device are used since the heat generated in densely packed integrated circuits in electronic devices causes malfunction and even failure. Thus, the heat is thrown away without any use. If such heat can be effectively reused as source energy, it is possible to reduce energy loss and create more sustainable uses of energy. For example, storing the waste heat and transporting the stored heat using a thermal circuit to convert heat into electric energy using a thermoelectric conversion technique or provide heating at later times. Such thermal management technology can be used to illuminate light or warm water at night. It can be of great use in places with a large temperature gap between day and night.

By definition, thermal management technology refers to all disciplines of technologies associated with controlling heat and converting heat into other forms of energy. However, unlike electrical energy, thermal energy is externally difficult to control, which is the main challenge in thermal management technologies. There are three typical thermal circuit components in thermal management technologies; thermal diode, regulator, and switch (**Figure 1-2**). [2] When a temperature difference (ΔT) is introduced to across a material, heat flows from the hot side to the cold side. Thermal diode allows that heat to flow one-way, which consists of two different materials with different temperature dependent thermal conductivity (κ) as shown in **Figure 1-2(a)**. [3] When the material on left is hotter than the material on right, heat will flow easily from left to right, but when the material on right is hotter than the material on left, heat will not significantly flow from the right to left. Thermal regulators regulate the flow of heat. A material that has a high heat conduction state and low heat conduction state between a critical temperature (T_c) is used. [4] For example, metal (high heat conduction state) – insulator (low heat conduction state) phase transition can be used, which can regulate the heat flow (**Figure 1-2(b)**). [5,6] In the case of thermal switch, it generates an "On (high κ)" state and a "Closed (low κ)" state by externally applied stimuli such as electric and magnetic fields [7-10]. (**Figure 1-2(c)**) This switching behavior can be applied to transistors structure, and κ of the active layer can be modulated by applying the stimuli controlling the heat flow. [11] By using such thermal elements, heat can be stored at a desired time, and the stored heat can be transported at will. [12]

Furthermore, in order to convert this stored heat into electricity, thermoelectric energy conversion technology is necessary. [13,14] Thermoelectric devices utilize electromotive power generated by temperature gradients in a material, which has the advantage of not generating harmful by-products in the energy conversion process. In addition, the structure is simple, and the size can be easily adjusted. The performance of thermoelectric conversion can be expressed by a dimensionless Figure of merit $ZT = S^2\sigma T/\kappa$, where S and σ are Seebeck coefficient (= Thermopower) and electrical conductivity, respectively. [15] If you have large ZT thermoelectric materials, you can generate a lot of electricity using waste heat. In order to find good thermoelectric materials, it is necessary to find material that has a low κ, high S and σ. For these reasons, materials exhibiting coupled electrical, chemical, magnetic, and thermal properties are essential for thermal circuit components and thermoelectric energy conversion.

1.2 Transition metal oxides (TMOs)

TMO is one of the most interesting materials that exhibit a wide-range of structural-chemical-physical properties, such as, high temperature superconductivity [16], giant Seebeck coefficient [17], quasi 1D σ [18], multiferroicity [19], and metal-insulator transition [20]. TMOs are also used as the active material for electrochemical oxidation/reduction or protonation/de-protonation. [21] These exotic properties are strongly related to the correlation between the number of degrees of freedom in spin, charge, orbital, and lattice. [22] Therefore, in order to understand the origin of versatile physical properties of TMOs, it is important to understand interplay of spin, charge, and orbital, which strongly depends on the atomic arrangement in the lattice.

1.2.1 Electrical properties of TMOs

Drude model is the simple model for explaining the electron transport in materials such as metal, conductor oxide, and heavily doped semiconductors. [23] This model assumes that materials consist of motionless cations and a non-interacting free electron gas, and the free electrons are elastically scattered by immobile cations and other electrons. The collective kinetic motion can be described by current density J and electric field E.

$$J = \sigma \mathrm{E};\ \sigma = \frac{ne^2\tau}{m^*} = ne\mu$$

where, n, e, τ, m^* and μ are carrier concentration, electron charge, relaxation time, electron effective mass and mobility, respectively. In the case of TMOs, n is determined by the outer d orbitals of transition metals, while μ is affected by electron-phonon scattering, electron-electron scattering, grain boundaries, impurities, defects, and so on.

In electrical properties of TMOs, it is essential to understand of the outer d electrons. According to the number of d electrons and Fermi level (E_F), TMOs categorize from class 1 to 4 as shown in **Figure 1-3**. [24,25] TMOs with completely empty d-bands (d^0) are categorized as class 1, which are insulators. But when they have oxygen vacancies, oxygen defect level appears, and the TMOs usually shows n-type semiconductor property. When the d-bands are partially filled with low number of electrons (d^1, d^2 and d^3), it categorizes as class 2, which tends to originated from chemically reduced d^0 oxides and mostly exhibit metallic properties. When d-band is partially filled with the high number of electrons (d^7, d^8 and d^9), it categorizes as class 3. These oxides are called as Mott-Hubbard or charge-transfer insulator. (**Figure 1-4(a)**) Because of strong electron-electron correlation, its electronic property is not correctly predicted by using the simple independent-electron model. According to class 1and 2, these oxides should be a metallic but are electrical insulators. This Mott-Hubbard insulating property is mostly observed in 3d TMOs that have narrow d orbitals, which is explained by electron-electron repulsion and electron exchange interactions. Furthermore, strong electron-electron correlation can also turn TMOs into Charge-Transfer insulators. (**Figure 1-4(b)**) Unlike the Mott-Hubbard insulator, where the lowest energy-excitation arises from electrons hopping between d-bands, the lowest energy-excitation of Charge-Transfer insulator arises from electron hopping from O 2p to d-band. Therefore, the Hubbard term (U) of Charge-Transfer insulator is greater than Mott-Hubbard insulator. When d-bands are fully occupied (d^{10}), it categorizes as class 4. In this case, the TMO shows semiconductor property because of the bandgap between the d-band and the next-highest energy level (metal *s*-band). Since the E_F is located near the valence band, it is mostly p-type semiconductor.

In TMOs, due to the crystal field splitting, metal and oxide ions are considered as simple point charges. For example, in perovskite TMOs, oxide ions are located at the vertices of the octahedron and surround the transition metal cation. When there is no charge nearby the transition metal ion, five d-orbitals have degenerated states (same energy level). However, when d-orbitals approach oxide ions, the Coulomb repulsion becomes stronger. Based on the distance between metal ions and oxide ions, 5 degenerate d-orbitals are broken into 3 t_{2g} orbitals (d_{xy}, d_{yz}, d_{xz}) and 2 e_g orbitals (d_{z2}, d_{x2-y2}). The d electrons are filled from the low to high orbital level, following the Hund's rule. Since the crystal field splitting occurs differently in the different crystal structures, the atomic arrangement in TMOs plays important role in their physic properties.

1.2.2 Thermal properties of TMOs

Thermal conductivity (κ) is the ratio between heat flux (j) and temperature gradient ($\nabla \vec{T}$). According to Fourier's Law, heat flux can be described as follow equation.

$$j = -\kappa\, (\nabla \vec{T})$$

Except for special occasions [26], thermal energy is transported by quantized lattice vibration (phonon) and free electrons. As such, κ consists of contribution from electrons and phonons. Generally, κ_{phonon} is determined by experimentally obtained κ_{total} and calculated κ_{electron}.

$$\kappa_{\text{total}} = \kappa_{\text{electron}} + \kappa_{\text{phonon}}$$

The electronic contribution can be estimated from the σ through the Wiedmann-Franz law.

$$\kappa_{\text{electron}} = L\sigma T = ne\mu LT$$

where L and T are Lorenz factor (2.4×10^{-8} J^2 K^{-2} C^{-2}) and temperature, respectively. Heat in metals is predominately carried by free electrons, and this is why metals are considered as good heat conductors. On the other hand, in insulators or semiconductors, as they rarely have free electrons, heat is predominantly carried by phonons. Unlike metal, in the case of TMOs, phonons mostly transfer heat. Therefore, understanding nature of phonon transportation is very important.

Phonons refer to collective displacements of atoms in a lattice. Based on the direction of wavevector ($\vec{k}$), one mode of longitudinal displacements and two modes of transverse displacements are generated for polarization mode, the dispersion relation (ω versus k) develops two types of branches, known as the acoustical and optical branches (**Figure 1-5(a)**). In the case of a two-atom system with atomic masses M_1 and M_2, phonon dispersion is described as follow. [23]

$$\omega^2 = \gamma\left(\frac{1}{M_1}+\frac{1}{M_2}\right) \pm \gamma\left[\left(\frac{1}{M_1}+\frac{1}{M_2}\right)^2 - \frac{4}{M_1M_2} - sin^2\frac{ka}{2}\right]^{1/2}$$

where γ and *a* are repeat distance force constant, spacing between planes. For *ka* is very small (*ka* << 0),

$$\omega^2 \cong 2\gamma\left(\frac{1}{M_1}+\frac{1}{M_2}\right)^2 : optical\ branch$$

$$\omega^2 \cong \gamma\frac{\frac{1}{2}}{M_1M_2}k^2a^2 : acoustic\ branch$$

For *ka* = ± *π* (Brillouin zone boundary)

$$\omega^2 \cong \frac{2\gamma}{M_1}\ or\ \frac{2\gamma}{M_2}$$

If the two atomic displacement is out of phase (**Figure 1-5 (c)**), this motion can be excited by the electric field from a light wave and therefore, branch is called the optical branch. If the two atomic displacements are in-phase **(Figure 1-5 (d)**), they behave like long-wavelength acoustical vibrations, therefore, the branch is called the acoustic branch. The total number of degree of freedom is 3p where p is atoms/primitive unit cell. 3 of modes are associated with the acoustic modes, and 3(p-1) are associated with the optical modes.

(**Figure 1-5(b)**) For example, if there are two atoms in a one primitive cell, total six modes are generated: one longitudinal acoustical (LA) and one longitudinal optical (LO) mode, and two transverse acoustic (TA) and two transverse optical (TO) modes. Phonons in the acoustic branch largely dominate the phonon heat transport, it due to their fast phonon group velocity. On the other hand, their optical phonons have small contributions in phonon heat transport because of their low phonon group velocity. TMOs always have optical branches, and optical phonons in TMOs strongly scatters charge carriers since anion and cation motions are out of phase, which creates strong electric fields. Electron contribution in the κ of TMOs is usually low, unless the n is comparable to metals, and the κ of TMOs is mostly attributed to phonons.

Since engineering κ in materials is usually achieved by controlling phonon scatterings, phonons can be scattered by external factors such as defects, dislocations, grain boundary, which also have a significant impact on κ. In a simple form, the role of phonon transport properties in κ can be described by the following equation. [23]

$$\kappa_{phonon} = \frac{1}{3}\int C_p(\omega) \cdot v(\omega) \cdot l(\omega) d\omega$$

where, C_p, υ, l and ω are heat capacity, phonon group velocity, phonon mean free path, and phonon frequency, respectively. There are generally three types of phonon scattering: grain boundary (l_{GB}), impurity (l_i) and phonon-phonon interactions (l_{ph}). The effective mean free path l_{eff} is described based on Matthiessen's rule by the following equation. [27]

$$\frac{1}{l_{eff}} = \frac{1}{l_{GB}} + \frac{1}{l_i} + \frac{1}{l_{ph}}$$

At low temperature, grain boundary scattering is dominant, and κ usually follows the Deby's T^3 law. As the temperature increases, phonons will be scattered by defects, dislocations. Impurity scattering is usually the dominant near the peak of thermal conductivity. At high temperature, Umklapp and phonon-phonon scatterings are dominants, and κ is usually inversely proportional to temperature ($\sim 1/T$). While these scattering mechanisms exhibit different temperature dependences, they are all strongly affected by the crystal structures. Consequently, in order to understand the electron and phonons transport in TMOs, it is very important to understand the effect of atomic arrangements.

1.2.3 Tungsten oxides

As mentioned above, phonon and electron transport properties in TMOs are greatly affected by the atomic arrangement. In order to investigate the electron and phonon transport with various atomic arrangement, a material system that can change the atomic structure without changing its stoichiometry is required. Tungsten oxide is selected as an excellent material system from this point of view. Tungsten oxide (WO_x) is one of TMOs with wide bandgap, and this material has been receiving a lot of attention as the active material for many functional applications such electrochromic device [28], electrode of Li-ion batteries [29], and gas sensors [30]. In particular, amorphous WO_x is the most famous active material among commonly used electrochromic devices. However, most of research are concentrated on the electrochromic property of amorphous WO_x, and research on phonon and electron transport properties of WO_x with various atomic arrangement is still rare.

Figure 1-6(a) shows different forms of tungsten oxide crystals. [31] Stoichiometric tungsten trioxide (WO_3) has a ReO_3 type monoclinic structure ($P2_{1/c}$, $a/2 = 0.385$ nm, $b/2 = 0.377$ nm, $c/2 = 0.365$ nm, $\alpha = \gamma = 90°$ and $\beta = 90.88°$) from room temperature (RT) to 300°C. However, it is often regarded as pseudo-cubic ($a_{\mathrm{cubic}} = 0.373$ nm). (**Figure 1-6(b)**) In addition, tungsten oxide easily forms the oxygen vacancies. Reduction of monoclinic WO_3 leads to formation of a unique structure called the Magnéli phase ($x = 2.9$, 2.82, and 2.72) [32]. The sub-stoichiometric $WO_{2.9}$ is monoclinic ($P2/m$, $a = 12.05$ Å, $b = 7.76$ Å, $c = 23.59$ Å, $\alpha = \gamma = 90°$ and $\beta = 82.28°$), which is composed of both corner and/or edge-sharing WO_6 octahedra. Because of the oxygen vacancies, $WO_{2.9}$ exhibits enhanced σ. (**Figure 1-6(c)**) The crystal structure is also monoclinic ($P2/m$, $a = 18.31$ Å, $b = 3.79$ Å, $c = 14.04$ Å, $\alpha = \gamma = 90°$ and $\beta = 115.03°$), which is composed of both WO_6 octahedra and WO_7 bipyramids with pentagonal column and hexagonal 1D tunnel arrays. (**Figure 1-6(d)**) $WO_{2.72}$ is known as electrical conductor. Also, there is metastable hexagonal WO_3 ($P6_3cm$, $a = b = 7.45$ Å, $c = 7.764$ Å, $\alpha = \beta = 90°$ and $\gamma = 120°$), which has a quite unique crystal structure with empty hexagonal and trigonal tunnels. [33]

In general, the atomic arrangement of material is changed by changing the atoms, but tungsten oxide can easily change the structure by introducing oxygen vacancies. Furthermore, WO_3 has two possible phases: monoclinic WO_3 and hexagonal WO_3.

Therefore, WO_x is selected as an ideal material to clarify the relationship between atomic arrangement and heat/electron transport properties.

1.3 Objective of research

The aim of this doctoral research is to understand the heat and electron transport properties of WO_x films with various atomic arrangements. Three different structures were examined: amorphous WO_x films, 1D defect tunnel stabilized WO_x epitaxial films, and hexagonal WO_x epitaxial films. To achieve the research goal, amorphous WO_x and WO_x epitaxial films were fabricated by using pulsed laser deposition technique, and the x of both amorphous and epitaxial WO_x films was systematically changed. Then, the resulting atomic arrangements were observed, and their electron and heat transport properties were clarified. The results of this research will provide the heat and electron transport properties of tungsten oxide films with various atomic arrangements for developments of WO_x based future applications.

This thesis is organized in the following way. In chapter 1, the background and objective of this research are introduced. In chapter 2, the experimental procedure for this research is described. In chapter 3 is about the low thermal conductivity properties of amorphous WO_x films, where the electrical, optical, and thermal properties of amorphous WO_x films are systematically clarified. [34] In chapter 4, the realization of low thermal conductivity and high σ in WO_x epitaxial films is examined, and the fundamental transport mechanism of 1D defect tunnels is addressed. [35] In chapter 5, anisotropy of σ in WO_x

films with 1D atomic defect tunnel structure is examined and the origin of this anisotropy electron transport is clarified. [36] In chapter 6, the reversible redox reaction of hexagonal WO_x was modulated. [37] Finally, in chapter 7, the present study is summarized.

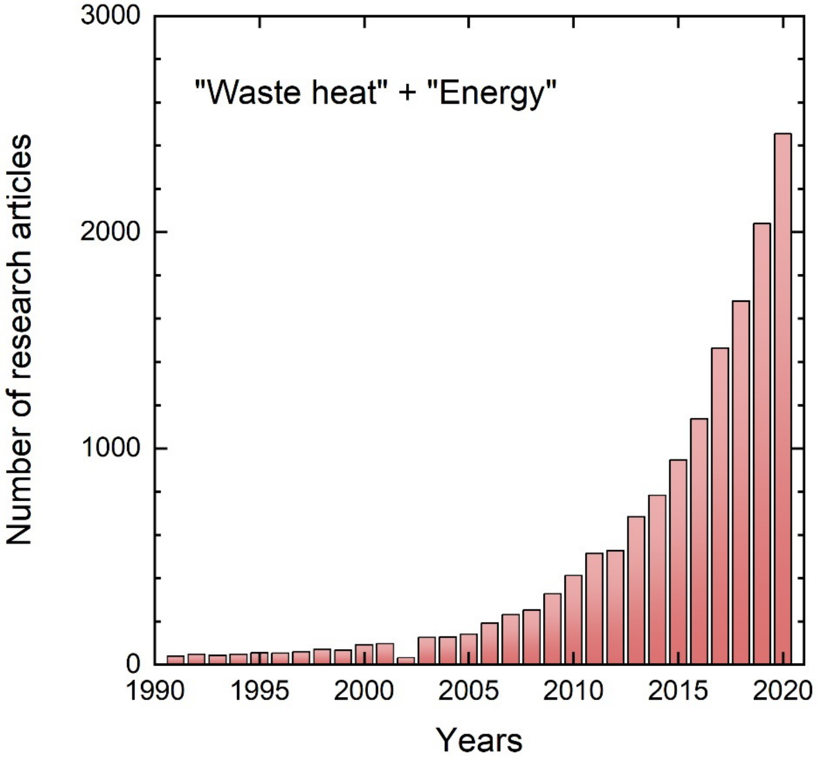

Figure 1-1. The number of research articles from 1990-2020, obtained with the keyword “Waste heat” and “Energy” based on a Web of Science search.

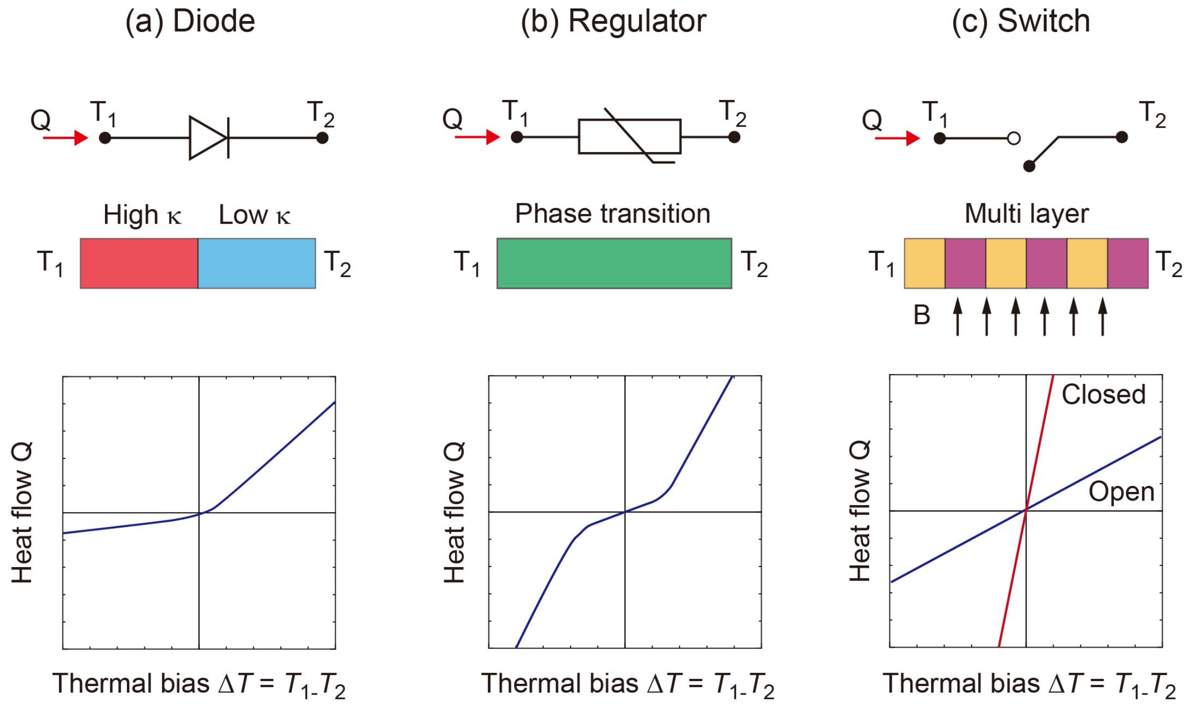

Figure 1-2. Thermal components and transfer function of (a) thermal diode (b) thermal regulator and (c) thermal switch.

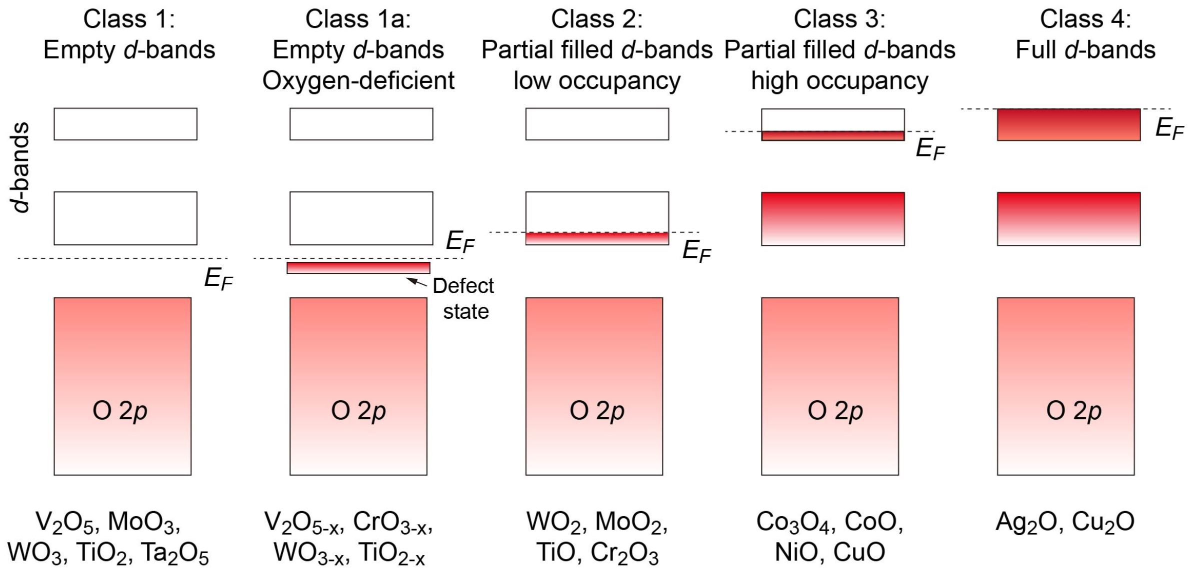

Figure 1-3. Schematic band diagrams of transition metal oxides. Class 1: Empty d-bands Class1a: Empty d-bands with oxygen deficient, Class 2: Partial filled d-bands with low occupancy. Class 3: Partial filled *d*-bands with high occupancy, Class 4: Fully filled d-bands. [24]

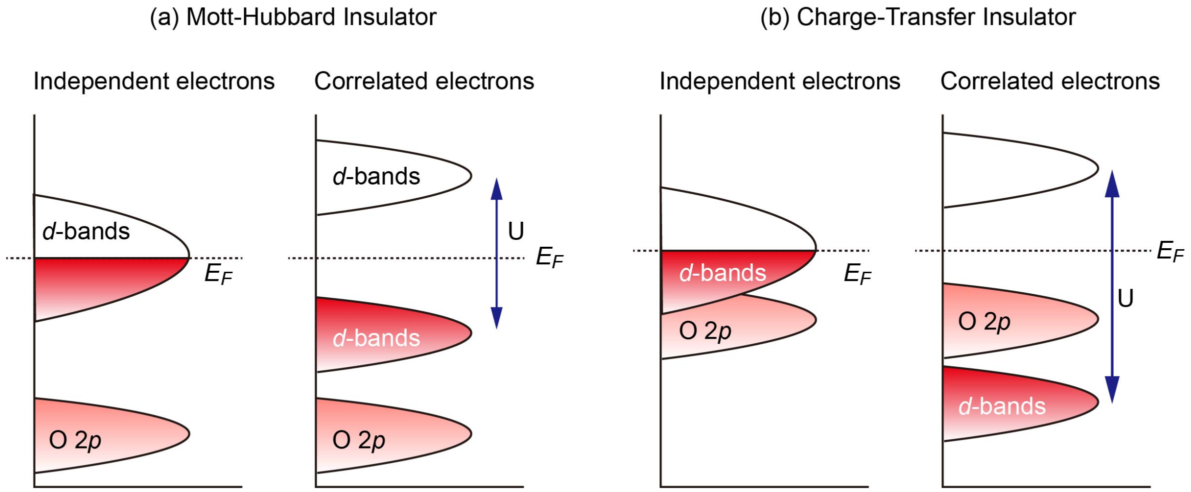

Figure 1-4. (a) Schematic band diagram of independent electron model (left) and Mott-Hubbard insulator (right). (b) Schematic band diagram of independent electron model (left) and Charge-Transfer insulator (right). [20]

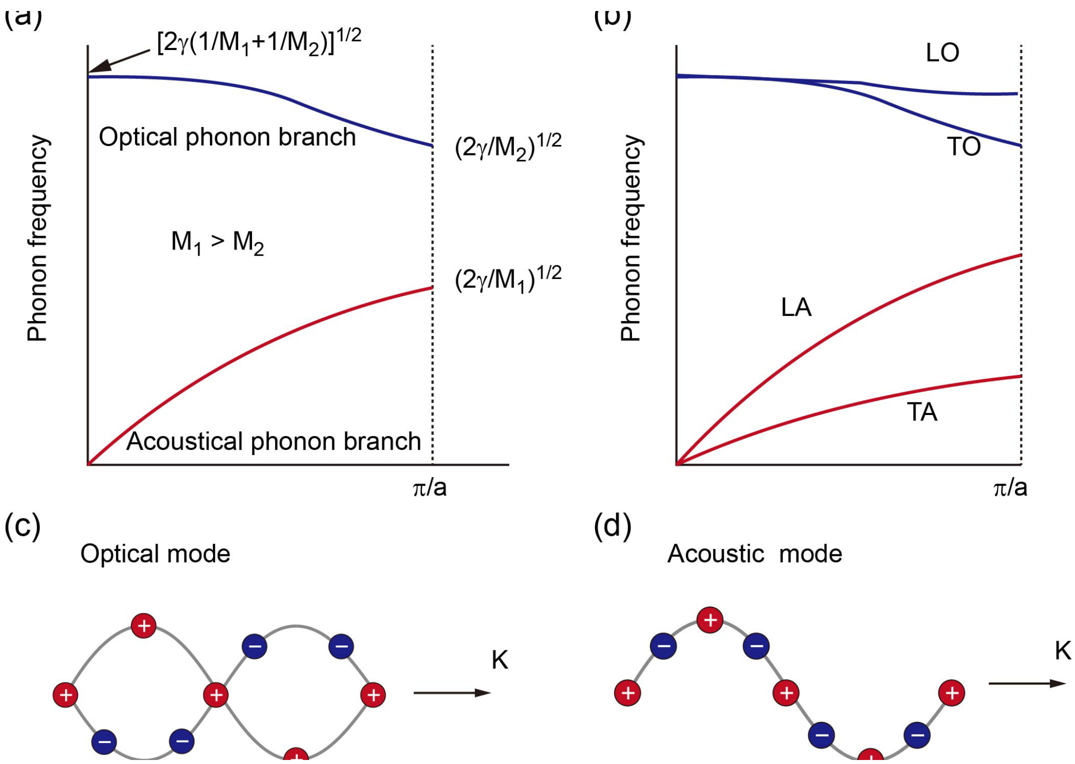

Figure 1-5. (a) Optical and acoustical phonon branches (b)Transverse acoustic (TA), longitudinal acoustic (LA) branches, Transverse optical (TO) and longitudinal optical (LO) phonon branches. (c) and (d) Optical and acoustic phonon waves in a diatomic linear lattice. [23]

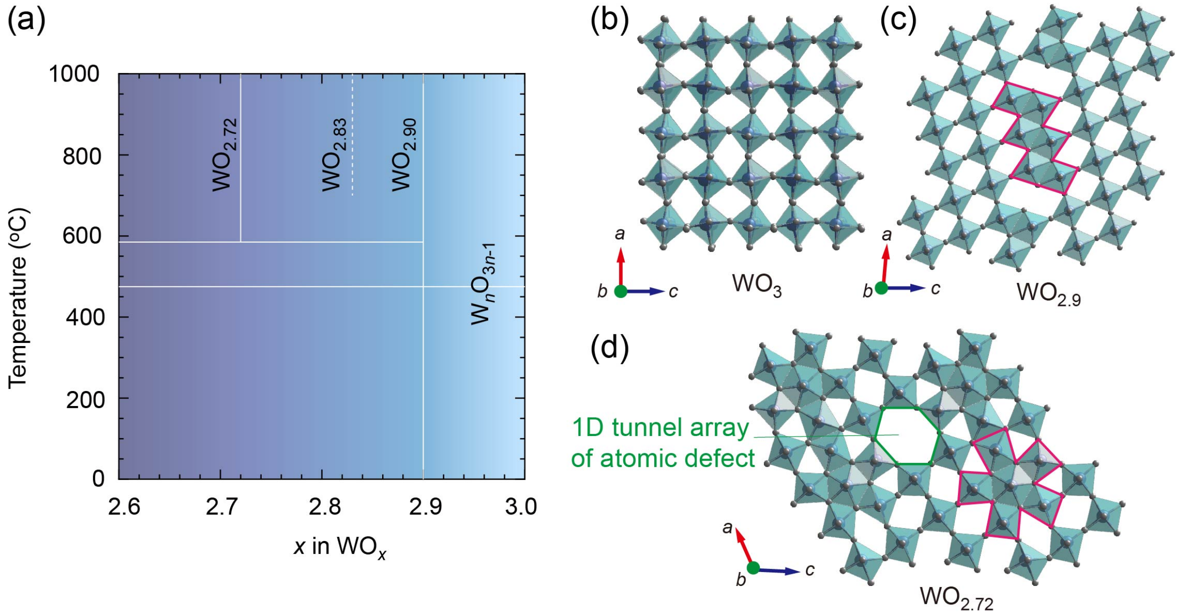

Figure 1-6. (a) Various crystal structure form of tungsten oxide. [31] Crystal structure of (b) WO_3 (c) $WO_{2.9}$ and (d) $WO_{2.72}$.

References

[1] K. Zeb, S. M. Ali, B. Khan, C. A. Mehmood, N. Tareen, W. Din, U. Farid, and A. Haider, *Renewable and Sustainable Energy Reviews* **75**, 1142 (2017).

[2] G. Wehmeyer, T. Yabuki, C. Monachon, J. Wu, and C. Dames, *Appl. Phys. Rev.* **4**, 041304 (2017).

[3] M. J. Martínez-Pérez, A. Fornieri, and F. Giazotto, *Nat. Nanotechnol.* **10**, 303 (2015).

[4] R. Shrestha, Y. Luan, S. Shin, T. Zhang, X. Luo, J. S. Lundh, W. Gong, M. R. Bockstaller, S. Choi, and T. Luo, *Sci. Adv.* **5**, eaax3777 (2019).

[5] T. Liu, J. W. Palko, J. S. Katz, E. M. Dede, F. Zhou, M. Asheghi, and K. E. Goodson, *Appl. Phys. Lett.* **115**, 254102 (2019).

[6] M. Hao, J. Li, S. Park, S. Moura, and C. Dames, *Nat. Energy* **3**, 899 (2018).

[7] J. Crossno, J. K. Shi, K. Wang, X. Liu, A. Harzheim, A. Lucas, S. Sachdev, P. Kim, T. Taniguchi, and K. Watanabe, *Science* **351**, 1058 (2016).

[8] J. F. Ihlefeld, B. M. Foley, D. A. Scrymgeour, J. R. Michael, B. B. McKenzie, D. L. Medlin, M. Wallace, S. Trolier-McKinstry, and P. E. Hopkins, *Nano Lett.* **15**, 1791 (2015).

[9] G. Cha, Y. S. Ju, L. A. Ahuré, and N. M. Wereley, *J. Appl. Phys.* **107**, 09B505 (2010).

[10] J. Kimling, R. Wilson, K. Rott, J. Kimling, G. Reiss, and D. G. Cahill, *Phys. Rev. B* **91**, 144405 (2015).

[11] A. Sood, F. Xiong, S. Chen, H. Wang, D. Selli, J. Zhang, C. J. McClellan, J. Sun, D. Donadio, and Y. Cui, *Nat. Commun.* **9**, 1 (2018).

[12] T. Swoboda, K. Klinar, A. S. Yalamarthy, A. Kitanovski, and M. Muñoz Rojo, *Adv. Electron. Mater.* **7**, 2000625 (2021).

[13] G. A. Slack and D. Rowe, *CRC handbook of thermoelectrics*, (CRC press Boca Raton, FL, 1995).

[14] H. J. Goldsmid, *Introduction to thermoelectricity*, (Springer, 2010).

[15] H. Goldsmid, *Thermoelectric refrigeration*, (Springer, New York, 1964).

[16] M.-K. Wu, J. R. Ashburn, C. Torng, P. H. Hor, R. L. Meng, L. Gao, Z. J. Huang, Y. Wang, and a. Chu, *Phys. Rev. Lett.* **58**, 908 (1987).

[17] H. Ohta, S. Kim, Y. Mune, T. Mizoguchi, K. Nomura, S. Ohta, T. Nomura, Y. Nakanishi, Y. Ikuhara, and M. Hirano, *Nat. Mater.* **6**, 129 (2007).

[18] G. Kim, Y. Q. Zhang, T. Min, H. Suh, J. H. Jang, H. Kong, J. Lee, J. Lee, T. Y. Jeon, and I. Lee, *Adv. Electron. Mater.*, 1800504 (2018).

[19] J. Heron, J. Bosse, Q. He, Y. Gao, M. Trassin, L. Ye, J. Clarkson, C. Wang, J. Liu, and S. Salahuddin, *Nature* **516**, 370 (2014).

[20] M. Imada, A. Fujimori, and Y. Tokura, *Rev. Mod. Phys.* **70**, 1039 (1998).

[21] T. Katase, K. Endo, T. Tohei, Y. Ikuhara, and H. Ohta, *Adv. Electron. Mater.* **1**, 1500063 (2015).

[22] Y. Tokura and N. Nagaosa, *Science* **288**, 462 (2000).

[23] C. Kittel, *Introduction to solid state physics*, (Wiley New York, 1976).

[24] M. T. Greiner, M. G. Helander, W.-M. Tang, Z.-B. Wang, J. Qiu, and Z.-H. Lu, *Nat. Mater.* **11**, 76 (2012).

[25] M. T. Greiner and Z.-H. Lu, *NPG Asia Materials* **5**, e55 (2013).

[26] A. Sologubenko, K. Gianno, H. Ott, U. Ammerahl, and A. Revcolevschi, *Phys. Rev. Lett.* **84**, 2714 (2000).

[27] G. Chen, *Nanoscale energy transport and conversion: a parallel treatment of electrons, molecules, phonons, and photons*, (Oxford university press, 2005).

[28] T. Onozato, Y. Nezu, H. J. Cho, and H. Ohta, *AIP Advances* **9**, 025122 (2019).

[29] W.-J. Li and Z.-W. Fu, *Appl. Surf. Sci.* **256**, 2447 (2010).

[30] X.-L. Li, T.-J. Lou, X.-M. Sun, and Y.-D. Li, *lnorg. Chem.* **43**, 5442 (2004).

[31] C. C. Mardare and A. W. Hassel, *Phys. Status Solidi A* **216**, 1900047 (2019).

[32] D. Migas, V. Shaposhnikov, and V. Borisenko, *J. Appl. Phys.* **108**, 093714 (2010).

[33] J. Besnardiere, B. Ma, A. Torres-Pardo, G. Wallez, H. Kabbour, J. M. González-Calbet, H. J. Von Bardeleben, B. Fleury, V. Buissette, and C. Sanchez, *Nat. Commun.* **10**, 1 (2019).

[34] G. Kim, H. J. Cho, Y.-M. Sheu, and H. Ohta, *J. Phys. Chem. C* **123**, 15419 (2019).

[35] G. Kim, B. Feng, Y.-M. Sheu, H. J. Cho, Y. Ikuhara, and H. Ohta, *ACS Appl. Electron. Mater.* **2**, 2507 (2020).

[36] G. Kim, B. Feng, S. Ryu, H. J. Cho, H. Jeen, Y. Ikuhara, and H. Ohta, *ACS Appl. Mater. Interfaces* **13**, 6864 (2021).

[37] G. Kim, H. J. Cho, and H. Ohta, *ACS Appl. Electron. Mater.* **XX**, XXX (2021).

Chapter 2. Experimental procedure

2.1 Pulsed laser deposition

Physical vapor deposition (PVD) method evaporates a solid target using a high energy source and deposit the material in forms of films on a substrate in vacuum. Among PVD techniques, pulsed laser deposition (PLD) is perhaps the most versatile method for growing high quality thin films. (**Figure 2-1(a)**) Usually, KrF excimer laser (λ= 248 nm) or third harmonics of Nd: YAG laser (λ= 355 nm) is used for the energy source. The detailed deposition mechanisms of PLD are very complex, but overall processes can be divided into four simple processes. [1]

1) High energy laser pulse is irradiated on the target surface. (Time (t) = 0)
2) Laser pulse vaporizes the target and creates a plasma plume. ($t \sim 0.1$ μs)
3) The plasma plume heads to substrate. ($t \sim 2$ μs)
4) Ablated plume reaches the substrate, where nucleation and film growth occur. ($t \sim 4$ μs)

The nucleation and growth of the film are strongly influenced by several parameters such as substrate temperature, oxygen pressure, laser fluence, laser wavelength, and lens position. Depending on these parameters and the respective thermodynamics, three growth mode are possible, as explained in the followings. The free energies of film surface, substrate surface, and interface are denoted by ε_f, ε_s, and ε_i, respectively. (**Figure 2-1(b)**)

1) Frank-van der Merwe mode ($\varepsilon_s > \varepsilon_f + \varepsilon_i$): layer-by-layer growth occurs when the lattice mismatch between substrate and film is small.

2) Volmer-Weber mode ($\varepsilon_s < \varepsilon_f + \varepsilon_i$): island growth occurs when the bonding between substrate and film is weak. In the case, the lattice mismatch between substrate and film is large.

3) Stranski-Krastanov mode ($\varepsilon_s < \varepsilon_f + \varepsilon_i$): layer-by-layer growth + island growth. Film is grown in the layer-by-layer mode due to strain and then grown in the island mode when the thickness of film exceeds a certain critical thickness.

In order to obtain a high-quality thin film, selection of the substrate and optimization of deposition conditions are very important since they can change the chemical and physical properties of film. Depending on the research objective, various types of films in single crystal (epitaxial), amorphous, and poly-crystal phases can be obtained. Therefore, PLD can be applied to various fields, including complex oxide film growth, epitaxial interface and superlattice fabrication, superconducting electronic devices, wide bandgap electronics, polymer and organic films, and biological film.

2.2 Reflection high-energy electron diffraction

Reflection high-energy electron diffraction (RHEED) is a technique for observing the smoothness and crystallinity of surfaces. The main advantage is the fact that *in-situ* monitoring is possible without air exposure. Hence, RHEED is generally used with PLD. This technique requires an electron gun and a photoluminescent detector screen. Generally, 10-50 keV of energy is applied to electron gun. Therefore, it can only be used in a high-vacuum to prevent the burning of the filament. A high-energy electron beam is incident on the film surface at a small angle of 1~5^{o}, and the electrons are scattered from the film surface, resulting in a characteristic diffraction pattern on the screen as shown in **Figure 2-2**. [2] This pattern contains a lot of information such as growth ratio, surface smoothness, surface reconstruction, rotational symmetry, crystallographic orientations, and in-plane lattice constants. For example, in the case of rotational symmetry, the RHEED pattern should be the same every 90 degrees when the film has a four-fold symmetry. When the film has a six-fold symmetry, the RHEED pattern is the same every 30 degrees (twin structure) or 60 degrees (no twin structure). Also, *in-situ* surface reconstruction can be observed. Therefore, the optimized growth condition of the film is relatively easy to find using RHEED.

2.3 X-ray diffraction

X-ray diffraction (XRD) is typically used to analyze the crystal structure, film thickness, density, and crystallographic orientation. XRD measurement is based on the Bragg's law [3]. There are parallel lattice planes that have a regular atomic arrangement with the interplanar distance d. When X-ray is incident on this plane with an angle θ, it is scatted by atomic planes with the reflection angle θ. (**Figure 2-3(a)**) The path difference in the X-rays reflected from adjacent planes is $2d \sin \theta$. Constructive interference of the radiation from successive planes occurs when the path difference is an integral (n) multiple of wavelength λ (Cu Kα1 ≈ 1.54059 Å). The Bragg's law can be expressed as the following (**Figure 2-3(b)**):

$$2d \sin \theta = n \lambda$$

When the specimen has a regular atomic arrangement (crystal), such constructive interference of the radiation appears at predictable angles, and a sharp/ intense diffraction pattern can be obtained. On the other hand, when the specimen has an irregular atomic arrangement (amorphous), constructive interference of the radiation is very weak, and a very broad diffraction pattern is obtained.

In this research, X-ray reflectivity (XRR), out-of-plane $\omega - 2\theta$ scan, and rocking curve (ω −scan, $\omega = \theta \pm \delta$, δ is an offset angle) have been used. Thicknesses of WO_x films were measured by XRR measurement, which is based on reflections and interferences at all interfaces between volumes of different electron densities. Thickness is inversely proportional to the periodicity of fringes; the overall slope is related to the roughness of interface and surface; the critical angle is related to the density. (**Figure 2-3(c)**) In the case of an amorphous film, the glancing angle incidence X-ray diffraction (GIXRD, 2θ scan) is performed with fixed incident angle θ ($0.5 - 1^{\circ}$) to amplify the peak intensity. In the case of an epitaxial film, one-directionally oriented Bragg peaks are seen in out-of-plane $\omega - 2\theta$ scan, and the out-of-plane lattice constant can be obtained from the peak position. (**Figure 2-3(d)**) By measuring the rocking curve, crystal tilting can be obtained. For example, smaller full width half maximum (FWHM) means smaller crystal tilting. (**Figure 2-3(f)**)

2.4 X-ray spectroscopy

X-ray spectroscopy is a typical technique for analyzing the chemical property of a material such as the elemental compositions, relative composition fractions, and electronic structure of the material constituents. X-ray photoelectron spectroscopy (XPS) and X-ray absorption spectroscopy (XAS) are widely used. XPS[4] is a surface-sensitive quantitative technique based on the photoelectric effect, usually trigger by Al Kα (E_{photon} = 1486.6 eV) radiation. (**Figure 2-4(a)**) When X-ray is incident on the surface of the specimen, the core-level electrons or outer electrons of the atoms are excited, and photoelectrons are emitted from the surface if the X-ray photon energy (E_{photon}) exceeds the binding energy of electrons ($E_{binding}$) and work function (ϕ). By measuring the $E_{kinetic}$ of the emitted photoelectron, the $E_{binding}$ of the specimen is obtained through the following equation.

$$E_{binding} = E_{photon} - (E_{kinetic} + \phi)$$

Since the $E_{binding}$ is the intrinsic property of the element, the elemental composition, chemical bonding state, and valence state of material constituents can be determined. The XPS spectrum is named according to the energy level of excited core-electron (**Table 2-1**). In order to analyze the valence state in the specimen, XPS peaks usually need to be deconvoluted. Each deconvoluted peak in XPS corresponds to the electron configuration within the atoms (*i.e.*, 1s, 2s, 2p *etc*). The p, d and f peaks consist of two peaks because of the spin-orbit splitting, and the splitting distance and peak area ratio are nearly the same even in different materials. In the case of p orbitals, the area ratio of $p_{1/2}$ and $p_{3/2}$ peaks is 1: 2, corresponding to 2 electrons in the $p_{1/2}$ level and 4 electrons in the $p_{3/2}$ level. Similarly, the d peaks consist of $d_{3/2}$ and $d_{5/2}$ peaks with an area ratio of 2: 3 while the f peaks consist of $f_{5/2}$ and $f_{7/2}$ peaks with an area ratio of 3: 4.

XAS is used for determining the electronic structure of the specimen, which is usually performed at synchrotron radiation facilities since it requires a highly intense coherent X-ray. When circularly polarized X-ray incident upon the specimen, the core electrons are excited due to X-ray absorption. The energy absorbed correspond to the energy required to promote the core electron into an unoccupied energy level as shown in **Figure 2-4(b)**. [5] The frontal region of XAS, which is called X-ray absorption near edge structure (XANES) spectrum, provides information about the oxidation states of the absorbing atoms and density of state (DOS) of unoccupied/partially filled electronic structure. In the case of TMOs, oxygen K-edge spectrum is commonly observed.[6] The shape of spectra is related to the hybridization of TM and oxygen. Furthermore, there is an X-ray linear dichroism (XLD) spectrum, which can evaluate each orbital occupancy of in-plane and out-of-plane using linearly polarized X-ray. The XLD is calculated as the intensity difference between the spectrum measured by parallelly polarized and perpendicularly polarized beams.

In this research, XPS was used to analyze the valence state of W in the WO_x films at RT. Al Kα radiation was used to generate the photoelectrons, and an Ar flood gun was used to prevent surface charging. The W 4f (30 − 42 eV) and O 1s (528 − 535 eV) core level spectra were corrected with the C 1s calibration peak at 284.8 eV. [17] The W 4f spectra were de-convoluted using the relationship of three spin-orbit doublets of W^{6+} ($5d^0$, 35.8 ± 0.1 eV), W^{5+} ($5d^1$, 34.8 ± 0.1 eV) and W^{4+} ($5d^2$, 33.4 ± 0.1 eV)[7,8] as well as Lorentzian

(30 %) - Gaussian peak with Shirley background subtraction. (*i.e.,* **Figure 2-5**) The x in WO_x was calculated by the following equation.

$$x\ in\ WO_x = \frac{[W^{6+}] \times 3 + [W^{5+}] \times 2.5 + [W^{4+}] \times 2}{[W^{6+}] + [W^{5+}] + [W^{4+}]}$$

where, $[W^{n+}]$ (n = 3.0, 2.5, or 2.0) denotes the percentage of the W ion states and the multiplied value means integers refer to the oxygen contents associate with each W valence state. XAS was measured using two orthogonal linearly-polarized beams at the 2A beamline Pohang accelerator laboratory (PAL). Total electron yield (TEY) was monitored, and the energy resolution is ~0.1 eV.

Table 2-1. Nomenclature as used in XPS and XAS

Core state (XPS)	**Spectroscopic name (XAS)**
1s	K
2s, 2p	L_1, $L_{2,3}$
3s, 3p ($p_{1/2}$ and $p_{3/2}$), 3d ($d_{3/2}$ and $d_{5/2}$)	M_1, $M_{2,3}$, $M_{4,5}$
4s, 4p ($p_{1/2}$ and $p_{3/2}$), 4d ($d_{3/2}$ and $d_{5/2}$), 4f ($f_{5/2}$ and $f_{7/2}$)	N_1, $N_{2,3}$, $N_{4,5}$, $N_{6,7}$

2.5 Thermopower

Thermopower is a powerful physical property associated with the electron transport and electronic structure of the material. When a temperature difference (ΔT) is introduced across a material, the chemical potential becomes inclined due to the chemical potential difference between hot side and cold side. Consequently, the charge carriers will diffuse from the hot side to the cold side, resulting in a thermo-electromotive force (ΔV). ΔV is proportional to ΔT, and the respective proportionality constant is called thermopower (= or Seebeck coefficient).

$$S = \Delta V / \Delta T$$

In the case of semiconductors, including TMOs, the S value is given by the Mott equation.[9]

$$S = -\frac{\pi^2}{3}\frac{k_B^2\,T}{e}\left\{\frac{d\left[\ln\left(\sigma(E)\right)\right]}{dE}\right\}_{E=E_F} = -\frac{\pi^2}{3}\frac{k_B^2\,T}{e}\left\{\frac{1}{n}\cdot\frac{dn(E)}{dE}+\frac{1}{\mu}\cdot\frac{d\mu(E)}{dE}\right\}_{E=E_F}$$

Here, the symbols k_B, e, n, E_F and μ refer to the Boltzmann constant, electron/hole charge, carrier concentration, Fermi energy, and carrier mobility, respectively. Several characteristics can be clarified from thermopower measurement. Depending on the carrier type or location of E_F, the thermopower has a negative or positive value since S can be simplified as the partial derivate of DOS with respect to energy at E_F, $|\partial \mathrm{DOS}(E)/\partial E|_{E=E_F}$. For example, in general, if the E_F is located on the side with a positive slope or has carrier electrons, S value is negative as shown in **Figure 2-6(a)**. When the E_F is located on the side with a negative slope or has carrier holes, S value is positive as shown in **Figure 2-6(b)**. From the relationship between $|S|$ and σ, which is known as the Jonker plot, the shape of conduction band can be estimated as shown in **Figure 2-6(c)**. As S mostly come from the DOS near the E_F with bi strong dependence on the quality of the specimen, thermopower characterization is a great tool for addressing material properties associated with the DOS.

In this research, S was measured at RT by creating a ΔT of ~10 K across the WO_x film using two Peltier devices. The thermo-electromotive force (ΔV) and ΔT were measured simultaneously, and the S-values were obtained from the slope of the ΔV–ΔT plots. [10]

2.6 Electrical conductivity

For the electrical transport characterization of thin films, Van der Pauw and four-point probe methods are commonly utilized. In the case of isotropic materials, Van der Pauw method is used, where each probe is placed at the corners of the film, and current (I_{12} or I_{13}) flows along one edge of the specimen while voltage (V_{34} or V_{24}) is measured along the opposite edge of the specimen. (**Figure 2-7(a)**) The respect resistance ($R_{12,34}$ or $R_{13,24}$) can be calculated as follows:

$$R_{12,34}=V_{34}/I_{12} \quad \text{or} \quad R_{13,24}=V_{13}/I_{24}$$

Base on $R_{12,34}$ and $R_{13,24}$, ρ ($1/\sigma$) and sheet resistance ($R_s= \rho/\mathrm{d}$) can be expressed with the following equation:

$$\rho = \frac{\pi \mathrm{d}}{ln2}\left(\frac{R_{12,34}+R_{13,24}}{2}\right) f\left(\frac{R_{13,24}}{R_{12,34}}\right) = 4.532\mathrm{d}\left(\frac{R_{12,34}+R_{13,24}}{2}\right)$$

where, d is the thickness of the film and f ($R_{13,24}/R_{12,34}$) is a geometric factor, which is 1 for a symmetric configuration. If the specimen exhibits anisotropic electron transport, four-point probe method is commonly used. Four probes are parallelly placed on one edge with the same separation distance as shown in **Figure 2-7(b)**. Two inner probes (2 and 3) are used for voltage measurement while the outer two probes (1 and 4) are used for flowing current. Unlike S, σ depends on the amount of defects, impurities, and quality of the specimen. Therefore, it is important to fabricate highly crystalized film to understand the intrinsic nature of electron transport properties.

In this research, ρ was measured by d.c. four probe methods with van der Pauw electrode configuration and four-point probe configuration from RT to 30 K. In-Ga alloy was used as the contact electrodes.

2.7 Time-domain thermoreflectance

Time-domain thermoreflectance (TDTR) is a technique that utilizes a sub-picosecond laser to measure the κ [11,12] which is based on changes in the thermoreflectance as a function of delay time. (**Figure 2-8**) The specimen surface is generally coated with a ~100 nm-thick metal transducer such as Mo, Al, Cr. When the pump laser thermally excites a localized area of the specimen surface, the temperature of that area will increase. The respective change in the reflectivity in the time domain is detected by a probe laser. In most TDTR experiments, the signals are obtained as the amplitude and phase of thermoreflectance decay. The simulated phase signals are changed by the κ of specimens. Higher κ exhibits a faster decay, and lower κ exhibits a slower decay.[13] In order to simulate the obtained signal, many input parameters are required (laser spot size, κ of transducer and substrate, density, heat capacity). Since all these parameters affect the TDTR signal, all parameters other than the κ are separately determined from other measurements or sources. Then the κ is adjusted until the simulated decay curve matches the measured decay curve.

In this research, ~100-nm-thick Mo was deposited on the WO_x films as a transducer by dc sputtering. The results were simulated using the packaged software developed by the manufacturer, PicoTherm corporation.

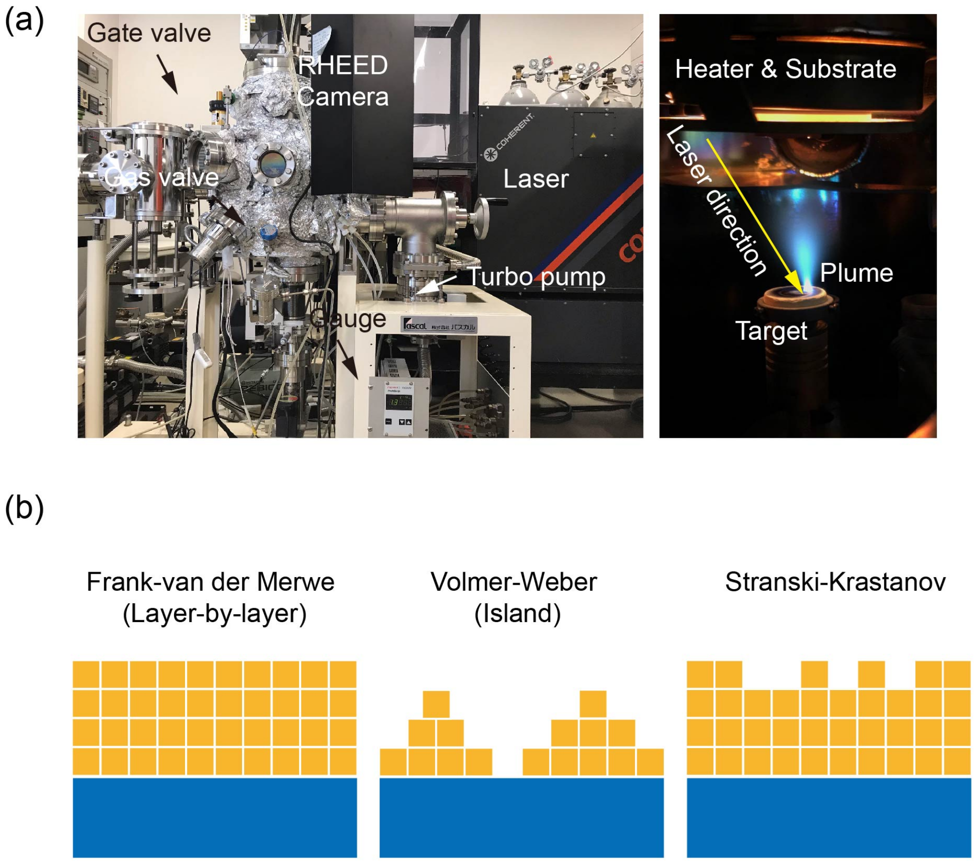

Figure 2-1. (a) PLD system and ablation of target. (b) Various film growth modes.

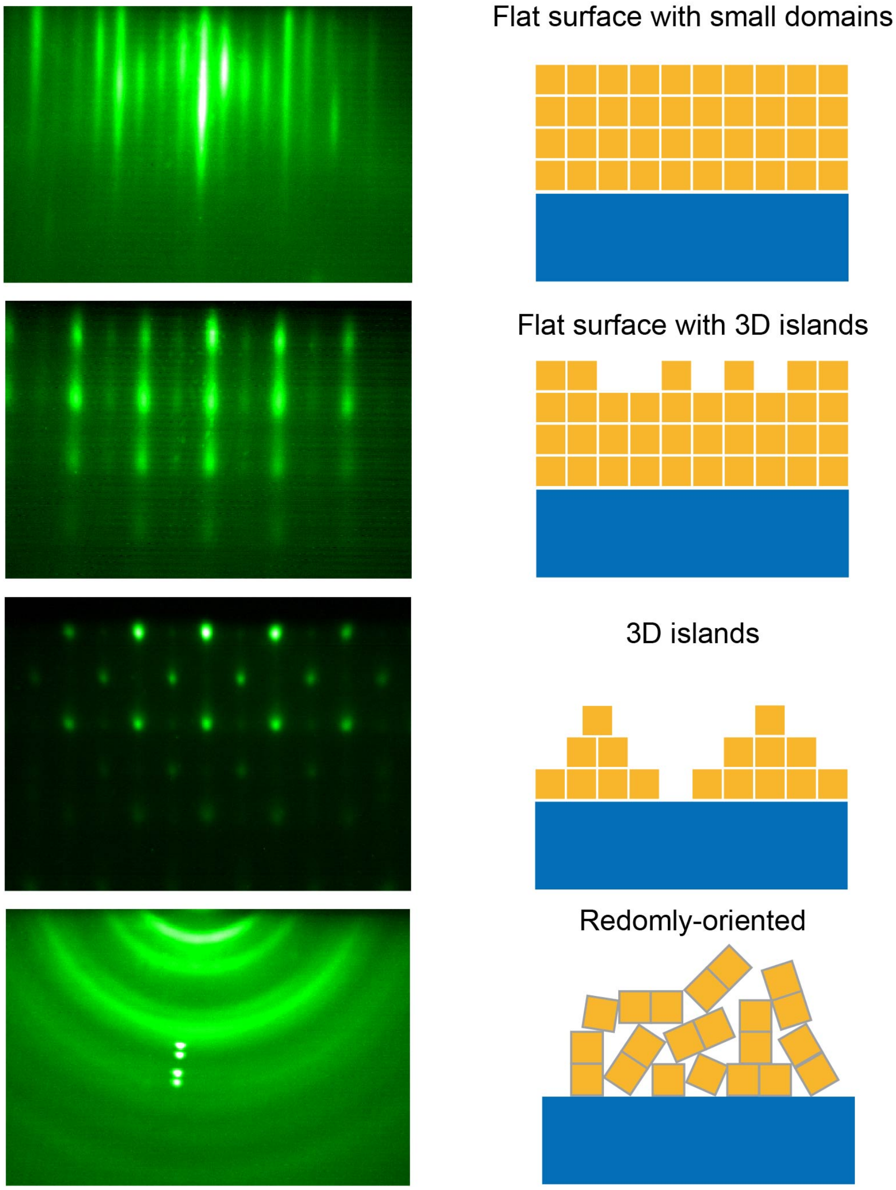

Figure 2-2. RHEED patterns according to different growth modes.

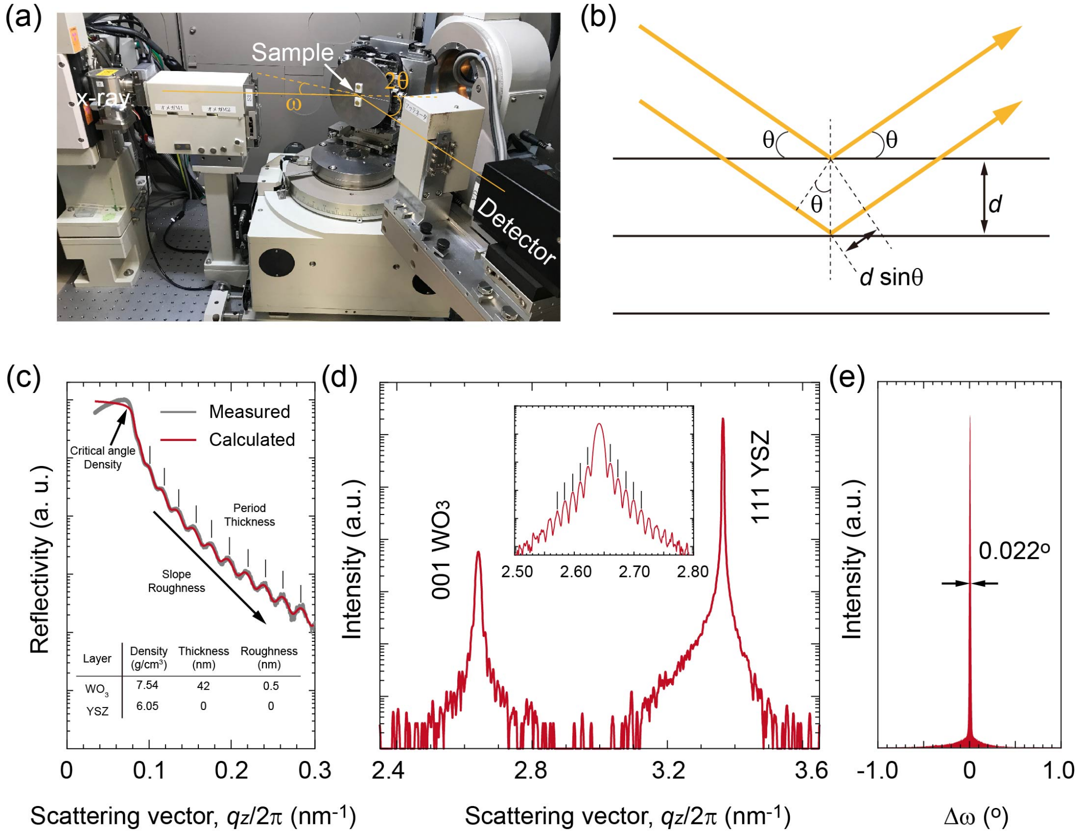

Figure 2-3. (a) XRD system (b) Bragg's law (c) XRR (d) Out-of-plane XRD pattern (e) rocking curve.

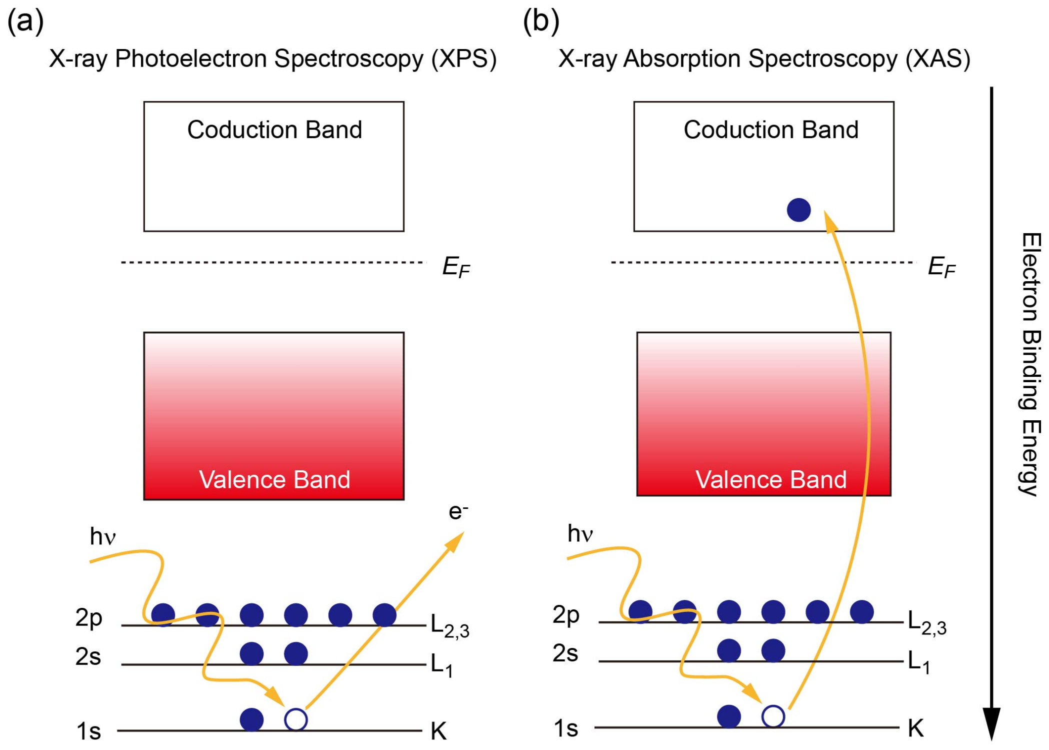

Figure 2-4. Mechanism of core-level spectroscope techniques. (a) XPS. (b) XAS.

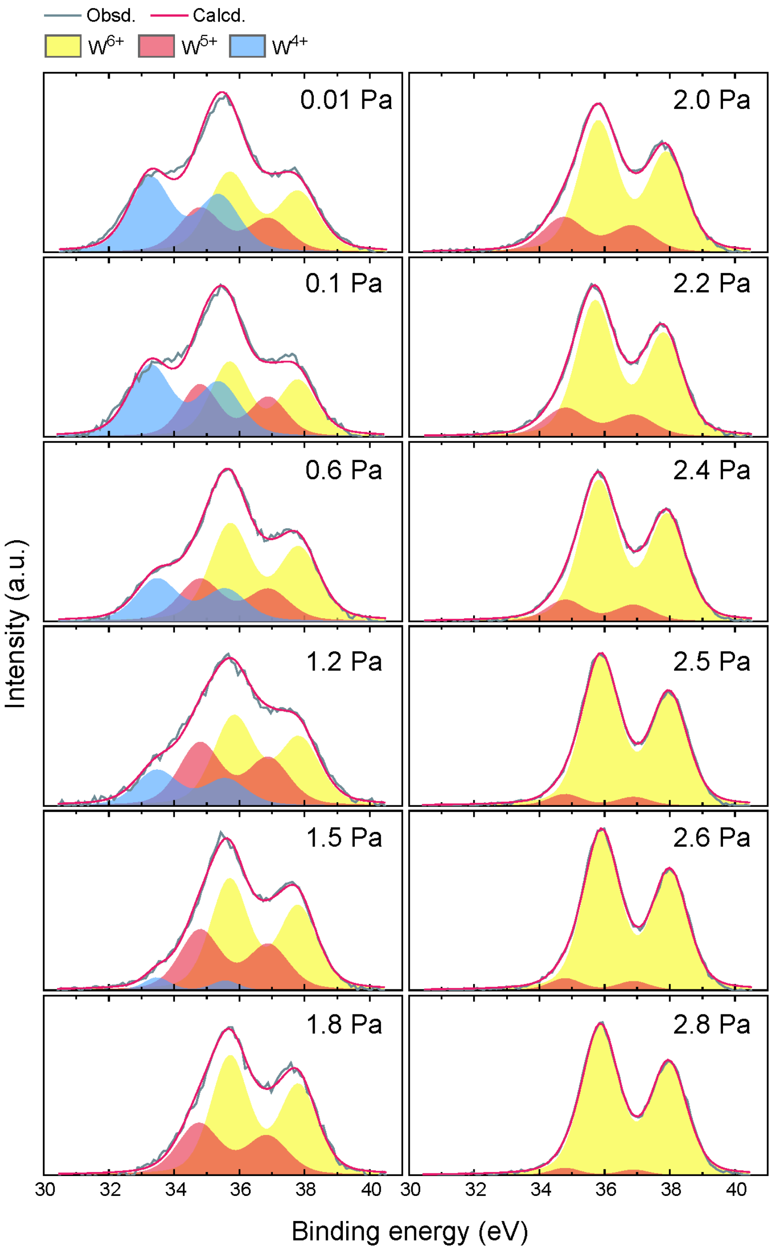

Figure 2-5. XPS spectra of the W 4f peaks of the a-WO$_x$ thin films.[14]

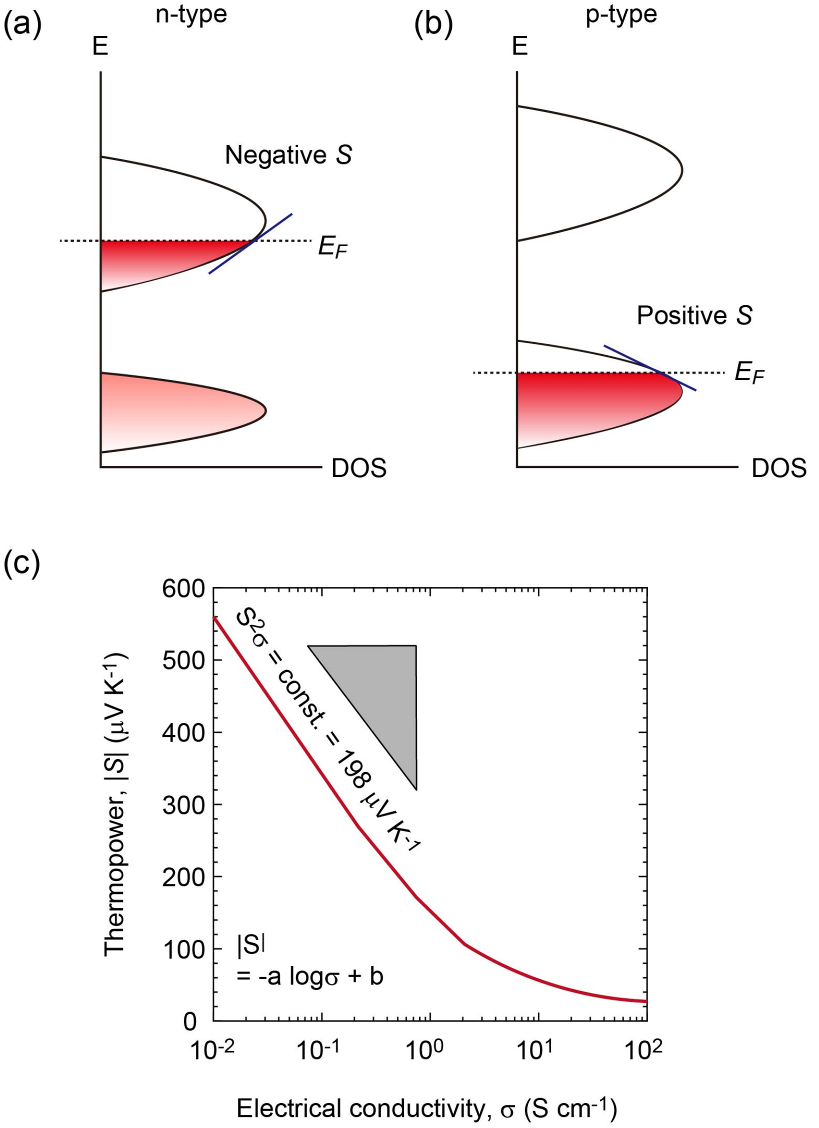

Figure 2-6. Schematic energy band diagram around the Fermi energy for (a) n-type and (b) p-type semiconductors. (c) S-σ (Jonker) plot.

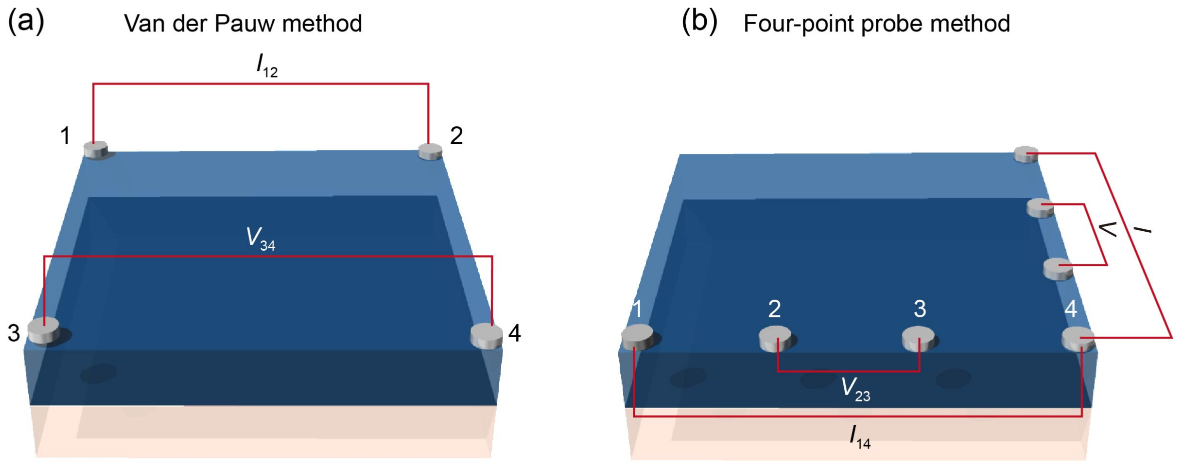
(a) Van der Pauw method

(b) Four-point probe method

Figure 2-7. Schematic diagrams for the measurement of σ. (a) Van der Pauw method. (b) four-point probe method.

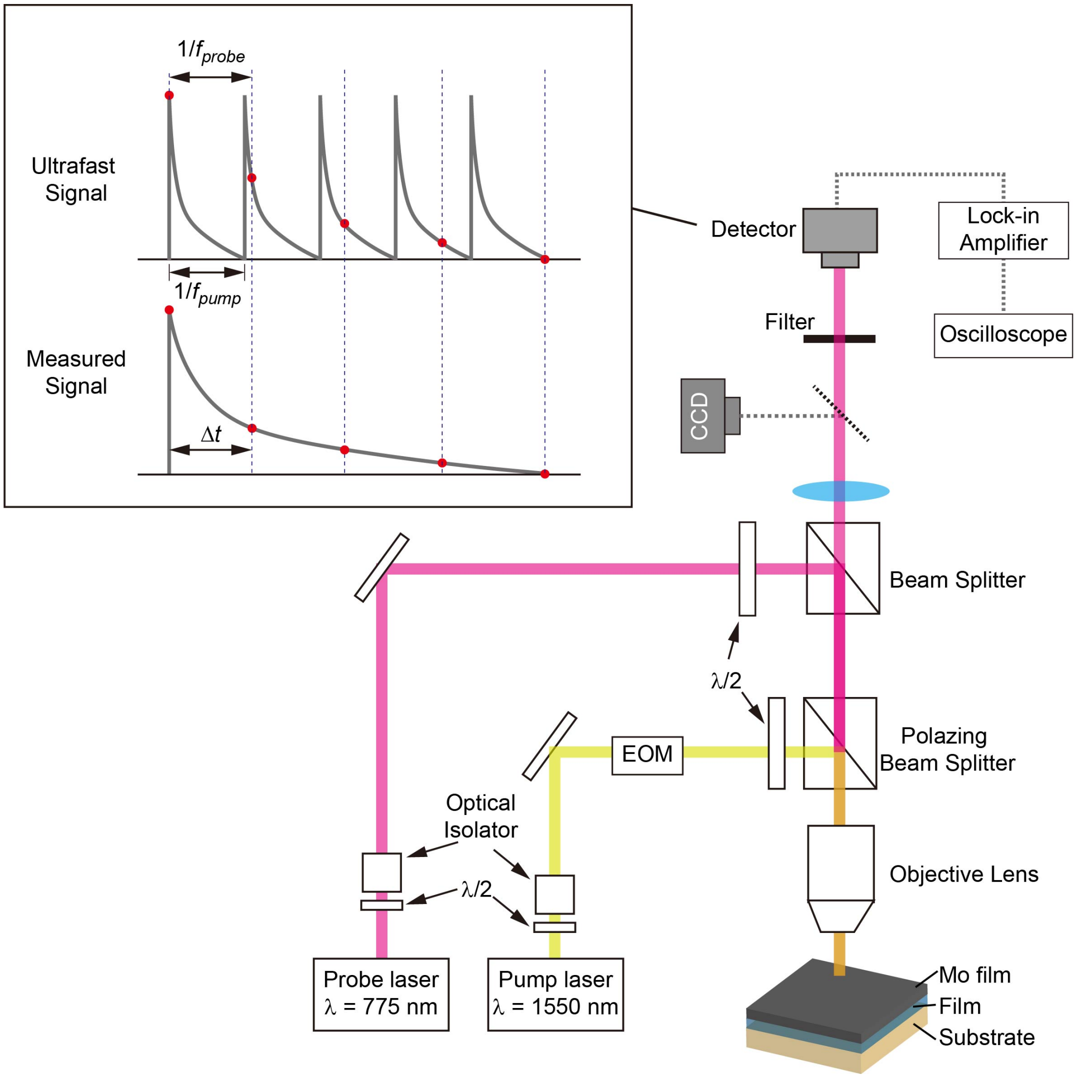

Figure 2-8. Schematic of typical TDTR apparatus.

References

[1] R. Eason, *Pulsed laser deposition of thin films: applications-led growth of functional materials*, (John Wiley & Sons, 2007).

[2] A. Ichimiya, P. I. Cohen, and P. I. Cohen, *Reflection high-energy electron diffraction*, (Cambridge University Press, 2004).

[3] W. H. Bragg and W. L. Bragg, *Proceedings of the Royal Society of London. Series A, Containing Papers of a Mathematical and Physical Character* **88**, 428 (1913).

[4] J. Chastain and R. C. King Jr, *Perkin-Elmer, USA*, 261 (1992).

[5] J. Yano and V. K. Yachandra, *Photosynth. Res.* **102**, 241 (2009).

[6] F. De Groot, M. Grioni, J. C. Fuggle, J. Ghijsen, G. A. Sawatzky, and H. Petersen, *Phys. Rev. B* **40**, 5715 (1989).

[7] C. Guo, S. Yin, Q. Dong, and T. Sato, *RSC Adv.* **2**, 5041 (2012).

[8] S. Lee, Y.-W. Lee, D.-H. Kwak, M.-C. Kim, J.-Y. Lee, D.-M. Kim, and K.-W. Park, *Ceram. Int.* **41**, 4989 (2015).

[9] M. Cutler and N. F. Mott, *Phys. Rev.* **181**, 1336 (1969).

[10] Y. Zhang, B. Feng, H. Hayashi, C.-P. Chang, Y.-M. Sheu, I. Tanaka, Y. Ikuhara, and H. Ohta, *Nat. Commun.* **9**, 2224 (2018).

[11] P. Jiang, X. Qian, and R. Yang, *J. Appl. Phys.* **124**, 161103 (2018).

[12] D. G. Cahill, W. K. Ford, K. E. Goodson, G. D. Mahan, A. Majumdar, H. J. Maris, R. Merlin, and S. R. Phillpot, *J. Appl. Phys.* **93**, 793 (2003).

[13] H. J. Cho, G. Kim, T. Onozato, H. Jeen, and H. Ohta, *Int. J. Heat Mass Transfer* **137**, 263 (2019).

[14] G. Kim, H. J. Cho, Y.-M. Sheu, and H. Ohta, *J. Phys. Chem. C* **123**, 15419 (2019).

Chapter 3. Low thermal conductivity of amorphous tungsten oxide films

3.1 Objective

WO_x is utilized as the active material for several functional applications, including electrochromic displays (ECDs) [1,2], smart windows [3], anode of Li-ion batteries [4], photocatalyst [5], gas sensors [6], and organic solar cells [7]. Such versatility is attributed to the valence states of W, which can be modulated from 4+ to 6+. For example, by electrochemically introducing protons or alkali ions (Li^+, Na^+, and K^+) [2] to WO_3, free carriers are introduced to the conduction band to reduce the W^{6+} ions, forming W^{5+} ($5d^1$) or W^{4+} ($5d^2$). This newly created electronic structure absorbs red light, and the color of WO_3 changes from transparent to dark blue. Therefore, understanding the relationship between the valence state of W and the functional properties of WO_x is significantly important.

WO_x can exhibits many crystalline phases (x = 2, 2.72, 2.82, 2.9, 3), and x can be changed in a step-by-step manner. [8,9] However, isolating the role of W ion valence state from the effect of structural phase transition is difficult. In this regard, investigating oxygen deficient amorphous (a-) WO_x, which does not have well-defined phase boundaries like crystalline WO_x, can be of great value. Unfortunately, although several previous studies have shown the feasibility of the valence state modulation in a-WO_x [10,11], the detailed influence of x on the electrical, optical, and thermal properties still remain unclear due to the lack of systematic studies.

This chapter addresses the systematic relationship between x, and several functional properties of a-WO$_x$ films. The x in a-WO$_x$ was varied from 2.511 to 2.982, and the charges in the functional properties in accordance to the valence state of W are analyzed in detail. The results from this chapter will be of great use for improving and optimizing WO$_x$ based devices [12-14] and provide a solid guideline for the range of x that needs to be considered even for the utilization of crystalline WO$_x$ in device applications.

3.2 Film synthesis and characterizations

The a-WO$_x$ films were deposited by PLD on alkaline-free glass substrates (10 × 10 × 0.7 mm, EAGLE XG®, Corning®) at RT. The laser fluence, pulse frequency, and the deposition time were ~1 J cm^{-2} pulse^{-1}, 10 Hz, and 10 mins, respectively. The partial oxygen pressure (P_{O2}) during the film growth was varied from 10^{-2} to 2.8 Pa, resulting in the deposition rates of 8 − 17 pm pulse^{-1}. The resultant film thicknesses were 49 − 105 nm. Optical transmission and reflection spectra of the resultant films were measured using an ultraviolet-visible-NIR spectrometer (UV-Vis-NIR, SolidSpec-3700, Shimadzu Co.) at RT. The σ of the resultant WO$_x$ films was measured by Van der Pauw method temperature range from 30 to 300 K. The S was measured by a steady- state method at RT. The structural properties (GIXRD), optical spectra (UV-Vis-NIR), electrical transport properties, and thermal conductivity (TDTR) of the films were also characterized as a function x. The TDTR simulation parameters are summarized in **Table 3-1**. For accuracy, Mo transducer on the glass substrate was measured separately.

Table 3-1. TDTR simulation parameters for analyzing a-WO$_x$ films on EAGLE

Material	Parameter	Value
Mo	Density	10200 Kg m^{-3}
	C_p	250 J Kg^{-1} K^{-1} [15]
	κ	31 W m^{-1} K^{-1}
a-WO$_x$	Density	5880 – 9350 Kg m^{-3}
	C_p	304 – 319 J Kg^{-1} K^{-1} [16]
EAGLE	Density	2350 Kg m^{-3}
	C_p	768 J Kg^{-1} K^{-1} [17]
	κ	1 W m^{-1} K^{-1}

3.3 Results and discussion

From GIXRD measurements, only halo pattern from the film ($q/2\pi$ ~2.8−4 nm^{-1}) with that from the substrate ($q/2\pi$ ~2.6 nm^{-1}) was detected (**Figure 3-1(a)**), confirming the amorphous phases for all films. The bulk density of the a-WO$_x$ films gradually increased from ~5.8 g cm^{-3} to ~9.3 g cm^{-3} with reducing P_{O2} (**Figure 3-1(b)**). Since the density of crystalline WO$_x$ increases from 7.1 g cm^{-3} to 10.8 g cm^{-3} if x changes from 3 to 2, the observed increase in the density suggests a reduction in x from the decrease in P_{O2}. The a-WO$_x$ films deposited under high P_{O2} (> 2 Pa) showed a lower density than c-WO$_3$ (7.1 g cm^{-3}). In addition, the surface roughness of these films was greater than that of the a-WO$_3$ films deposited under lower P_{O2} (< 2 Pa) (**Figure 3-1(c)**), most likely due to a formation of the porous structures at higher P_{O2}. [18]

The XPS spectra of the a-WO$_x$ films are shown in **Figure 3-2**. The W 4f doublet peaks (W 4f$_{7/2}$: ~36 eV, W 4f$_{5/2}$: ~38 eV) were clearly observed for films grown under P_{O2} = 2.8 Pa, which became broader with decreasing P_{O2}. An additional peak appeared around 33 eV at P_{O2} = 0.01 Pa (**Figure 3-2(a)**). On the other hand, tuning P_{O2} results in an insignificant change in the O 1s spectra, which are composed of O^{2-} peak ~530.8 eV and OH^- related peak at 532.1 eV (**Figure 3-2(b)**). The OH^- peak is likely from ambient contaminations, which cannot be controlled and therefore, can explain the lack of meaningful tendency in O 1s spectra.

The ratio of W^{6+} ($5d^0$) in the total W ion has an inverse proportionality to P_{O2}, changing from 100 % to ~60 % upon reducing the P_{O2} from 2.8 Pa to 1.5 Pa while that of W^{5+} ($5d^1$) in the total W ion increased almost linearly from 0 % to ~35 % (**Figure 3-2(c)**). Further reducing of P_{O2} (P_{O2} < 1.5 Pa) leads to the increment in W^{4+} ($5d^2$), thus gradually declining the W^{5+}. It should be noted that the concentration of W^{5+} was maximized for P_{O2} ~1.2−1.5 Pa. From this analysis, the O/W ratio in a-WO$_x$ films was varied from 2.982 (P_{O2} = 2.8 Pa) to 2.511 (P_{O2} = 0.01 Pa), and the linear relationship between P_{O2} and x was confirmed (**Figure 3-2(d)**). These results show that a-WO$_x$ films were successfully fabricated with various x.

With the decline of x, the color of the a-WO$_x$ films changed from colorless transparent to metallic black. Meanwhile, the optical transmission decreased drastically, due to the formation of oxygen deficiency. [11,19,20] The absorption coefficient (α) was extracted using the observed transmission (*Trans.*) and reflection (R) from the relationship of $\alpha = d^{-1} \cdot \ln [(1-R) \cdot Trans.^{-1}]$. [21] **Figure 3-3(a)** displays the absorption coefficient versus x. At the high O/W ratio ($x > 2.935$), the absorption coefficient, α, steeply increased above 3 eV due to the direct transition from O 2p to W 5d (Tauc gap). The Tauc gap of a-WO_x films ($x > 2.888$) was ~3.25 eV, agreeing well with that of the reported values (3.2 – 3.5 eV). [22-24] The Drude-like absorption due to the free carrier electrons (~1.4 eV) increased from ~0 to 10^5 cm^{-1} when x decreased from 2.928 to 2.779. The shoulder absorption peak around 3.0 eV is most likely due to the oxygen vacancies. [20] The Drude-like absorption displays an inverse proportionality to x from 1522 cm^{-1} ($x = 2.982$) to 93278 cm^{-1} ($x = 2.779$) and was not observable below $x = 2.642$ (**Figure 3-3(b)**). The disappearance of Drude-like absorption for $x = 2.642$ is probably due to the formation of W^{4+} ($5d^2$) valence state. [20] The spectra continuously changed with decreasing x, and finally, the Tauc gap was closed at $x = 2.511$. It should be noted that the Burstein-Moss shift was not observed, which suggests a small dispersion in the conduction band. These results suggest that the free carriers are predominantly due to the formation of W^{5+} ($5d^1$).

Next, the electron transport properties of a-WO_x films were investigated. **Figure 3-4(a)** shows the ρ of various a-WO_x films at RT. With decreasing x from 2.982 to 2.642, ρ drastically reduced from 2×10^4 Ω cm to 3×10^{-3} Ω cm. The white [9] and grey square [25] are polycrystalline WO_x, and the black square is epitaxial WO_x [26]. Crystalline WO_xs (c-WO_x) also show similar behaviors with the amorphous ones, but there exists a two-orders-of-magnitude difference, likely due to the μ difference. **Figure 3-4(b)** shows the $\rho-T$

curves for the a-WO_x films from 300 K to 30 K. The ρ for the entire a-WO_x films increased with decreasing temperature, indicating that conduction electrons are thermally activated. The slope of the ρ–T curve decreased continuously and was minimized at $x = 2.642$, below which the slope increased again. Similarly, $-S$ decreased with decreasing x until it reached $x = 2.642$ (**Figure 3-4(c)**). Since the $-S$ of an n-type semiconductor can be expressed as $-S = -(k_B / e)$ [ln (DOS/n) + A], where A is transport constant (typically $0 \leq A \leq 2$), respectively [27], the decreasing tendency of $-S$ indicates that the E_F increased with decreasing x. Thus, the carrier concentration increased with decreasing x until it reached $x = 2.642$. However, when the x was further reduced ($x < 2.642$), the ρ and $-S$ slightly increased with decreasing the x. The $-S - \sigma$ relation of the a-WO_x films at $x \leq 2.642$ is located at slightly higher $-S$ side than that at $x \geq 2.779$. Similar behavior of $-S$ was reported in the WO_x-ECT upon protonation [14], and the $-S$ did not return to the original value after oxidation. The activation energy of σ (E_a) of the a-WO_x films around RT was extracted by assuming Arrhenius-type thermal activation of the σ (**Figure 3-4(d)**). The E_a decreased from 94 meV to 6.9 meV with decreasing x until it reached 2.642, suggesting that the E_F gradually approached the mobility edge with increasing W^{5+} concentration. When x was less than 2.642, the E_a increased to 29 meV with decreasing the x.

Finally, the relationship between x and the κ of the a-WO_x films at RT was investigated, which is summarized in **Figure 3-5**. The reported κ of c-WO_x (white square) was also plotted for comparison. Although the observed κ (κ_{obsd}) of c-WO_x is linearly proportional with decreasing x (i.e., 1.3 W m^{-1} K^{-1} ($x = 2.98$) to 12 W m^{-1} K^{-1} ($x = 2.72$) [9]), a-WO_x

films did not show such tendency. The κ_{obsd} of a-WO$_x$ ranges from ~0.9 W m^{-1} K^{-1} (x = 2.982) to ~1.6 W m^{-1} K^{-1} (x = 2.642), which is far lower than that of the c-WO$_x$ (**Figure 3-5 (a)**). Note that the porous structures of the a-WO$_x$ films (x >2.93) deposited at higher P_{O2} (>2.5 Pa) show slightly lower κ_{obsd}. The κ_{obsd} is the sum of the κ_{phonon} and $\kappa_{\mathrm{electron}}$, but since there is no lattice in a-WO$_x$ films, the κ_{phonon} was defined as κ_{int} (intrinsic κ), which was calculated from Wiedemann-Franz law. (**Figures 3-5(c)** and **3-5(d)**). The contribution of $\kappa_{\mathrm{electron}}$ in a-WO$_x$ is low compared to that in c-WO$_x$ due to the low μ. Both κ_{obsd} and $\kappa_{\mathrm{electron}}$ (grey dashed line) of c-WO$_x$ have linear dependency on σ, indicating the enhancement in $\kappa_{\mathrm{electron}}$ upon reducing x (**Figure 3-5(c)**). On the other hand, despite some scattering at low values of σ, the κ_{obsd} of a-WO$_x$ shows an increasing behavior with increasing σ (**Figure 3-5(d)**). The $\kappa_{\mathrm{electron}}$ (red dashed line) showed a maximum at around x = 2.642 (~ 0.25 W m^{-1} K^{-1}), demonstrating that free carrier electrons of W^{5+} solely contribute $\kappa_{\mathrm{electron}}$. From the extracted $\kappa_{\mathrm{electron}}$ (**Figure 3-5(b)**), it can be seen that κ_{int} of a-WO$_x$ films is ranging from ~0.85 W m^{-1} K^{-1} to ~1.2 W m^{-1} K^{-1}, which is 1/4 – 1/3 compared to that of c-WO$_x$ (κ_{int} = 3 – 4.5 W m^{-1} K^{-1} except x > 2.98). The κ_{obsd} of x = 2.982 is close to the minimum κ_{min} of WO$_x$ ~0.4 W m^{-1} K^{-1}, which was calculated using the Cahill model. [28] These results show that both μ and κ_{obsd} of a-WO$_x$ are far smaller than those of c-WO$_x$ due to the lack of a periodic lattice structure in a-WO$_x$.

The enhancement of –S, ρ, and E_{a} was observed when x was less than 2.642. Around x = 2.642, W^{5+} is dominant and maximized in the film. The detailed chemical reaction in a-WO$_x$ is as follows. For a-WO$_x$ films with high values of x, W^{5+} valence state increases with decreasing oxygen contents; simultaneously, E_F gradually increases, and the W^{5+} valence state generates free electrons for heat and electron transport. As x decreases further down to x ~2.6, the W^{4+} valence state forms to reduce the concentration of W^{5+} valence state. Likely, the localization of the d^2 electrons in W^{4+} valence state cannot enhance the electrical properties. Therefore, $-S$ and ρ start to increases although x decreases further. This can be supported from the disappearance of Drude-like behavior in the absorption spectra. Consequently, it demonstrates that free electrons from W^{5+} solely contribute to heat transport and the versatile functional properties of a-WO_x are attributed to the transition between W^{5+} and W^{6+}.

3.4 Conclusion

In this chapter, systematic investigations of the electrical, optical, and thermal properties of a-WO_x were shown with the respective valence states of W ions (+6 (d^0), +5 (d^1), and +4 (d^2)). Although the +6 dominant films were electrically insulating with transparency in the visible region, both optical transmissivity and ρ decreased drastically with increasing the concentration of +5 states. Heat can be carried by additional free conduction electrons, which increase the κ. However, the +4 dominant films showed slightly higher ρ while maintaining the optical opacity. These results suggest that the redox of tungsten between +6 and +5 creates switchable properties of WO_x, and device application needs to be performed based on the transition between +6 and +5, which corresponds to the range of $2.64 < x < 3$.

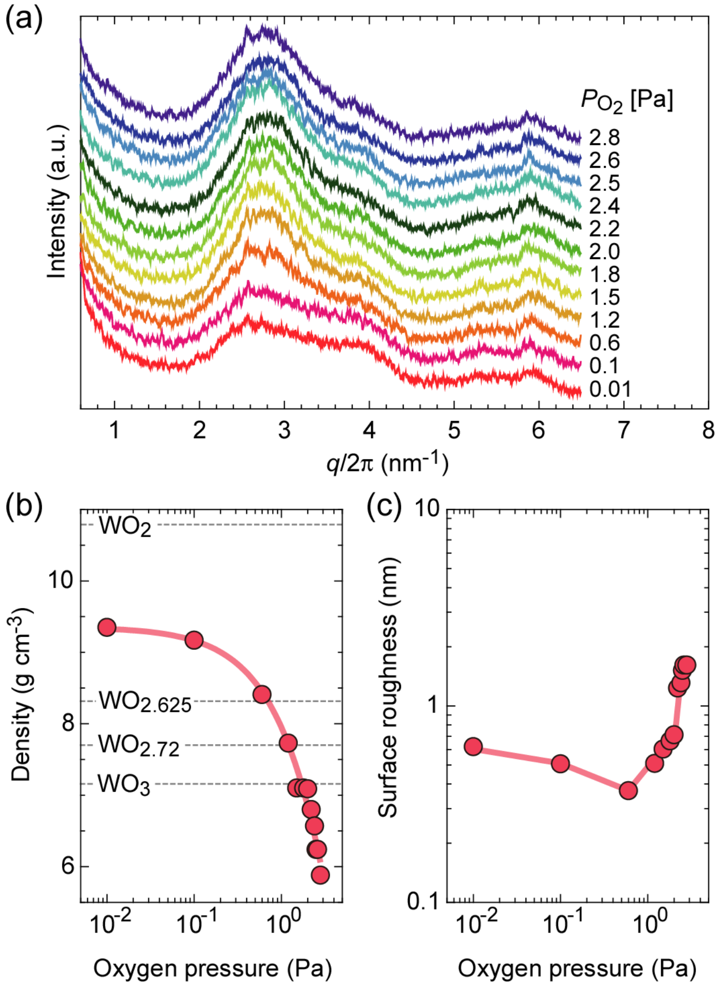

Figure 3-1. Structural features of the resultant WO$_x$ thin films under various oxygen pressures. (a) GIXRD of a-WO$_x$ films at RT. The incident angle of the X-ray was fixed at 0.5°. (b) Bulk densities of the resultant a-WO$_x$ films, which were measured by the XRR patterns (c) The surface roughness (≡root mean square roughness) of the resultant a-WO$_x$ films, which was also evaluated by the XRR measurements. The surface roughness remarkably increases from ~0.4 nm to ~1.7 nm when the oxygen pressure exceeds 1 Pa.

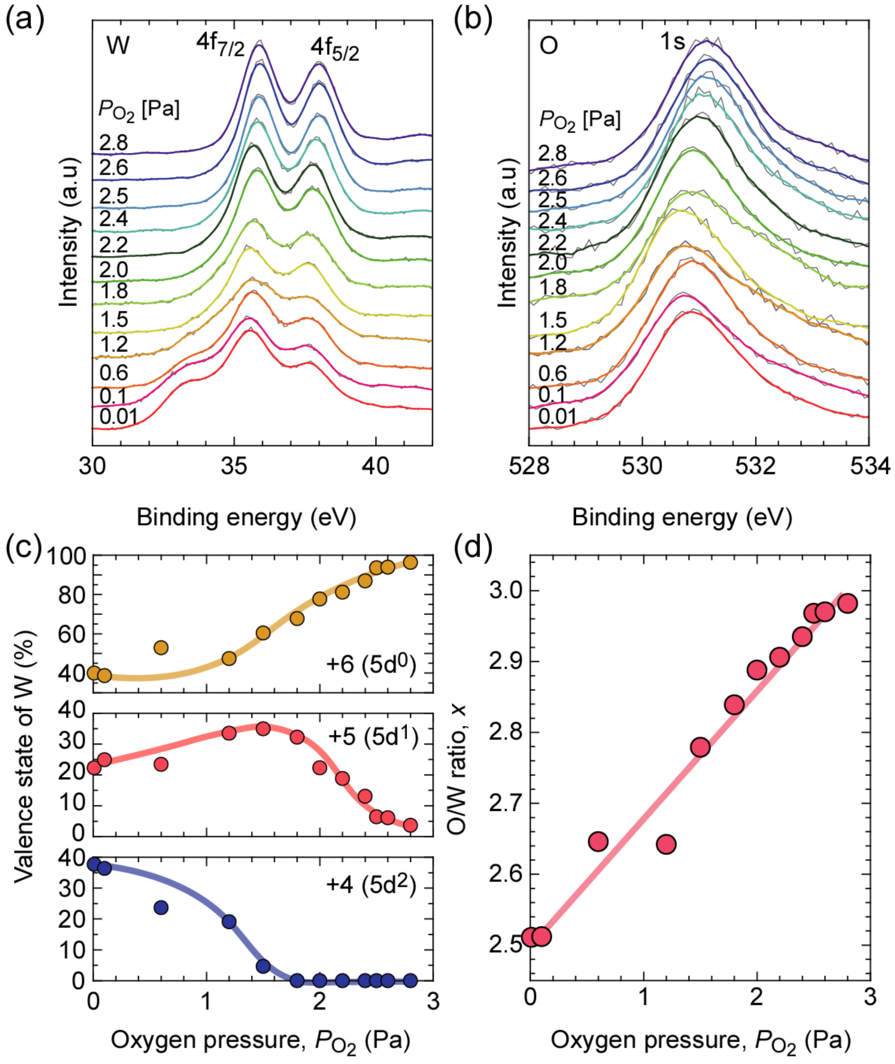

Figure 3-2. XPS spectra of the a-WO$_x$ thin film surfaces. (a) W 4f and (b) O 1s spectra for various films grown with different oxygen pressures. (c) De-convoluted valence state from +6 to +4 plotted as a function of oxygen pressure. (d) The relationship between O/W ratio, *x,* and oxygen pressure.

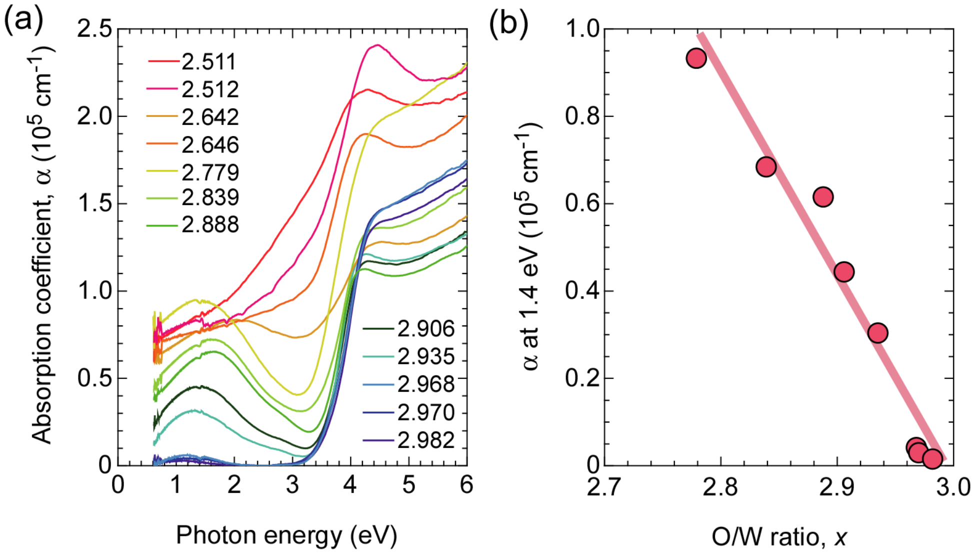

Figure 3-3. Optical characteristics of the resultant a-WO$_x$ thin films with various O/W ratios. (a) The α versus photon energy for various values of x. (b) The α of various values of x at 1.4 eV.

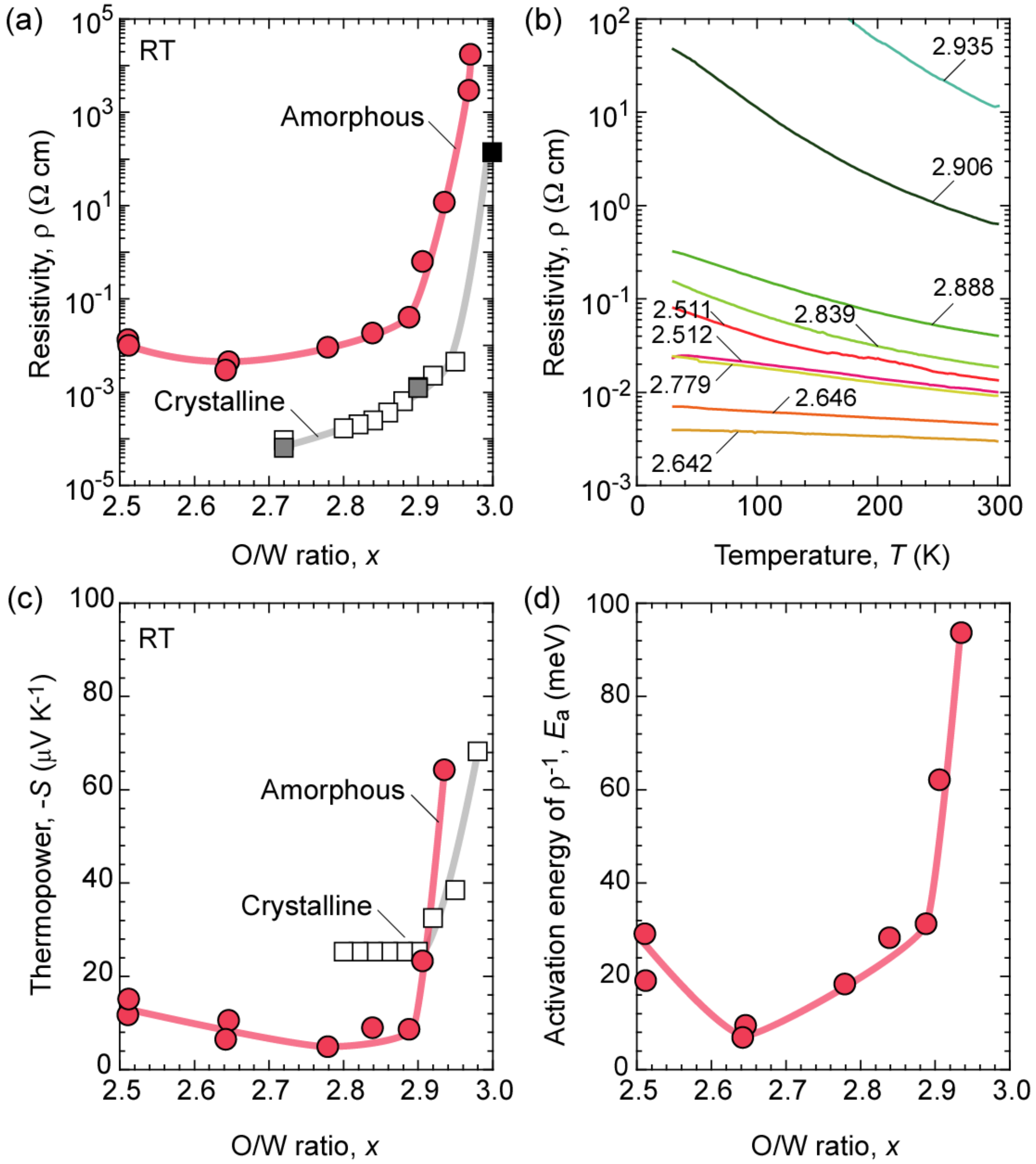

Figure 3-4. Electron transport properties of the a-WO$_x$ films. (a) The ρ of crystalline WO$_x$ ceramics and amorphous WO$_x$ films as function of x. (b) Temperature dependent ρ of the a-WO$_x$ films. (c) The relationship between the -S and O/W ratio. (d) E_a, which was calculated using Arrhenius plot.

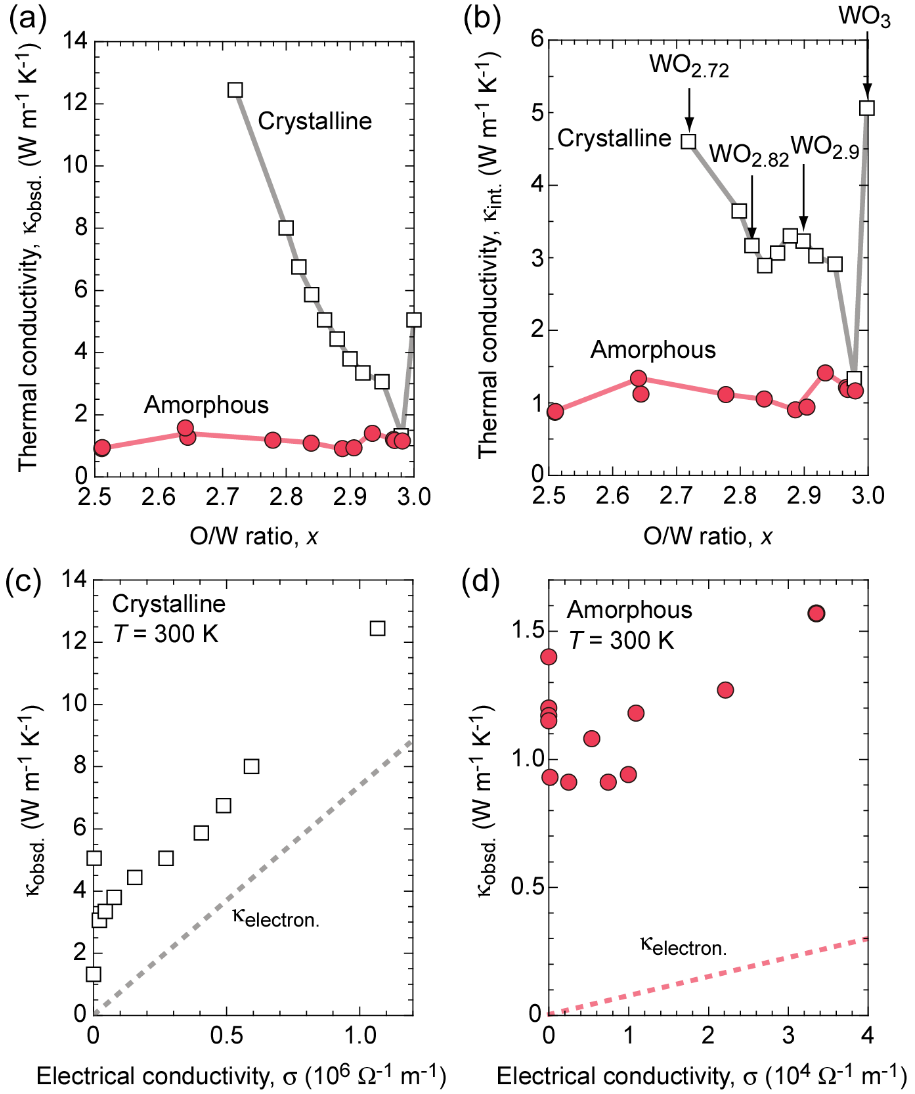

Figure 3-5. Heat transport features of the a-WO$_x$ thin films in the cross-plane direction at RT. (a) The κ_{obsd} of amorphous (red circle) films compared with that of crystalline (white square [9]) WO$_x$ films for various x. (b) κ_{int} with various x. (c) The κ_{obsd} plotted as a function of σ for c-WO$_x$. (d) κ_{obsd} plotted as a function of σ for a-WO$_x$.

References

[1] C. G. Granqvist, *Sol. Energy Mater. Sol. Cells* **60**, 201 (2000).

[2] C. G. Granqvist, *Thin Solid Films* **564**, 1 (2014).

[3] P. Yang, P. Sun, and W. Mai, *Mater. Today* **19**, 394 (2016).

[4] Y. Sun, W. Wang, J. Qin, D. Zhao, B. Mao, Y. Xiao, and M. Cao, *Electrochim. Acta* **187**, 329 (2016).

[5] X. Guo, X. Qin, Z. Xue, C. Zhang, X. Sun, J. Hou, and T. Wang, *RSC Adv.* **6**, 48537 (2016).

[6] C. S. Rout, A. Govindaraj, and C. Rao, *J. Mater. Chem.* **16**, 3936 (2006).

[7] L. You, B. Liu, T. Liu, B. Fan, Y. Cai, L. Guo, Y. Sun, and interfaces, *ACS Appl. Mater.* **9**, 12629 (2017).

[8] G. Mattoni, A. Filippetti, N. Manca, P. Zubko, and A. D. Caviglia, *Phys. Rev. Mater.* **2**, 053402 (2018).

[9] F. Kaiser, P. Simon, U. Burkhardt, B. Kieback, Y. Grin, and I. Veremchuk, *Crystals* **7**, 271 (2017).

[10] B. W. Faughnan, R. S. Crandall, and P. M. Heyman, *RCA Rev.* **36**, 177 (1975).

[11] S.-H. Lee, H. M. Cheong, C. E. Tracy, A. Mascarenhas, A. Czanderna, and S. K. Deb, *Appl. Phys. Lett.* **75**, 1541 (1999).

[12] P. Grey, L. Pereira, S. Pereira, P. Barquinha, I. Cunha, R. Martins, and E. Fortunato, *Adv. Electron. Mater.* **2**, 1500414 (2016).

[13] P. Barquinha, S. Pereira, L. Pereira, P. Wojcik, P. Grey, R. Martins, and E. Fortunato, *Adv. Electron. Mater.* **1**, 1500030 (2015).

[14] T. Katase, T. Onozato, M. Hirono, T. Mizuno, and H. Ohta, *Sci. Rep.* **6**, 25819 (2016).

[15] L. Khriplovich and I. Paukov, *J. Chem. Thermodyn* **15**, 333 (1983).

[16] F. Sale, *Thermochim. Acta* **30**, 163 (1979).

[17] C. Incorporated, *EAGLE XG® Slim Glass Product Information Sheet*, https://www.corning.com/media/worldwide/cdt/documents/Eagle_PI_Sheet_2019.pdf.

[18] H. Ohta, Y. Sato, T. Kato, S. Kim, K. Nomura, Y. Ikuhara, and H. Hosono, *Nat. Commun.* **1**, 118 (2010).

[19] G. Leftheriotis, S. Papaefthimiou, P. Yianoulis, and A. Siokou, *Thin Solid Films* **384**, 298 (2001).

[20] G. A. Niklasson and C. G. Granqvist, *J. Mater. Chem.* **17**, 127 (2007).

[21] W. Q. Hong, *J. Phys. D: Appl. Phys.* **22**, 1384 (1989).

[22] L. Berggren, J. C. Jonsson, and G. A. Niklasson, *J. Appl. Phys.* **102**, 083538 (2007).

[23] S. Deb, *Philos. Mag.* **27**, 801 (1973).

[24] K. S. Rao, B. R. Kanth, G. S. Devi, and P. Mukhopadhyay, *J. Mater. Sci. Mater. Electron.* **22**, 1466 (2011).

[25] G. Kieslich, I. Veremchuk, I. Antonyshyn, W. G. Zeier, C. S. Birkel, K. Weldert, C. P. Heinrich, E. Visnow, M. Panthöfer, and U. Burkhardt, *Phys. Chem. Chem. Phys.* **15**, 15399 (2013).

[26] K. Yoshimatsu, T. Soma, and A. Ohtomo, *Appl. Phys. Express* **9**, 075802 (2016).

[27] M. Ohtaki, T. Tsubota, K. Eguchi, and H. Arai, *J. Appl. Phys.* **79**, 1816 (1996).

[28] D. G. Cahill, S. K. Watson, and R. O. Pohl, *Phys. Rev. B* **46**, 6131 (1992).

Chapter 4. Coexistence of low thermal conductivity and high electrical conductivity in tungsten oxide films with 1D atomic defect tunnels

4.1 Objective

Electron conduction and heat conduction in media are associated with σ and κ, respectively. As both σ and κ are increased/suppressed simultaneously by reducing/introducing impurities, atomic vacancies, and boundaries, it is considerably difficult to solely engineer the σ and κ in different directions. In the case of amorphous materials as seem from chapter 3, it is easy to control the σ but difficult to control the κ due to low value of vibrational density of states. Therefore, crystallized materials with well-defined lattice are appropriate for controlling both σ and κ, seperately. Nevertheless, materials showing unusual transport characteristics such as the coexistence of high electron conduction and low heat conduction, which are required to realize efficient thermal management systems, are rare.

Nanostructuring approaches such as introducing point defects [1-4] and layers [5-7] are known as effective ways to reduce κ. In general, the phonon mean free path is much longer than the carrier electron mean free path. Therefore, when the average distance between two adjacent defects is shorter than the phonon mean free path and longer than the carrier electron mean free path, phonon propagation would be suppressed, but electron propagation would mostly be maintained. [8] However, it is still challenging to reduce heat conduction while keeping high electron conduction (mobility), using nano-structuring, which can be understood using the schematic diagram in **Figure 4-1**. When a 0D defect or dot is introduced (**Figure 4-1(a)**), both electron and phonon can be transported without suppression when the 0D defect density is low because of the low phonon scattering cross section. On the other hand, both electrons and phonons are scattered when the 0D defect density is sufficiently high [9]. If a 2D layered structure is fabricated (**Figure 4-1(c)**), electrons and phonons are both scattered at the heterointerfaces. Therefore, they cannot quickly be transported through the interface.

In order to overcome these difficulties, an excellent solution is proposed in **Figure 4-1(b)**: introducing 1D atomic defect tunnel [10,11] or wire to reduce the phonon propagation without reducing the electron propagation. In this structure, the probability of phonon scattering (short-to-mid wavelength [8]) by the 1D atomic defect tunnel or wire is much higher than that in structures with 0D defect or dot even if the 1D defect density is low. Further, if the average distance between two neighboring 1D defects can be controlled to be much longer than the carrier electron mean free path, the electron propagation can be expected to be preserved when the 1D defect density is low.

To verify this hypothesis experimentally, oxygen-deficient tungsten oxide (WO_x, $2.7 \leq x \leq 3$) epitaxial films are selected as the candidate. The bulk crystal structure of oxygen-deficient WO_x contains 1D tunnel structure [12,13] and can be epitaxially grown on perovskite oxide single crystals coherently. [14-18] Therefore, WO_x with 1D tunnel structure can be stabilized on a substrate. In fact, Ning *et al*. reported that the κ of WO_x films grown on (001) $LaAlO_3$ substrate under different oxygen atmospheres decreased dramatically with decreasing the x whereas the σ increased in an opposing way. [18] Based on the results from the WO_x films grown on various substrates, they concluded that the κ decreased with increasing the volumetric strain without discussing the atomic arrangement of the WO_x films although the κ of a crystal is extremely sensitive to the disordering of the atomic arrangement, which also need to be thoroughly examined.

This chapter addresses that 1D atomic defect tunnels in crystallized WO_x films exhibiting low κ and high σ. The WO_x epitaxial films were fabricated on $LaAlO_3$ substrates under a precisely controlled oxygen atmosphere. Crystallographic analyses revealed that 1D atomic defect tunnels are formed randomly along the rectangular-shaped grains in the in-plane direction. Coexistence of high electron conduction and low heat conduction was realized in these structures at $x < 2.9$.

4.2 Film synthesis and characterizations

The WO_x films were heteroepitaxially grown on (001) $LaAlO_3$ single crystal substrate by PLD at 700 °C in oxygen atmospheres. The laser fluence, pulse frequency, and the deposition time were ~1 J cm^{-2} pulse^{-1}, 10 Hz, and 5 minutes. The oxygen pressure was varied from 2 to 13 Pa during the deposition to modulate the x in WO_x. The thickness of the films was ~40 nm in all cases. The growth condition of all the WO_x films was determined by optimizing the growth condition of the WO_x film (13 Pa) from the viewpoints of

RHEED pattern, surface morphology, and average crystal tilting. Out-of-plane Bragg diffraction patterns and RSMs were recorded to measure the lattice parameters of the WO_x films. Atomic force microscopy (AFM, Nanocute, Hitachi Hi-Tech Sci. Co.) was used to observe the surface morphology of the films. The σ and S of the resultant WO_x films were measured by Van der Pauw method and steady- state method at RT. The atomic arrangement of the films was visualized using high-angle annular dark-field scanning transmission electron microscopy (HAADF-STEM). The TDTR simulation parameters are summarized in **Table 4-1**. For accuracy, 116-nm-thick Mo transducer on a glass substrate was measured separately. Since C_p does not vary significantly with x and was constrained within a small fluctuation around the reported single crystalline bulk values. [20]

Table 4-1. TDTR simulation parameters for analyzing WO_x films on $LaAlO_3$

Material	Parameter	Value
Mo	Density	10000 Kg m^{-3}
	C_p	250 J Kg^{-1} K^{-1} [19]
	κ	45.4 W m^{-1} K^{-1}
WO_x	Density	5880 – 9350 Kg m^{-3}
	C_p	312 – 319 J Kg^{-1} K^{-1} [20]
$LaAlO_3$	Density	6520 Kg m^{-3}
	C_p	427 J Kg^{-1} K^{-1} [21]
	κ	10.3 W m^{-1} K^{-1}

4.3 Results and discussion

The x in the WO_x films were successfully modulated from 2.787 to 2.977 as shown in **Figures 4-2(a)** and **4- 2(b)**, which were extracted from the XPS spectra. The volume fractions of W^{6+} and W^{5+} dynamically changed with decreasing x (**Figure 4-2(a)**). [22]. Coherent epitaxial growth was confirmed from the RSM (**Figure 4-3**); the in-plane lattice parameter is fixed with that of $LaAlO_3$ substrate. Intense diffraction peak of WO_x with Pendellösung fringes is observed around 001 $LaAlO_3$ in the out-of-plane XRD patterns (**Figure 4-2(c)**), indicating a strong orientation in WO_x. From the XRD results, lattice expansion from ~0.366 nm to ~0.385 nm was observed with decreasing x (**Figure 4-2(d)**). Streak-like RHEED pattern [inset of **Figure 4-2(d)**] was observed in the $WO_{2.787}$ film, confirming that the film was heteroepitaxially grown. Rectangular-shaped grains have a length of ~200 nm (long side) and ~20 nm (short side), forming a checkerboard-like pattern alternately in the plane which was observed in the topographic AFM image of the $WO_{2.787}$ film (**Figure 4-2(e)**).

The atomic arrangement of the films is visualized in **Figure 4-4**, which shows HAADF--STEM performed in the in-plane direction along the [100] $LaAlO_3$ substrate. Almost perfect square lattice is seen in the cross-sectional HAADF-STEM micrograph of $WO_{2.977}$ film (**Figure 4-4(a)**), indicating that the film is epitaxially grown on (001) $LaAlO_3$ substrate, which is epitaxially stabilized in a pseudo-tetragonal structure. Misfit dislocation was not observed at the heterointerface between the film and the substrate, confirming the coherent epitaxial growth. On the other hand, it was found that the atomic defects were formed when x is smaller than 2.955 in WO_x as shown in **Figures 4-4(b)** and **4-4(f)**. Since the STEM micrographs are the projection of atomic arrangements, these atomic defects are tunnel oriented along [100]. Furthermore, the density of the atomic defect tunnels increased with decreasing x in WO_x. In addition, the shape of the atomic defect tunnels became complex (**Figure 4-4(g)**) when the density of the atomic defect tunnels increased, probably due to the interactions and relaxations between these defects during the film growth. It should be noted that the atomic arrangement of oxygen-deficient WO_x with many atomic defect tunnels looks random, like an amorphous material. The oxygen-deficient WO_x films receive strong compressive strain from the substrate to forcefully stabilize the WO_3 structure. Therefore, these atomic defect tunnels are formed to release the stress during the film growth. Surprisingly, the epitaxial growth continues even above the atomic defect tunnels (**Figures 4-4(f)** and **4-4(g)**).

The electron and heat conduction properties of 1D atomic defect stabilized WO_x epitaxial films are shown in **Figure 4-5**. As schematically shown in **Figure 4-5(a)**, the κ_{obsd} was measured in the cross-plane direction, whereas the σ_{ave} was measured in the in-plane direction as shown in **Figure 4-5(c)**. The measured σ is defined as σ_{ave}, which is average of σ_1, σ_2, σ_3 and σ_4. With decreasing x from 2.98 to 2.92, κ in the cross-plane direction drastically decreases (**Figure 4-5(b)**), whereas the σ_{ave} drastically increases simultaneously (**Figure 4-5(d)**). Very similar decreasing tendency was also seen in the κ_{obsd} of WO_x epitaxial films grown on $LaAlO_3$ reported by Ning *et al*. [18] The κ_{obsd} of $WO_{2.97}$ was ~7 W m^{-1} K^{-1} and the value abruptly decreased to ~2 W m^{-1} K^{-1} with decreasing x to 2.92, then gently decreased with decreasing x (TDTR decay curves, **Figure 4-6**). The κ_{obsd} values of the WO_x films at $x \leq 2.92$ are close to those of amorphous WO_x film in chapter 3 [22], which shows the minimum κ [23] at the same chemical composition. On the other hand, the measured σ_{ave} in the in-plane direction of $WO_{2.97}$ was 0.07 S cm^{-1}, which reached to ~500 S cm^{-1} at $WO_{2.92}$. When x at 2.787, σ_{ave} and κ_{obsd} were 1500 S cm^{-1} and 1.65 W m^{-1} K^{-1}, respectively. This is due to the increase in both μ and n, which was confirmed from thermopower analyses (**Figure 4-7**).

Then, the low κ_{obsd} of the WO_x epitaxial films was analyzed with the Wiedemann-Frantz law to extract phonon and electron contributions in the heat conduction. Although the Wiedemann-Frantz law does not give a reliable $\kappa_{electon}$ for some TMOs (VO_2 [24]), the $\kappa_{electon}$ can be calculated in the case of the WO_x epitaxial films. The $\kappa_{electon}$ and $\kappa_{lattice}$ of the $WO_{2.92}$ film can be calculated as ~0.07 W m^{-1} K^{-1} and ~1.83 W m^{-1} K^{-1}, and the κ_{obsd} is close to that of amorphous $WO_{2.93}$ (1.4 W m^{-1} K^{-1}), which is quite low among the oxides [25]. Although amorphous $WO_{2.93}$ shows ~10^{-1} S cm^{-1}, the σ_{ave} of the epitaxial $WO_{2.92}$ is three orders of magnitude higher. Thus, by introducing the 1D atomic defect tunnels, phonon propagation is suppressed, but electron propagation is enhanced. Since the 1D atomic defect tunnel is spontaneously introduced upon oxygen removal while maintaining the epitaxial growth, high electron conduction and low heat conduction are realized together in the oxygen-deficient WO_x crystals.

4.4 Conclusion

This chapter demonstrated that high electron conduction and low heat conduction can coexist simultaneously in an oxide crystal: oxygen-deficient WO_x epitaxial film. Crystallographic analyses revealed that the resultant WO_x films contain 1D atomic defect tunnels in the in-plane direction, of which the density increased with decreasing x. The 1D atomic defect tunnels were randomly distributed along the long axis of rectangular-shaped WO_x grains. The cross-plane κ drastically decreased with increasing the 1D atomic defect tunnels due to suppressed phonon propagation, whereas the σ significantly increased. High electron conduction and low heat conduction coexist when $x < 2.92$. The present findings would be of great use for designing thermal management materials.

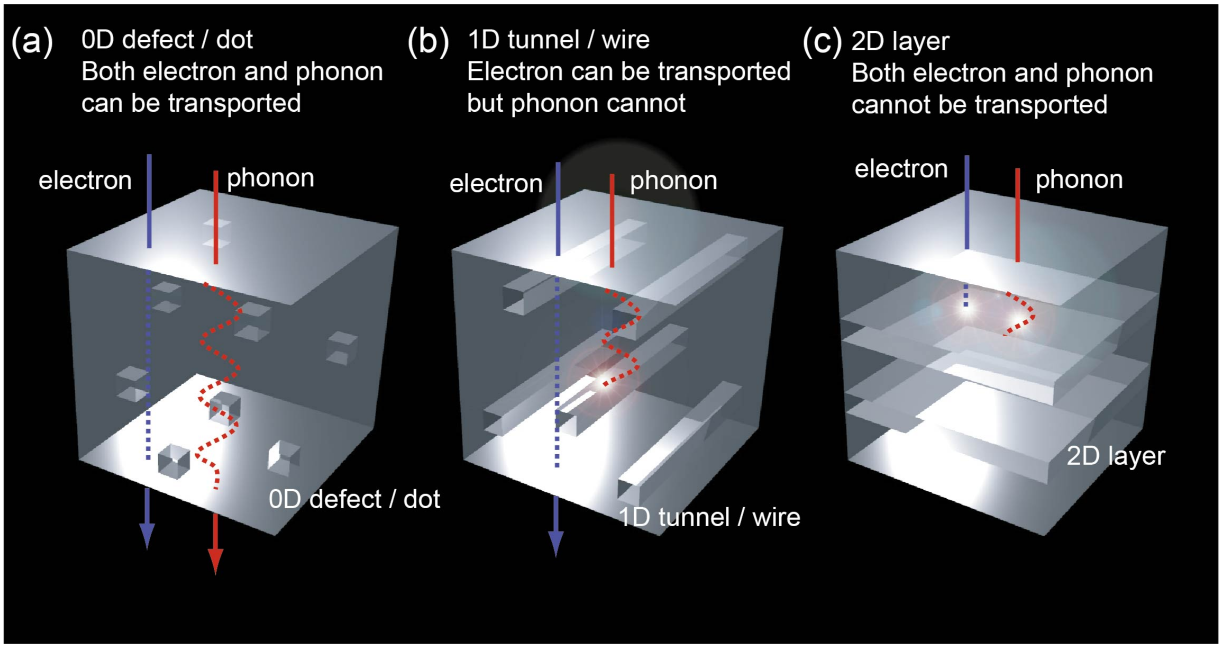

Figure 4-1. Nanostructuring concept to reduce heat conduction while keeping high electron conduction. Schematic illustrations of electron/phonon propagation in materials with (a) 0D defect (dot), (b) 1D tunnel (wire), and (c) 2D layer. (a) Electron and phonon can be transported without suppression because of the low probability of phonon hitting the vacancies. Electron transport is less sensitive to the defect. (b) the probability of that phonon hits the 1D tunnel is much higher than that of phonon being scattered by 0D defects. Therefore, low κ can be expected. (c) 2D layer insertion is effective in reducing κ. However, electrons are also scattered at the interface, which results in low σ and low κ.

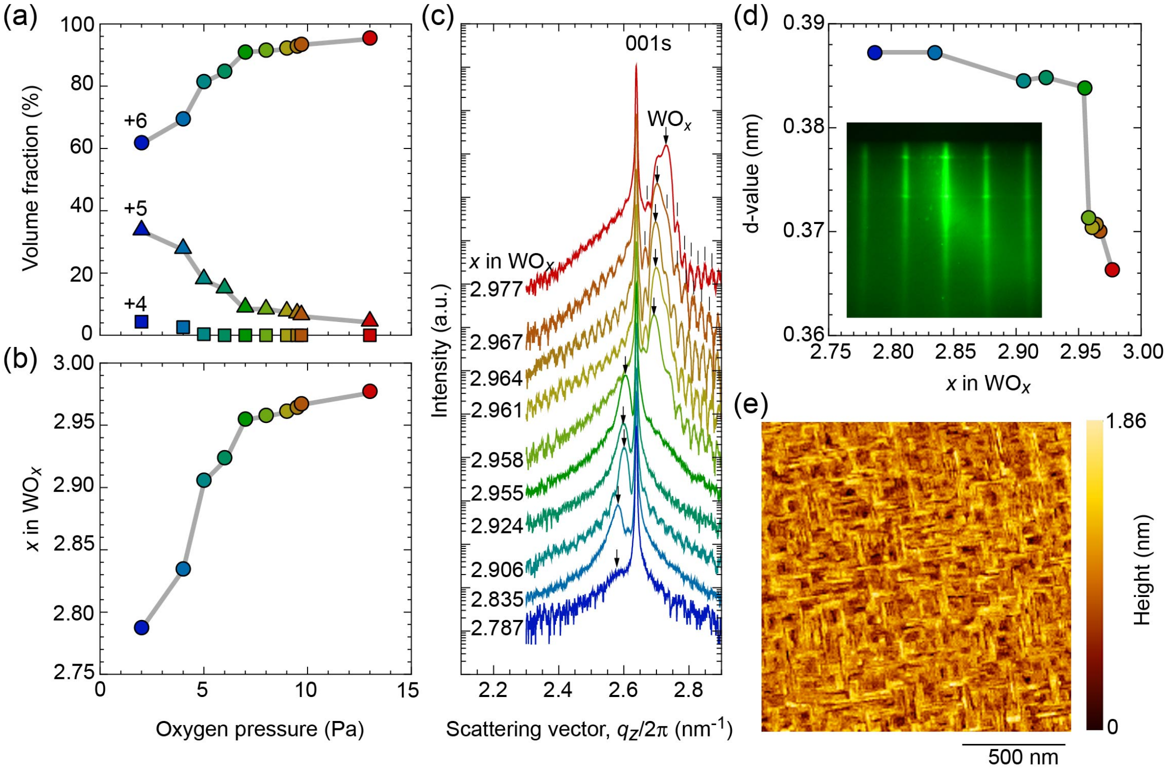

Figure 4-2. Change in the crystalline lattice of the WO$_x$ epitaxial films. (a) Volume fraction of W^{6+}, W^{5+}, and W^{4+} and (b) x in the WO$_x$ films as a function of the oxygen pressure during the film growth. The x in WO$_x$ was modulated from ~2.78 to ~2.98. (c) Out-of-plane XRD patterns of the WO$_x$ films around 001 LaAlO$_3$. The arrows indicate the diffraction peak position of WO$_x$, and the short lines indicate Pendellösung fringes. (d) Change in the out-of-plane lattice spacing of WO$_x$. The inset shows the RHEED pattern of the WO$_{2.787}$ film, confirming the successful heteroepitaxial growth. (e) Topographic AFM image of the WO$_{2.787}$ film.

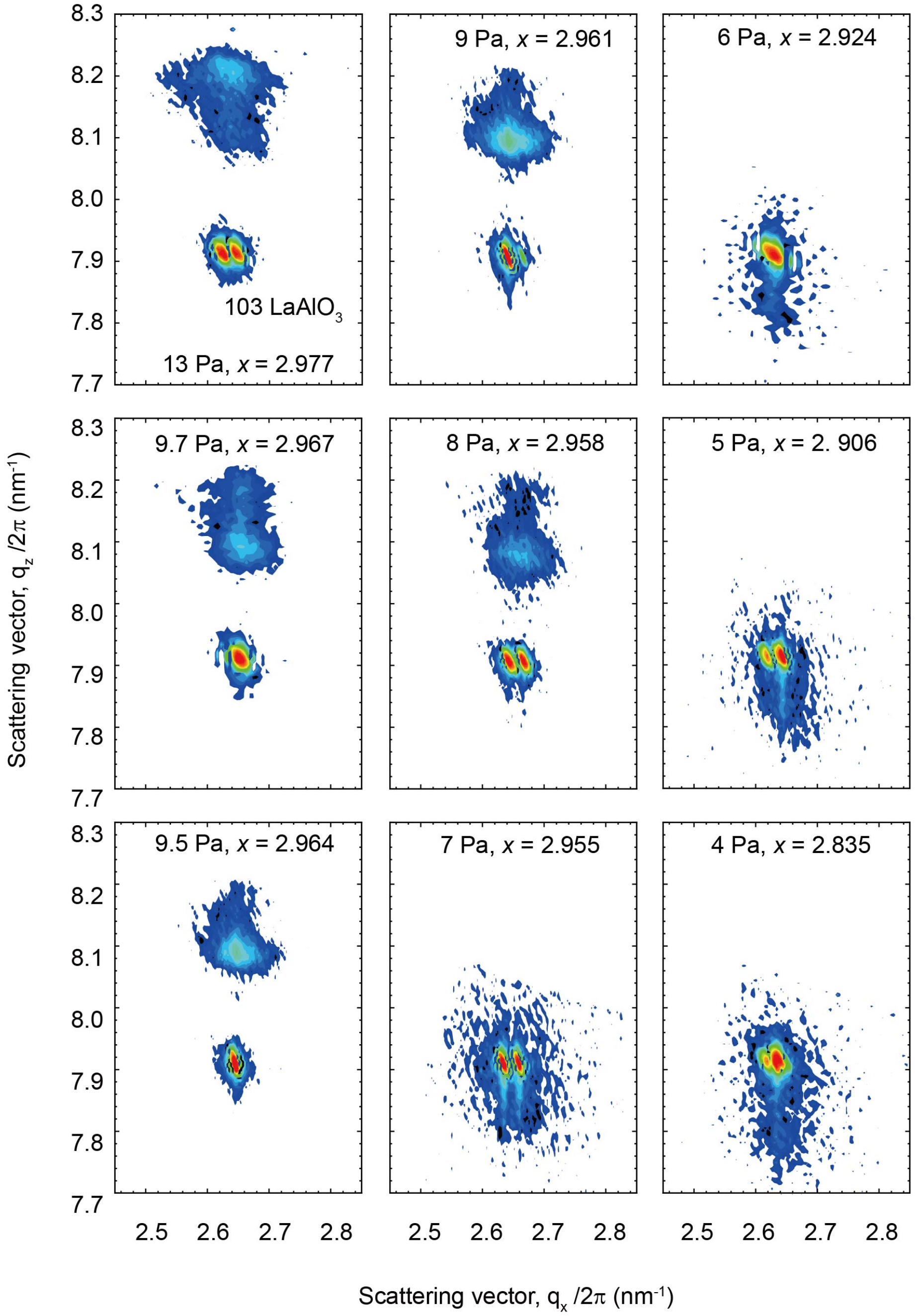

Figure 4-3. RSMs of the WO$_x$ films. The diffraction spots of WO$_x$ are located at the same q_x/2π position with those of 103 LaAlO$_3$ substrates, indicating coherent epitaxial growth in all cases.

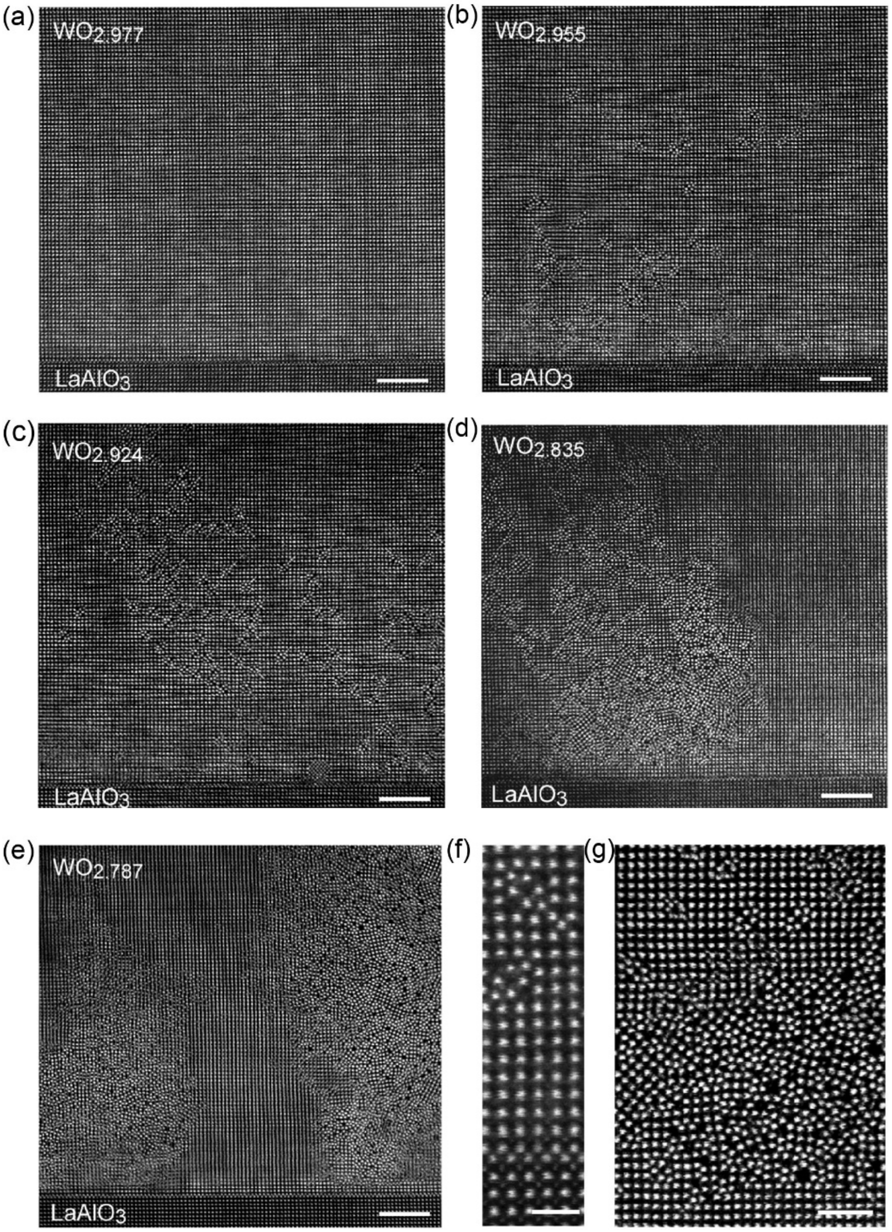

Figure 4-4. Evolution of 1D atomic defect tunnel in the oxygen-deficient (001) WO_x epitaxial films. Cross-sectional HAADF-STEM micrographs of (a) $WO_{2.977}$, (b) $WO_{2.955}$, (c) $WO_{2.924}$, (d) $WO_{2.835}$, and (e) $WO_{2.787}$ films. (f) Atomic structure of the 1D atomic defects in (b). (g) Atomic structure of high-density 1D atomic defect in (e). The scale bar is 5 nm for (a)−(e), 1 nm for (f), and 2 nm for (g).

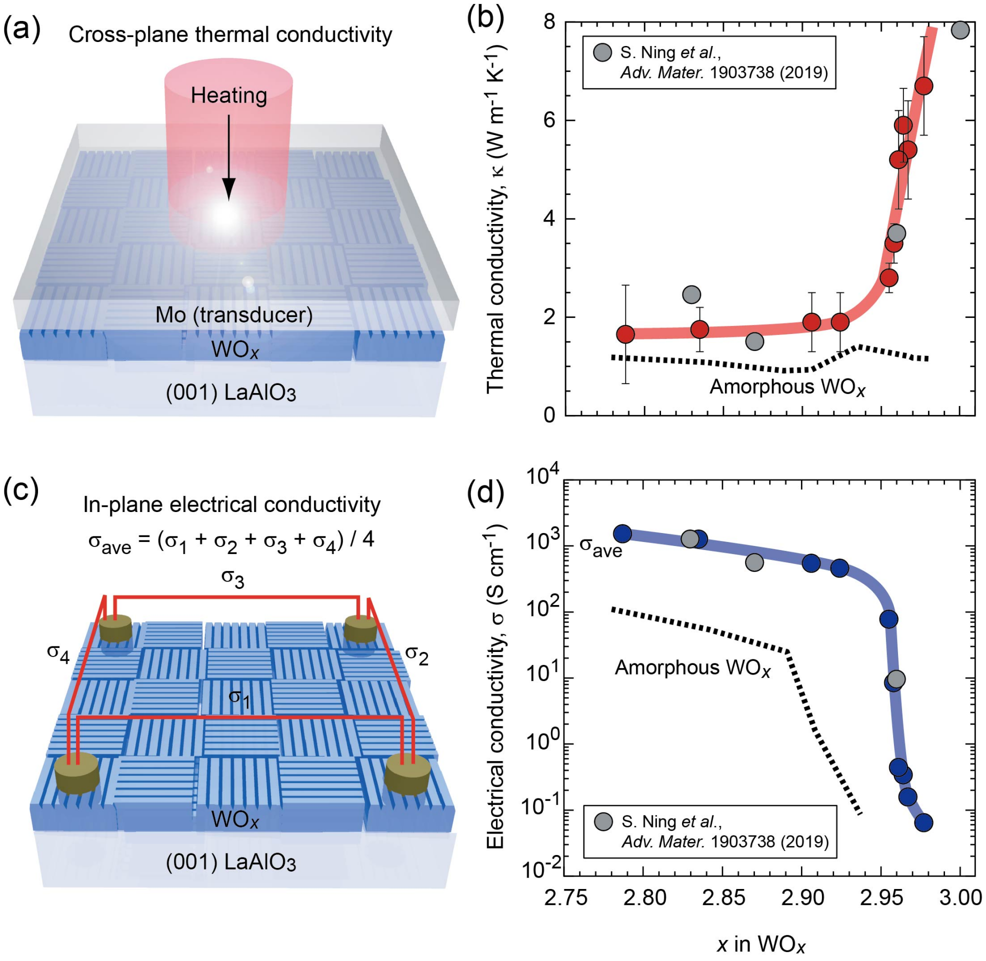

Figure 4-5. **Coexistence of high electron conduction and low heat conduction in the WO$_x$ epitaxial films with 1D atomic defect tunnels.** (a) Schematic illustration of the TDTR. (b) Cross-plane κ_{obsd} extracted from the TDTR measurement. (c) σ measurement. (d) In-plane σ_{ave}. Dashed line: amorphous WO$_x$ films [22] and Gray circles: epitaxial WO$_x$ films [18].

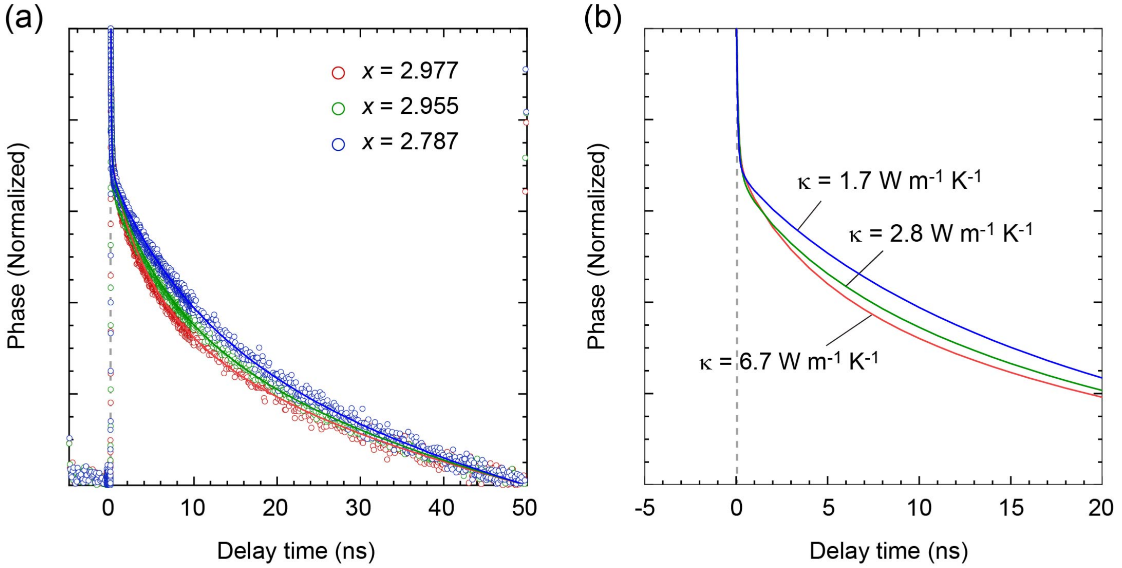

Figure 4-6. Normalized decay curve of the TDTR phase signal. (a) The thermal decay curves of $WO_{2.977}$, $WO_{2.955}$ and $WO_{2.787}$ display clear differences in κ_{obsd} for various WO_x films. (b) The simulated κ are 6.7 W m^{-1} K^{-1} ($WO_{2.977}$), 2.8 W m^{-1} K^{-1} ($WO_{2.955}$) and 1.7 W m^{-1} K^{-1} ($WO_{2.787}$), respectively.

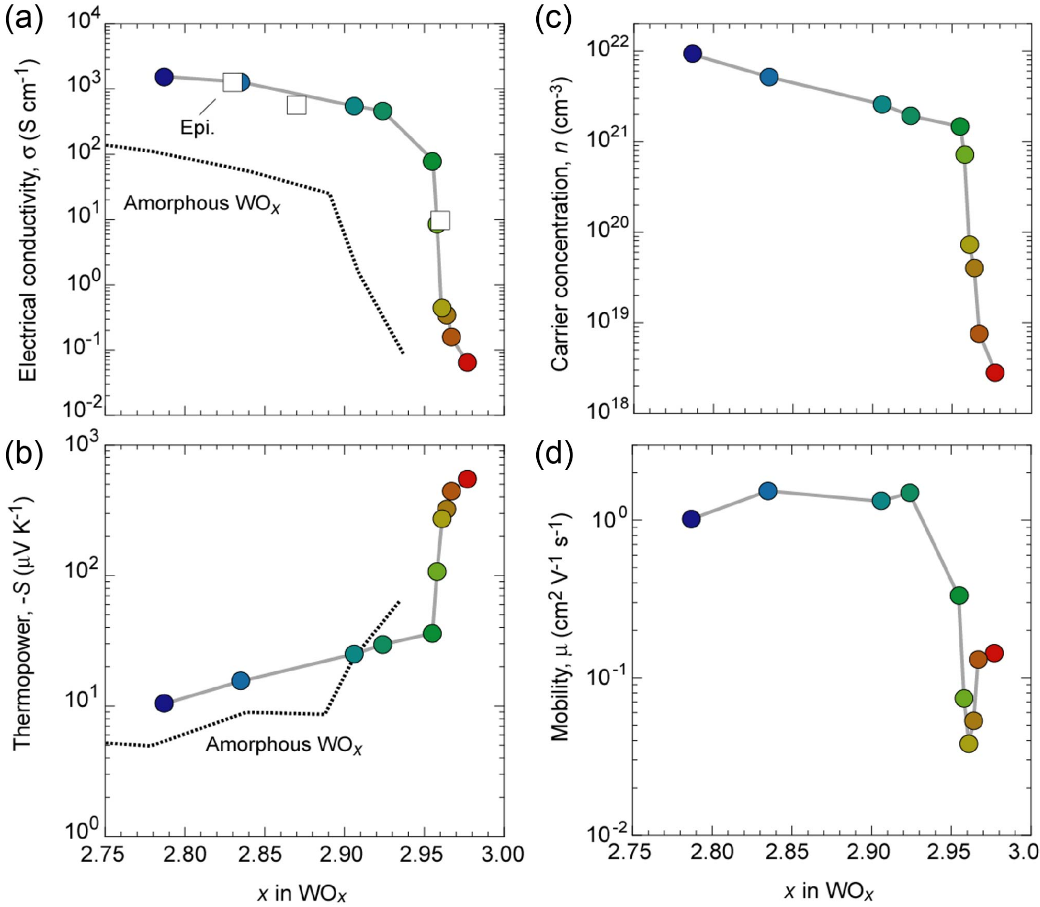

Figure 4-7. In-plane electron transport properties of the WO$_x$ films. Dashed line: amorphous WO$_x$ films[22] and Gray circles: epitaxial WO$_x$ films[18]. (a) In-plane σ. (b) The absolute values of S. (c) The n. (d) The μ. All transport properties show drastic change with x ranging from 2.98 to 2.92. Note both n and μ increase with increasing 1D atomic defect tunnel.

References

[1] K. F. Hsu, S. Loo, F. Guo, W. Chen, J. S. Dyck, C. Uher, T. Hogan, E. Polychroniadis, and M. G. Kanatzidis, *Science* **303**, 818 (2004).

[2] M. N. Luckyanova, D. Chen, W. Ma, H. L. Tuller, G. Chen, and B. Yildiz, *Appl. Phys. Lett.* **104**, 061911 (2014).

[3] E. A. Scott, K. Hattar, C. M. Rost, J. T. Gaskins, M. Fazli, C. Ganski, C. Li, T. Bai, Y. Wang, K. Esfarjani, M. Goorsky, and P. E. Hopkins, *Phys. Rev. Mater.* **2**, 095001 (2018).

[4] B. Dongre, J. Carrete, S. Wen, J. Ma, W. Li, N. Mingo, and G. K. H. Madsen, *J. Mater. Chem. A* **8**, 1273 (2020).

[5] R. Venkatasubramanian, E. Siivola, T. Colpitts, and B. O'Quinn, *Nature* **413**, 597 (2001).

[6] J. Ravichandran, A. K. Yadav, R. Cheaito, P. B. Rossen, A. Soukiassian, S. Suresha, J. C. Duda, B. M. Foley, C. H. Lee, Y. Zhu, A. W. Lichtenberger, J. E. Moore, D. A. Muller, D. G. Schlom, P. E. Hopkins, A. Majumdar, R. Ramesh, and M. A. Zurbuchen, *Nat. Mater.* **13**, 168 (2014).

[7] E. Dechaumphai, D. Lu, J. J. Kan, J. Moon, E. E. Fullerton, Z. Liu, and R. Chen, *Nano Lett.* **14**, 2448 (2014).

[8] C. J. Vineis, A. Shakouri, A. Majumdar, and M. G. Kanatzidis, *Adv. Mater.* **22**, 3970 (2010).

[9] H. Sy and C. Ong, *Solid State Commun.* **52**, 881 (1984).

[10] Y. Yuan, S. M. Wood, K. He, W. Yao, D. Tompsett, J. Lu, A. Nie, M. S. Islam, and R. Shahbazian-Yassar, *ACS nano* **10**, 539 (2016).

[11] D. Yin, C. Chen, M. Saito, K. Inoue, and Y. Ikuhara, *Nat. Mater.* **18**, 19 (2019).

[12] A. Magnéli, *Nature* **169**, 791 (1952).

[13] C. C. Mardare and A. W. Hassel, *Phys. Status Solidi A* **216**, 1900047 (2019).

[14] X. Leng, J. Pereiro, J. Strle, A. Bollinger, and I. Božović, *APL materials* **3**, 096102 (2015).

[15] S. Nishihaya, M. Uchida, Y. Kozuka, Y. Iwasa, M. Kawasaki, S. Nishihaya, M. Uchida, Y. Kozuka, Y. Iwasa, and M. Kawasaki, *ACS Appl. Mater. Interfaces* **8**, 22330 (2016).

[16] M. Wang, S. Shen, J. Ni, N. Lu, Z. Li, H. B. Li, S. Yang, T. Chen, J. Guo, and Y. Wang, *Adv. Mater.* **29**, 1703628 (2017).

[17] G. Mattoni, A. Filippetti, N. Manca, P. Zubko, and A. D. Caviglia, *Phys. Rev. Mater.* **2**, 053402 (2018).

[18] S. Ning, S. C. Huberman, Z. Ding, H. H. Nahm, Y. H. Kim, H. S. Kim, G. Chen, and C. A. Ross, *Adv. Mater.* **31**, 1903738 (2019).

[19] L. Khriplovich and I. Paukov, *J. Chem. Thermodyn* **15**, 333 (1983).

[20] F. Sale, *Thermochim. Acta* **30**, 163 (1979).

[21] W. Schnelle, R. Fischer, and E. Gmelin, *J. Phys. D: Appl. Phys.* **34**, 846 (2001).

[22] G. Kim, H. J. Cho, Y.-M. Sheu, and H. Ohta, *J. Phys. Chem. C* **123**, 15419 (2019).

[23] M. T. Agne, R. Hanus, and G. J. Snyder, *Energy Environ. Sci.* **11**, 609 (2018).

[24] S. Lee, K. Hippalgaonkar, F. Yang, J. Hong, C. Ko, J. Suh, K. Liu, K. Wang, J. J. Urban, and X. Zhang, *Science* **355**, 371 (2017).

[25] M. R. Winter and D. R. Clarke, *J. Am. Ceram. Soc.* **90**, 533 (2007).

Chapter 5. Anisotropy of electrical conductivity in tungsten oxide films with 1D atomic defect tunnel

5.1 Objective

Materials having an anisotropic crystal structure often exhibit anisotropy in σ. [1-9] Since there are wide varieties of crystal structures in complex TMOs, many complex TMOs exhibit anisotropy in σ as summarized in **Table 5-1**. [10-15] For example, the σ of hollandite $BaRu_6O_{12}$ along the double chain of edge-sharing RuO_6 is ~6 times larger compare to the perpendicular direction at 300K. [16] In the case of perovskite layered structure, $YBa_2Cu_3O_y$ ($6.6 \leq y \leq 7$), the in-plane σ along the CuO chain has 1.2~2.7 times larger than that across CuO chain direction. [15] However, simple TMO that exhibits anisotropy in the σ is rare due to their simple crystal structure. One exception is NbO_2. [17] Since the overlap integral of 4d orbitals in NbO_2 which is the major component of the conduction band is relatively small, the σ decreases when the bond angle of Nb−O−Nb is distorted from 180°. On the other hand, the overlap integral of widely spread 5d orbitals in TMOs is large, and therefore, the σ is less sensitive to the bond angle of TM−O−TM. Hence, it is difficult to find simple 5d TMOs that exhibit anisotropy in the σ.

Among many simple 5d TMOs, oxygen-deficient tungsten oxide (WO_x) is likely to have anisotropic σ. There is 1D defect tunnel structure in the $WO_{2.72}$, which has an anisotropic crystal structure (**Figure 5-1(a)**, unit cell). [18] There are also one-dimensional vacancy channels in the WO_x crystal (**Figure 5-1(b)**, yellow ring). Due to this unique anisotropic crystal structure, which was partially addressed in chapter 4, large anisotropic σ between along and across the tunnels can be expected. If 1D defect tunnel studied in chapter 4 can be aligned one directionally, the resulting WO_x structure will likely show different σ along and across direction of the 1D defect tunnel direction. In order to realize such a structure, investigating the similarity of crystal structure between WO_x and the substrate is very important. The $[1\bar{1}0]$ of (110)-oriented $LaAlO_3$ has small lattice mismatch with the *c*-axis of $WO_{2.72}$. Although there is almost no similarity in the atomic arrangement between WO_x along the *b*-axis and $LaAlO_3$ along [001], the distance between the two neighboring oxygens in WO_x along the *c*-axis and that in $LaAlO_3$ along $[1\bar{1}0]$ are the same (0.379 nm). In addition, chapter 4 revealed that the oxygen content x in WO_x can be controlled by modulating the oxygen pressure during the WO_x film deposition by PLD. [19] Therefore, WO_x film with aligned 1D tunnels can be grown on $LaAlO_3$ single crystal substrate.

This chapter demonstrates that oxygen-deficient WO_x epitaxial films with 1D atomic defect tunnels exhibit a large anisotropy in σ. Several WO_x films were fabricated with highly dense atomic defect tunnels, which were aligned one dimensionally along [001] $LaAlO_3$ by PLD technique. The resultant 1D atomic defect tunnels indeed showed a large anisotropy in their σ, which will be useful for designing simple TMOs with an anisotropic σ.

Table 5-1. Anisotropy in σ of transition metal oxide at 300K.

Material	**Anisotropy (σ_x/σ_y)**	**Structure**	**TMO outer orbital**	**Ref.**
$SrNbO_{3.41}$	~3000	Layered perovskite	4d	[10]
$Ba_{1.2}Rh_8O_{16}$	~3.3	Pseudo-hollandite	4d	[11]
$BaRu_6O_{12}$	~ 6	Hollandite	4d	[16]
$Li_{0.9}Mo_6O_{17}$	~ 260	Bronze (Superlattice)	4d	[14]
NaV_2O_4	~ 2.1	Calcium-ferrite type structure	3d	[13]
$YBa_2Cu_3O_y$ ($6.5 \leq y \leq 7$)	1.2~2.7	Layered perovskite	3d	[15]
NbO_2	~2.7	Rutile	4d	[17]

5.2 Film synthesis and characterizations

Oxygen-deficient WO_x epitaxial films were heteroepitaxially grown on lattice-matched (110) $LaAlO_3$ substrate by PLD technique at 600 °C under controlled oxygen atmospheres (4.0 – 8.3 Pa). The fluence and repetition rate were set to ~1 J cm^{-2} pulse^{-1} and 10 Hz, respectively. The typical growth rate was ~15 pm pulse^{-1}, and the film thickness was ~45 nm in all cases. The diffraction patterns from HRXRD and RSMs were used to analyze the lattice characteristics of the WO_x films. The film surface was observed by AFM. The atomic arrangement was visualized using HAADF-STEM. The σ of the WO_x films was measured along [100] and [$1\bar{1}0$] $LaAlO_3$ substrate by d.c. four-point probe method with four equally-spaced, co-linear probes at a temperature ranging 30 – 300 K. The S was also measured at

RT. The XAS O *K*-edge spectrum was measured from 525 to 560 eV at RT to examine the electronic structure of WO_x films.

5.3 Results and discussion

Oxygen-deficient WO_x films were successfully fabricated on (110)-oriented $LaAlO_3$ single crystal substrates, and the x in the WO_x films was modulated from 2.778 to 3. **Figure 5-2(a)** shows the out-of-plane XRD pattern of the WO_x films around the 110 diffraction peak of the $LaAlO_3$ substrate. At $x = 3$, an intense diffraction peak of 110 WO_3 (assuming ReO_3 structure) is observed at $q_z/2\pi = 3.8$ nm^{-1} together with Pendellösung fringes (|), indicating a strong (110) orientation of the film. With decreasing x, the peak intensity decreases, and the peak position shifts to the lower $q_z/2\pi$ side, indicating that the orientation of WO_x crystal becomes weak. It also indicates that the lattice expansion with decreasing x as shown in **Figure 5-2(b)**. Since the ionic radius of W^{5+} (0.62 Å) is larger than that of W^{6+} (0.60 Å), the lattice expansion is attributed to the removal of oxygen from ReO_3-type WO_3 lattice. The surface morphologies of the WO_3 and $WO_{2.778}$ films are shown in **Figure 5-2(c)** and **5-2(d)**. The WO_3 film surface is smooth and composed of tiny grains without special features, whereas the $WO_{2.778}$ surface shows an anisotropic structure composed of long rectangular shaped grains (L ~600 nm, W ~20 nm) aligned along [001]. The RHEED patterns of the WO_3 (**Figure 5-2(e)**) and $WO_{2.778}$ (**Figure 5-2(f)**) films clearly indicate the structural difference: intense streak RHEED patterns were manifested in **Figure 5-2(e)**, indicating the strong preferred orientation and the smooth surface of the WO_3 film. On the other hand, intense streak RHEED pattern was seen in the azimuth of $[1\bar{1}0]$ (**Figure 5-2(f)**), and halo-like

RHEED pattern was manifested in the azimuth of [001]. This clearly indicates that there is a 1D lattice along [001] while the atomic arrangement along $[1\bar{1}0]$ is almost random.

To further clarify the anisotropic structure, RSMs around the Bragg diffraction spots of $22\bar{2}$ $LaAlO_3$ and 310 $LaAlO_3$ were measured. An intense diffraction spot of $44\bar{4}$ WO_3 was seen together with $22\bar{2}$ $LaAlO_3$ when the azimuth is [001] (**Figure 5-3(a)**), and two intense diffraction spots of 620 and 230 WO_3 were observed together with 310 $LaAlO_3$ when the azimuth was $[1\bar{1}0]$ (**Figure 5-3(b)**). An intense spot of $WO_{2.778}$ was seen together with $22\bar{2}$ $LaAlO_3$ spot when the azimuth was [001] (**Figure 5-3(c)**). Weak tail in the q_z direction was also observed. On the other hand, a very broad streak of $WO_{2.778}$ was observed together with 310 $LaAlO_3$ when the azimuth was $[1\bar{1}0]$ (**Figure 5-3(d)**), indicating that the lateral coherence length along $[1\bar{1}0]$ is extremely short. It should be noted that the in-plane peak position ($q_{[001]}/2\pi$) of the WO_3 and $WO_{2.778}$ peaks was the same with that of $LaAlO_3$, indicating that coherent epitaxial growth occurred in all cases. These results show almost uniaxially oriented oxygen deficient WO_x films along [001] were successfully fabricated on (110) $LaAlO_3$ substrate.

HAADF-STEM observations of the $WO_{2.778}$ film was performed. Disordered atomic columns were observed along [001] (**Figures 5-4(a)** and **5-4(c)**) together with many dot-like dark contrast, whereas ordered stripes were observed along $[1\bar{1}0]$ (**Figures 5-4(b)** and **5-4(d)**). The diameter of the dot-like contrast was ~0.3 nm, which was distributed in the surroundings of randomly distributed atomic column. Sharp interface is seen from energydispersive X-ray spectroscopy (EDS) mappings, indicating that there is no chemical reaction between $WO_{2.778}$ film and $LaAlO_3$ substrate. (**Figure 5-5**) These observations revealed that the 1D atomic defect tunnels are aligned along the long axis of the rectangular-shaped grains, and high-density atomic defect tunnels were successfully stabilized one dimensionally in the $WO_{2.778}$ film.

Although the detailed crystal growth mechanism of the $WO_{2.778}$ film remains unclear, the following can be suspected. Since the oxygen sublattices of the $WO_{2.778}$ and (110) $LaAlO_3$ are matched well along [001] but not well along $[1\bar{1}0]$, uniaxially orientated crystal growth occurs. During the film growth, atomic arrangement moves, and the 1D atomic defect tunnels are formed to minimize the energy.

The σ of the resultant WO_x films measured along the [001] and $[1\bar{1}0]$ is shown in **Figure 5-6**. The σ increased from ~0.4 to ~5 S cm^{-1} with decreasing x from 2.987 to 2.960 in both directions. (**Figure 5-6(a)**) The electron configuration of W^{5+} is $5d^1$, and the d-electron plays as the carrier electron. Therefore, the σ increased with decreasing x. If $x < 2.96$, the σ along [001] was always higher than that along $[1\bar{1}0]$, indicating the anisotropy in the σ. The anisotropy increased with decreasing x. When $x = 2.778$, the σ along [001] was 1700 S cm^{-1} while that along $[1\bar{1}0]$ was 360 S cm^{-1}, resulting in an anisotropic ratio of σ ~5. In order to clarify the origin of this anisotropy, S was measured. (**Figure 5-6(b)**) The absolute values of S decreased from ~360 to ~20 μV K^{-1} with decreasing x regardless of the directions. This indicates that the n increased with decreasing x, and there is no anisotropy in the n. Inset of

Figure 5-6(b) shows Jonker plot of $x = 2.778$, 2.82 and 2.853, which reveals that the μ along [001] is higher than that along $[1\bar{1}0]$.

Figure 5-7(a) shows the σ–T curves of the films. The σ along [001] is always higher than that along $[1\bar{1}0]$. The σ increased with increasing temperature in all cases, and the respective E_a near RT was plotted in **Figure 5-7(b)** as a function of x in WO_x. The E_a decreased with decreasing x. If $x < 2.96$, the E_a along [001] is clearly smaller than that along $[1\bar{1}0]$. Since there is no anisotropy in the n, the difference in the E_a reflects the anisotropy in μ. There are two possible origins: difference in the τ and difference in the m^*.

In order to clarify the origin of the anisotropy in the σ, XAS was performed. The O K-edge spectra of $WO_{2.853}$ with linearly-polarized beams are shown in **Figure 5-8 (a)**. The beam along the tunnel is donated as $E_{//}$ while that across the tunnel is donated as $E_{\perp}$. In **Figure 5-8(b)**, the peak A and B refer to O 2p−W 5d t_{2g} hybridization, C and D refer to O 2p−W 5d e_g hybridization, and E and F refer to O 2p−W 6sp hybridization, respectively. [20-22] There is no significant difference between the XAS spectra across and along the tunnel, indicating that the anisotropy in the electronic structure is small, most likely due to widely spread W 5d orbitals. Since there is no significant difference in peak A and B, the anisotropy in the carrier effective mass is negligible. This result reveals that the anisotropic σ values are originated by the discrepancy in the τ. In other words, the 1D atomic defect tunnels scatter carrier electrons.

5.4 Conclusion

In this chapter, the anisotropy in the σ of oxygen-deficient WO_x with the anisotropic crystal structure was explored. The WO_x films were grown on lattice matched $LaAlO_3$ substrate by PLD technique under controlled oxygen atmosphere. The crystallographic analyses of the WO_x films revealed that highly dense atomic defect tunnels were aligned one dimensionally along [100] $LaAlO_3$. The σ along the 1D atomic defect tunnels was ~5 times larger than that across the tunnels; at $x = 2.778$, the σ along [001] was 1700 S cm^{-1} whereas that along $[1\bar{1}0]$ was 360 S cm^{-1}. The origin of this anisotropy of σ is the difference between the crystal structure along [001] and along $[1\bar{1}0]$, which are attributed to the formation of the 1D atomic defect tunnels. The present approach, introduction of 1D atomic defect tunnels, is useful to design simple TMOs exhibiting anisotropic σ.

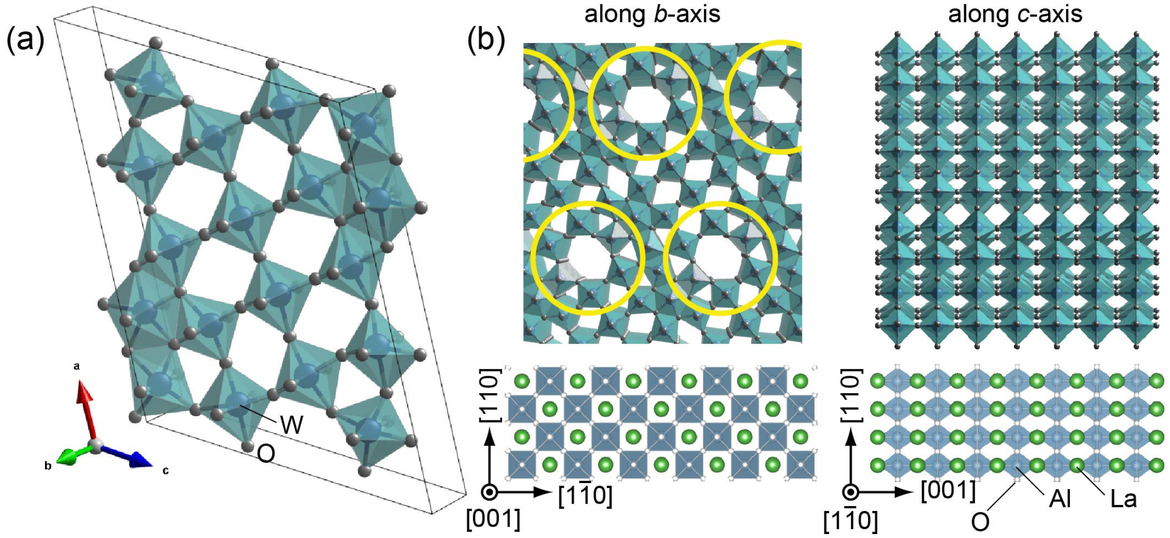

Figure 5-1. **Schematic crystal structure of $WO_{2.72}$.** (a) Unit cell of $WO_{2.72}$ (b) Side (or cross-sectional) views based on predicted film growth of oxygen deficient WO_x on (110) oriented $LaAlO_3$ substrate. There is no similarity in the atomic arrangement between WO_x along *b*-axis and $LaAlO_3$ along [001]. On the other hand, the distance between two neighboring oxygens in WO_x along *c*-axis and $LaAlO_3$ along [1$\bar{1}$0] is the same (0.379 nm).

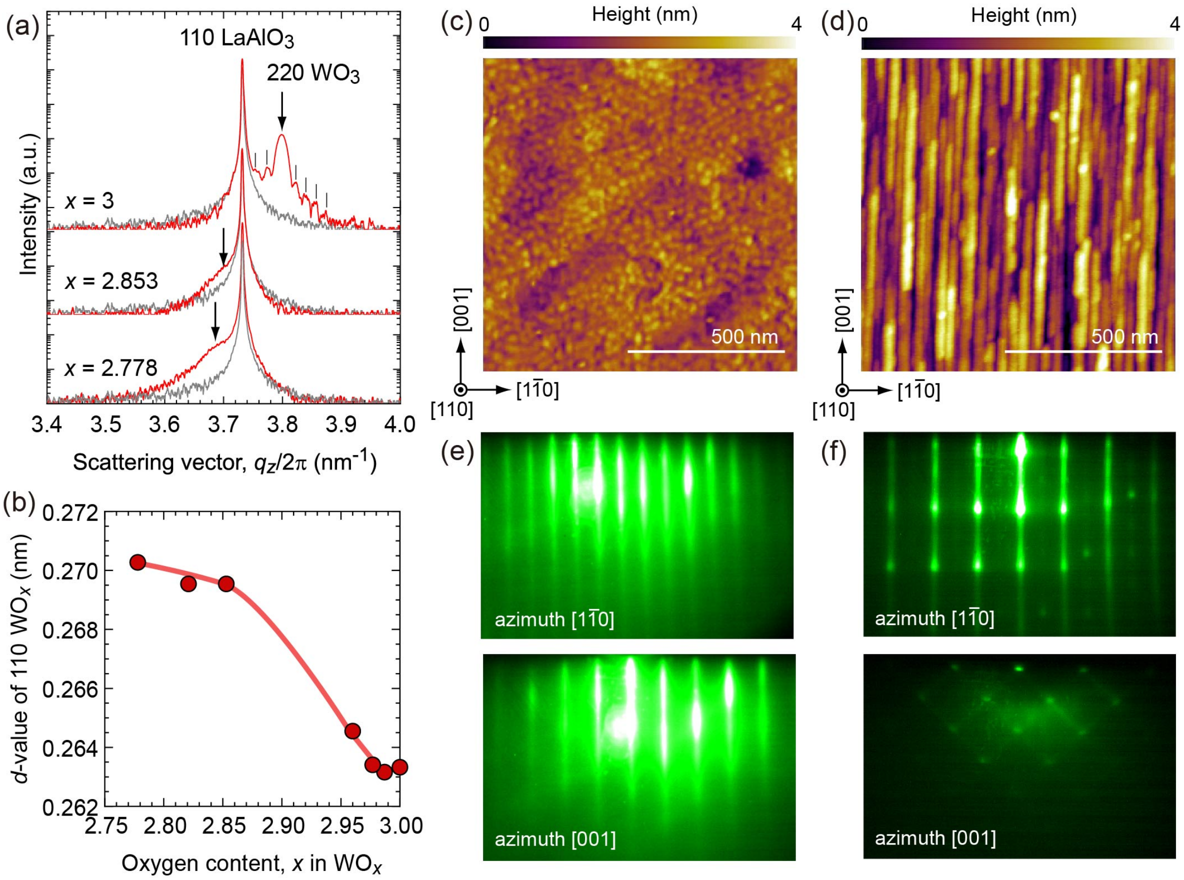

Figure 5-2. **Change in the crystalline lattice of the WO$_x$ epitaxial films.** (a) Out-of-plane XRD patterns of the WO$_x$ films around 110 LaAlO$_3$. The gray dashed line indicates bare LaAlO$_3$ substrate. The diffraction peak position of WO$_x$ is indicated with arrow (↓). (b) Change in the *d*-value of 110 WO$_x$. The *d*-value increases with decreasing *x*. Topographic AFM images of (c) WO$_3$ and (d) WO$_{2.778}$ epitaxial films. Structural anisotropy is clearly visualized in (d). RHEED patterns of (e) WO$_3$ and (f) WO$_{2.778}$ epitaxial films. The labelled directions on AFM images and RHEEED patterns are the crystal directions of LaAlO$_3$ substrate.

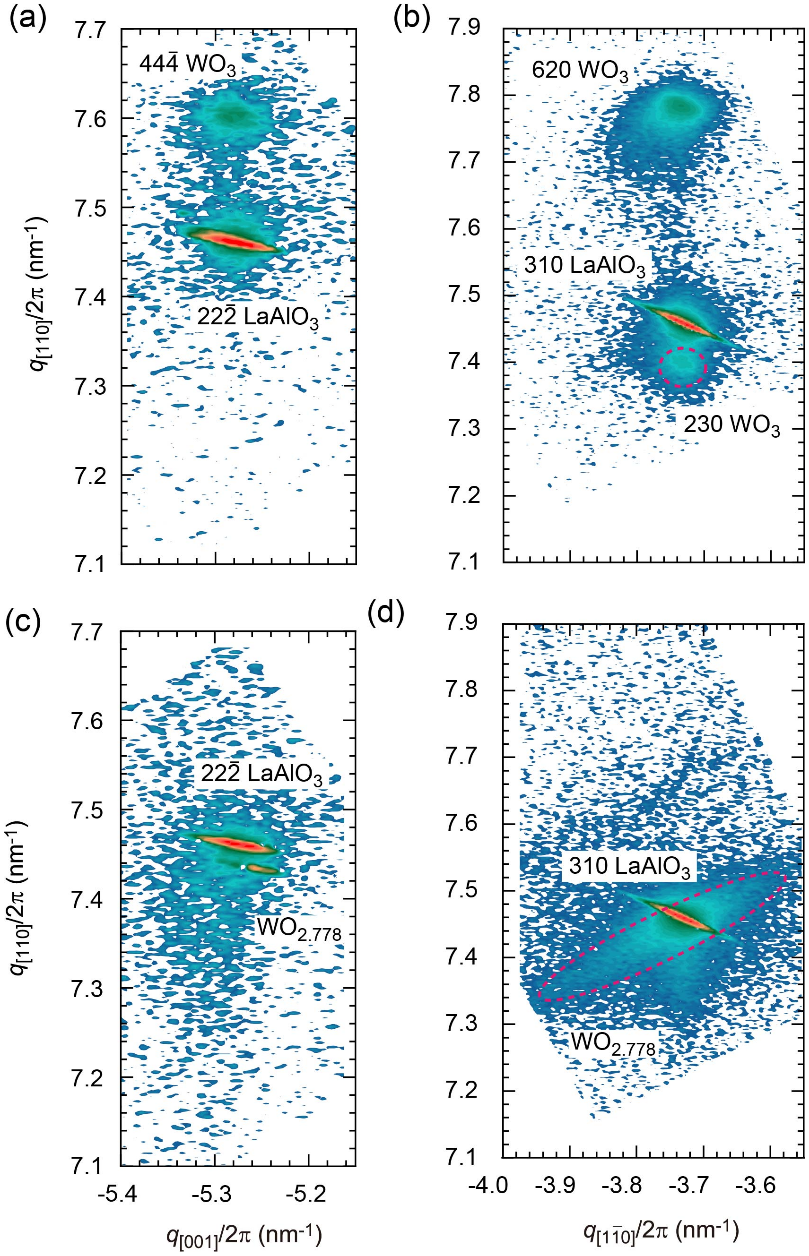

Figure 5-3. RSMs of the WO$_x$ films. RSMs of (a), (b) WO$_3$ and (c), (d) WO$_{2.778}$. The diffraction spots of WO$_3$ and WO$_{2.778}$ are located at the same $q_{[001]}/2\pi$ position with $22\bar{2}$ LaAlO$_3$ substrate. The diffraction spots of WO$_3$ and WO$_{2.778}$ are located at the same $q_{[1\text{-}10]}/2\pi$ position with 310 LaAlO$_3$ substrate.

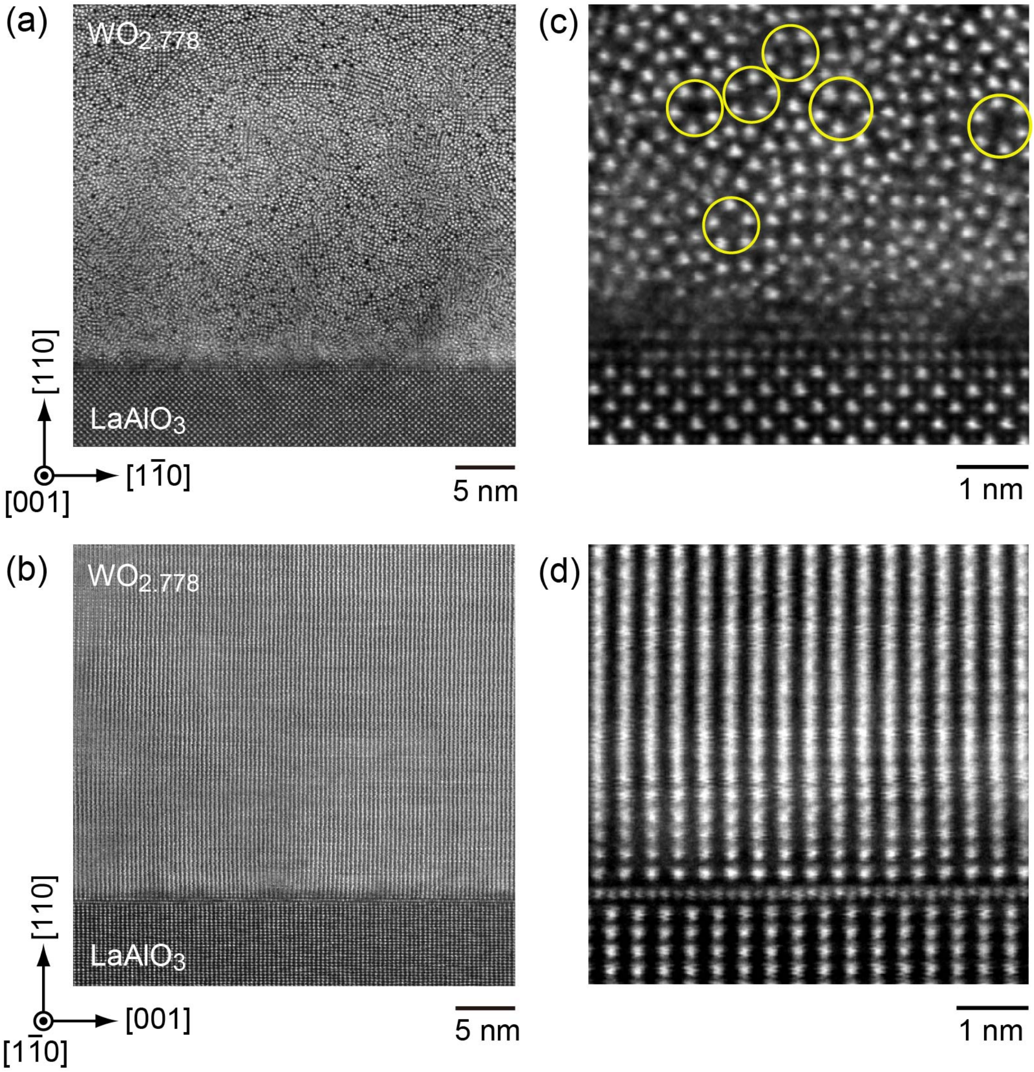

Figure 5-4. **Evolution of 1D atomic defect tunnel in the oxygen-deficient (110) WO$_x$ epitaxial films.** Cross-sectional HAADF-STEM images of the WO$_{2.778}$ film along (a) [001] and (b) [1$\bar{1}$0]. The scale bar is 5 nm. Highly dense atomic defect tunnels are clearly visualized along [001], whereas only square lattices are seen along [1$\bar{1}$0]. (c) and (d) show magnified atomic arrangements with 1 nm scale bar.

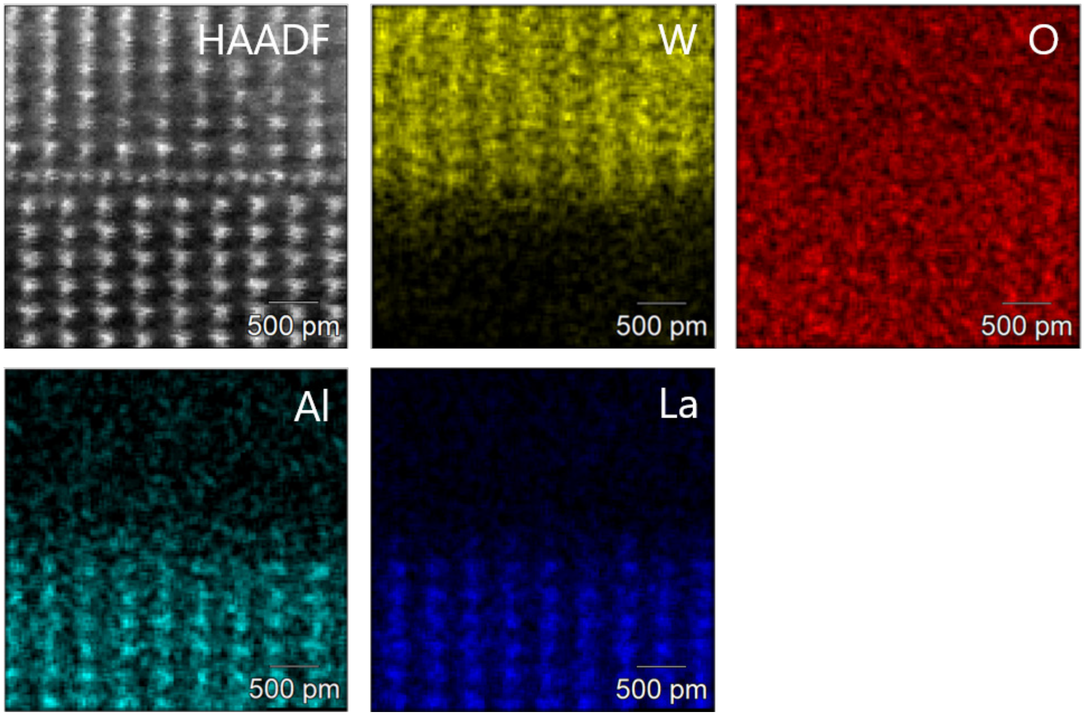

Figure 5-5. Atomic-resolution EDS mapping of the interface. Sharp interface is seen without chemical reaction between $WO_{2.778}$ film and $LaAlO_3$ substrate.

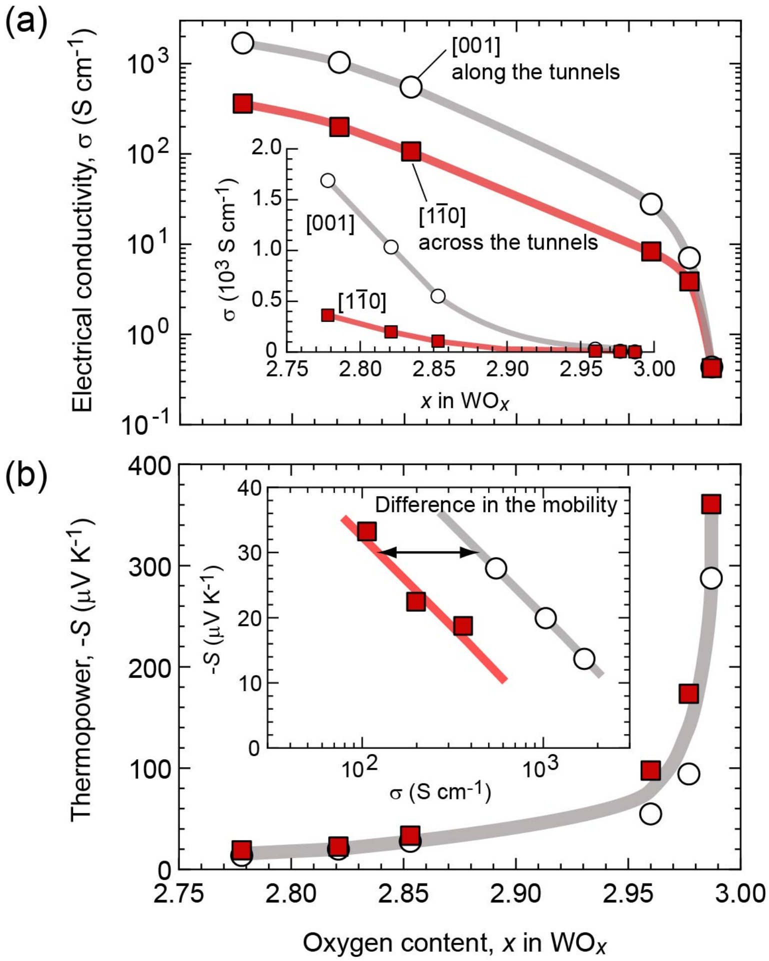

Figure 5-6. Electron transport properties of the WO$_x$ films. (a) σ and (b) S of the WO$_x$ films along [001] and [1$\bar{1}$0] at RT. (Inset in (a)) Linear scaled. (Inset in (b)) Jonker plot of x = 2.778, 2.82 and 2.853. When x < 2.98, anisotropy of the σ is obviously observed whereas such anisotropy of the S is not observed. The Jonker plot clearly indicates that the μ along [001] is higher than that along [1$\bar{1}$0].

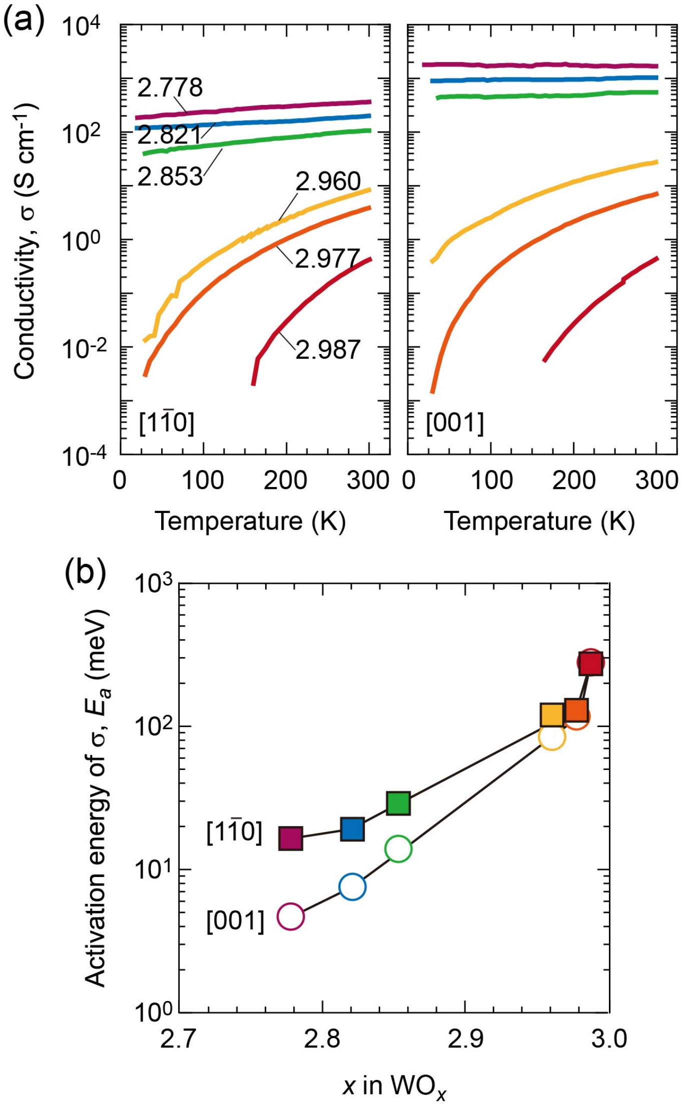

Figure 5-7. Temperature dependence of the σ of the WO$_x$ epitaxial films with 1D atomic defect tunnels. (a) The σ–T curve along the [1$\bar{1}$0] (left) and the [001] (right). (b) The E_a as function of x in WO$_x$.

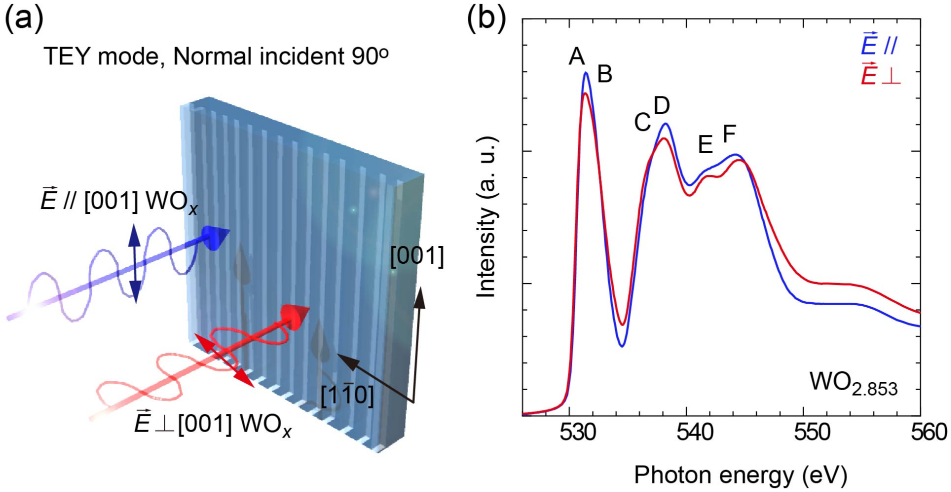

Figure 5-8. O K-edge spectra measured by XAS with TEY mode. (a) The linearly polarized beam incidence along the tunnel ($E_{//}$) and across the tunnel ($E_{\perp}$). (b) The peak A and B refer to O 2p–W 5d t_{2g} hybridization, C and D refer to O 2p–W 5d e_g hybridization, and E and F refer to O 2p–W 6sp hybridization, respectively. There is no significant difference in the peak A and B, indicating that the discrepancy in the carrier effective mass is negligible.

References

[1] E. Liu, Y. Fu, Y. Wang, Y. Feng, H. Liu, X. Wan, W. Zhou, B. Wang, L. Shao, and C.-H. Ho, *Nat. Commun.* **6**, 1 (2015).

[2] S. Afsari, P. Yasini, H. Peng, J. P. Perdew, and E. Borguet, *Angew. Chem. Int. Ed.* **58**, 14275 (2019).

[3] H. Wang, M.-L. Chen, M. Zhu, Y. Wang, B. Dong, X. Sun, X. Zhang, S. Cao, X. Li, and J. Huang, *Nat. Commun.* **10**, 1 (2019).

[4] M. Funahashi, *Mater. Chem. Front* **1**, 1137 (2017).

[5] S. Gong, Z. Zhu, and S. Meguid, *Polym.* **56**, 498 (2015).

[6] S. Zhao, B. Dong, H. Wang, H. Wang, Y. Zhang, Z. V. Han, and H. Zhang, *Nanoscale Adv.* **2**, 109 (2020).

[7] L.-D. Zhao, S.-H. Lo, Y. Zhang, H. Sun, G. Tan, C. Uher, C. Wolverton, V. P. Dravid, and M. G. Kanatzidis, *Nature* **508**, 373 (2014).

[8] C. Shen, J. E. Calderon, E. Barrios, M. Soliman, A. Khater, A. Jeyaranjan, L. Tetard, A. Gordon, S. Seal, and L. Zhai, *J. Mater. Chem. C* **5**, 11708 (2017).

[9] Y. Zhuang, K. Zheng, X. Cao, Q. Fan, G. Ye, J. Lu, J. Zhang, and Y. Ma, *ACS nano* **14**, 11733 (2020).

[10] C. Kuntscher, S. Schuppler, P. Haas, B. Gorshunov, M. Dressel, M. Grioni, F. Lichtenberg, A. Herrnberger, F. Mayr, and J. Mannhart, *Phys. Rev. Lett.* **89**, 236403 (2002).

[11] A. Pautrat and W. Kobayashi, *Phys. Rev. B* **82**, 115113 (2010).

[12] S. Huangfu, G. D. Jakub, X. Zhang, O. Blacque, P. Puphal, E. Pomjakushina, F. O. von Rohr, and A. Schilling, *Phys. Rev. B* **101**, 104104 (2020).

[13] K. Yamaura, M. Arai, A. Sato, A. Karki, D. Young, R. Movshovich, S. Okamoto, D. Mandrus, and E. Takayama-Muromachi, *Phys. Rev. Lett.* **99**, 196601 (2007).

[14] M. Greenblatt, *Chem. Rev.* **88**, 31 (1988).

[15] Y. Ando, K. Segawa, S. Komiya, and A. Lavrov, *Phys. Rev. Lett.* **88**, 137005 (2002).

[16] Z. Mao, T. He, M. Rosario, K. Nelson, D. Okuno, B. Ueland, I. Deac, P. Schiffer, Y. Liu, and R. Cava, *Phys. Rev. Lett.* **90**, 186601 (2003).

[17] G. Kim, Y. Q. Zhang, T. Min, H. Suh, J. H. Jang, H. Kong, J. Lee, J. Lee, T. Y. Jeon, and I. Lee, *Adv. Electron. Mater.*, 1800504 (2018).

[18] R. Pickering and R. Tilley, *J. Solid State Chem.* **16**, 247 (1976).

[19] G. Kim, B. Feng, Y.-M. Sheu, H. J. Cho, Y. Ikuhara, and H. Ohta, *ACS Appl. Electron. Mater.* **2**, 2507 (2020).

[20] J. Purans, A. Kuzmin, P. Parent, and C. Laffon, *Electrochim. Acta* **46**, 1973 (2001).

[21] J. Purans, A. Kuzmin, P. Parent, and C. Laffone, *Ionics* **4**, 101 (1998).

[22] B. Chen, J. Laverock, L. Piper, A. Preston, S. Cho, A. DeMasi, K. Smith, D. Scanlon, G. Watson, and R. Egdell, *J. Phys.: Condens. Matter* **25**, 165501 (2013).

Chapter 6. Reversible redox control of optoelectronic properties of hexagonal tungsten oxide epitaxial films

6.1 Objective

Advanced memory devices that store optoelectronic property changes would be in extremely high demand in near future because of the explosive amount of information to be processed in the upcoming fourth industrial revolution. [1-4] In this regard, TMOs can be considered as the promising candidate materials of advanced memory devices since the optoelectronic properties of TMOs can be modulated by controlling the oxygen concentration. [5-7] The valence state of TM ions is versatile in a TMO lattice due to their strong ionicity, and several TMOs show a crystallographic phase transition upon reduction or oxidation due to the difference in the ionic radius of TM ions before and after the redox reaction. Thus, controlling the oxygen concentration in metal oxides is one of the most effective ways of modulating their optoelectronic properties.

However, such redox control is difficult to apply for metal oxide epitaxial films since it induces serious damage to the crystal lattice, particularly near the film/substrate interface due to the large volume change during the redox treatment. Generally, TMO thin films are grown heteroepitaxially on oxide single crystal substrates with a lattice mismatch. [8] Therefore, the crystal lattice of the TMO thin film is highly strained at the heterointerface between the film and the substrate if the film is thin and not relaxed. If such strained crystal lattice is exposed to intense stress, the crystal lattice is easily fractured into pieces. For example, VO_2 epitaxial films grown on lattice-mismatched TiO_2 substrate breaks into tiny pieces upon insulator-to-metal transition. [9,10]

To overcome this issue and prevent damage to the crystal lattice, metal oxides exhibiting a stress-resistant crystal structure are demanded. In chapter 3, optical property change in a-WO_x with different oxygen contents was confirmed. In chapters 4-5, electron and heat transport properties of 1D-defect-tunnel-stabilized WO_x were studied. Despite the existence of many 1D defect tunnels, the functional properties have changed while maintaining the epitaxial crystal structure, indicating stress-resistant crystal structure. If 1D defect tunnels can be oriented along the *c*-axis like hexagonal tungsten oxide (h-WO_x), the optoelectronic property can be potentially controlled by reversible electrochemical redox treatment. This approach is feasible for three reasons. First, h-WO_x crystal is composed of honeycomb layers with periodic holes stacked along the *c*-axis [11,12] , and honeycomb structure is known as one of the strongest lattices against external stress. [13,14] Secondly, c-axis oriented h-WO_x crystal can be grown heteroepitaxially on (111) yttria-stabilized zirconia (YSZ) single crystal substrate. [15,16] Thus, the one-dimensional tunnels are periodically aligned along the growth direction. Lastly, YSZ substrate can be used as an oxide-ion conducting solid electrolyte, which has been utilized for the reversible electrochemical redox control of oxygen contents in $SrCoO_{2.5}$ [17-19] and $SrFeO_{2.5}$ [20].

This chapter demonstrates reversible redox control of optoelectronic properties of c-axis oriented h-WO$_x$ epitaxial films grown on (111) YSZ single crystal substrate. Upon electrochemical redox treatment at 300 °C by applying ±3 V to the YSZ solid electrolyte, the oxygen content x of h-WO$_x$ was reversibly controlled in the range of $2.93 \leq x \leq 2.99$ without inducing any damage to the crystal lattice. Simultaneously, the σ and the optical properties were reversibly engineered. The present results would be of great value in developing metal oxide epitaxial films-based electrochemical optoelectronic devices.

6.2 Film synthesis and characterizations

Highly c-axis oriented h-WO$_x$ epitaxial films were heteroeptiaxially grown on (111) YSZ substrate by PLD technique at of 500 °C under oxygen atmospheres (2 − 6 Pa). The fluence and repetition rate were set ~0.3 J cm^{-2} pulse^{-1} and 10 Hz. The growth rate was ~8.7 pm pulse^{-1} [21,22]. The thicknesses of the resultant h-WO$_x$ were determined from Pendellösung fringes (HRXRD). **Figure 6-1(a)** shows the schematic illustration of the electrochemical redox treatment. Atomic arrangement of the top view of h-WO$_3$ film is schematically shown in **Figure 6-1(b)**. First, the film surface was mechanically pressed on an Al foil (ground electrode). Then, small amount of Ag paint was pasted on the back side of the YSZ substrate, and the sample was heated at 300 °C in air. By applying a gate voltage (V_G) of −3 V to the Ag electrode for 10 min, the film was fully oxidized. (**Figure 6-1(c) upper**) Then, films were reduced by applying V_G of +3 V for 5 to 200 s (**Figure 6-1(c) lower**). The transferred electron charge (Q) was calculated by $Q = \int I(t)\, dt$, where I is current. Then, the x in WO$_x$ was measured by XPS (**Figure 6-1(d)**). The film surface was observed by AFM. The σ and S of the resultant WO_x films were measured by Van der Pauw method and steady- state method at RT. The optical transmission of the resultant films was measured using an UV-Vis-NIR and Fourier-transform infrared spectrometer (FT-IR, IRPrestige-21, Shimadzu Co.) at RT.

6.3 Results and discussion

Figure 6-2(a) (upper) shows the XPS spectrum of the as-grown epitaxial film. The XPS spectrum is composed of W^{6+} and W^{5+}, and the value of x is 2.938. **Figure 6-2(b)** (upper) shows the out-of-plane XRD pattern of as-grown h-$WO_{2.938}$ epitaxial film. An intense diffraction peak of 0002 h-WO_x is observed with 111 YSZ substrate. Pendellösung fringes near the 0002 h-$WO_{2.938}$ indicate the strong *c*-axis orientation of the film and yield the film thickness value of ~42 nm. **Figure 6-2(a) (lower)** shows the XPS spectrum of oxidized h-WO_x, which became sharper, and the W^{5+} peak almost disappeared. The as-grown film was successfully oxidized and became h-$WO_{2.993}$ (namely Oxi 1), of which the out-of-plan XRD pattern is shown in **Figure 6-2(b) (lower)**. Compare to the as-grown $WO_{2.938}$, the diffraction peak position of h-$WO_{2.993}$ shifted to smaller scattering vector side due to the *c*-axis lattice constant expansion from 0.758 to 0.769 nm. It should be noted that Pendellösung fringes are clearly observed even after the oxidation treatment, confirming that the oxidation treatment did not affect the *c*-axis oriented texture in the film. This suggests that the crystal lattice was not damaged despite the large lattice expansion.

Next, the Oxi 1 films were electrochemically reduced. 8 samples were prepared with varying chemical compositions from h-$WO_{2.987}$ to h-$WO_{2.931}$. **Figure 6-2(c)** summarizes the out-of-plane XRD patterns of the electrochemically reduced samples (linear scale). The peak position of 0002 h-WO_x is almost unchanged after the reduction from $x = 2.987$ to $x = 2.981$ while it gradually shifted to higher scattering vector side from $x = 2.981$ to $x = 2.931$, indicating that the reversible redox reaction of h-WO_x succeeded. This behavior of the *c*-axis is opposite as compared to other metal oxides, which show lattice expansion upon reduction. Presumably, the inter-atomic repulsion along *c*-axis is suppressed due to the 1D atomic defect tunnel structure. The *c*-axis lattice parameter of the electrochemically treated specimens returned to 0.762 nm, which is very close to that of the as-grown $WO_{2.938}$.

Figures 6-3(a) and **6-3(b)** show the σ and S of the electrochemically reduced h-WO_x epitaxial films measured at RT. For comparison, data for the PLD-grown h-WO_x films with various oxygen contents of x are also plotted with a grey solid line (**Figures 6-3(a)** and **6-3(b)**). The σ increases from ~0.2 (A) to ~400 S cm^{-1} (H) with decreasing x. Since $|S|$ decreased with increasing σ, n increased with decreasing x. Thus, the n of h-WO_x was successfully controlled by the electrochemical redox treatment. **Figure 6-3(c)** shows the $\sigma - T$ curves of electrochemically reduced h-WO_x epitaxial films in the range of 20 − 300 K. All films have semiconductor-like behavior of σ; where the σ increased with temperature. The slope of $\sigma - T$ curves gradually decreased with decreasing x. The E_a of the σ around RT decreased from ~212 meV (A) to ~33 meV (H) with decreasing x (**Table 6-1**). The decreasing tendency of E_a for the electrochemically reduced h-WO_x films is consistent with that of the PLD-grown h-WO$_x$ films. These results clearly suggest that n was systematically controlled by the electrochemical reduction treatment, and the crystal lattice of h-WO$_x$ film was not destroyed.

Table 6-1. Transmission (*Trans.*) at 1.5 μm and the E_a of the electrochemically reduced/oxidized h-WO$_x$ films.

Sample	**x in WO$_x$**	***Trans.* at 1.5 μm (%)**	**E_a (meV)**
A	2.987	49.8	212.3
B	2.986	52.0	203.7
C	2.981	46.7	108.5
D	2.960	44.2	74.0
E	2.954	43.4	68.1
F	2.935	41.8	71.7
G	2.933	38.3	35.8
H	2.931	35.4	33.3
Oxi 1	2.993	69.3	ND
Oxi 2	2.988	61.9	ND

Figure 6-4(a) shows the optical transmission spectra of the h-WO$_x$ epitaxial films with various reduction states (as-oxidized: Oxi 1, A, E, and G) from the electrochemical reduction treatments. The spectra of as-grown sample and (111) YSZ substrate are also plotted for comparison. Although the bandgap of YSZ is ~4 eV, the optical transmission of (111) YSZ substrate is only ~75% in the range of 0.4 – 6 μm in wavelength; reflection of YSZ in the range of 0.4 – 6 μm in wavelength is large (~23 %) due to its high refractive index. Compared to the transmission spectrum of YSZ substrate, the Oxi 1 sample shows slightly lower transmission due to an absorption peaking around 1.5 μm. The absorption peak intensity gradually increased with oxygen reduction, indicating free carrier absorption. Finally, the optical transmission spectrum of the reduced sample G became similar to that of the as-grown sample. **Figure 6-4(b)** plots change in the transmission at 1.5 μm as a function of x in WO_x. For comparison, data for the PLD-grown h-WO_x films is also plotted with a grey solid line. The transmission increased with oxidation and decreased with reduction. The control in the optical transmission control at 1.5 μm is clearly demonstrated in the range of 35 − 70%.

Finally, the electrochemical redox treatment was repeated to check the cyclability. **Figures 6-5(a)** and **6-5(b)** show the σ and optical transmission at 1.5 μm of the redox-treated h-WO_x epitaxial films. Upon reversible electrochemical redox treatment, the σ was controlled from ~300 to ~0.1 S cm^{-1}, and the optical transmission at 1.5 μm is controlled in the range of 35 − 70%. Also, surface morphology was not changed during electrochemical redox treatment while keeping the root mean square roughness less than 0.5 nm (**Figure 6-6**). These results indicate an excellent cyclability and stability. From these results, electrochemically redox treatments did not cause serious structural damage to the crystalline lattice of h-WO_x with stress-resistant honeycomb lattice. The optoelectronic properties of h-WO_x were repeatedly controlled electrochemically.

6.4 Conclusion

This chapter demonstrated reversible redox control of the optoelectronic properties in hexagonal tungsten oxide (h-WO_x) epitaxial films with honeycomb structure. Highly c-axis oriented h-WO_x epitaxial films were fabricated on (111) YSZ single crystal substrate. Upon the electrochemical redox treatment, the oxygen content x in h-WO_x was reversibly controlled in the range of $2.93 \leq x \leq 2.99$ without inducing damage to the crystal lattice. Simultaneously, the σ was controlled from ~400 S cm^{-1} to an insulator, and the optical transmission at 1.5 μm was controlled between 35% and 70%. These results suggest that electrochromic or optoelectronic application is also valid in epitaxial h-WO_x films.

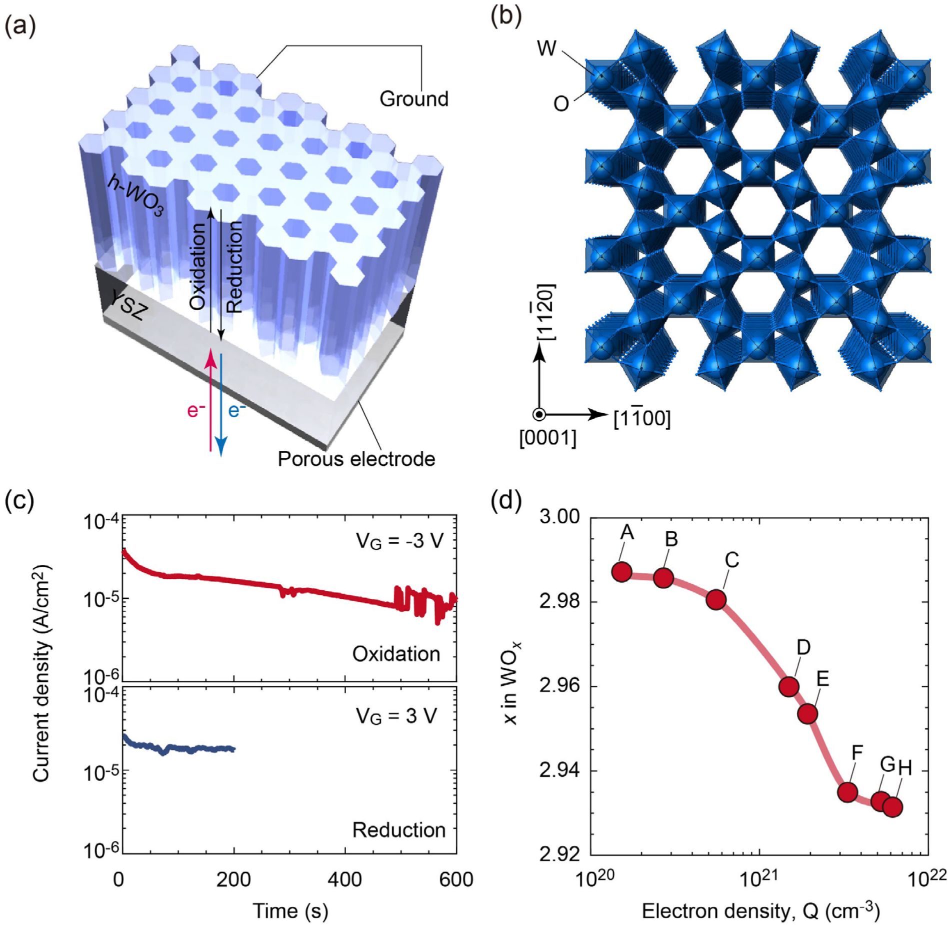

Figure 6-1. Solid-state electrochemical redox treatment of a h-WO$_x$ epitaxial film. (a) Schematic illustration of the solid-state electrochemical cell composed of h-WO$_3$/YSZ substrate. (b) Honeycomb lattice of h-WO$_3$ crystal with periodic holes along the *c*-axis. (c) Change in the current density through the h-WO$_3$/YSZ bilayer at 300 °C in air. (d) Change in the oxygen content *x* in h-WO$_x$ as a function of the current density during the electrochemical reduction treatment.

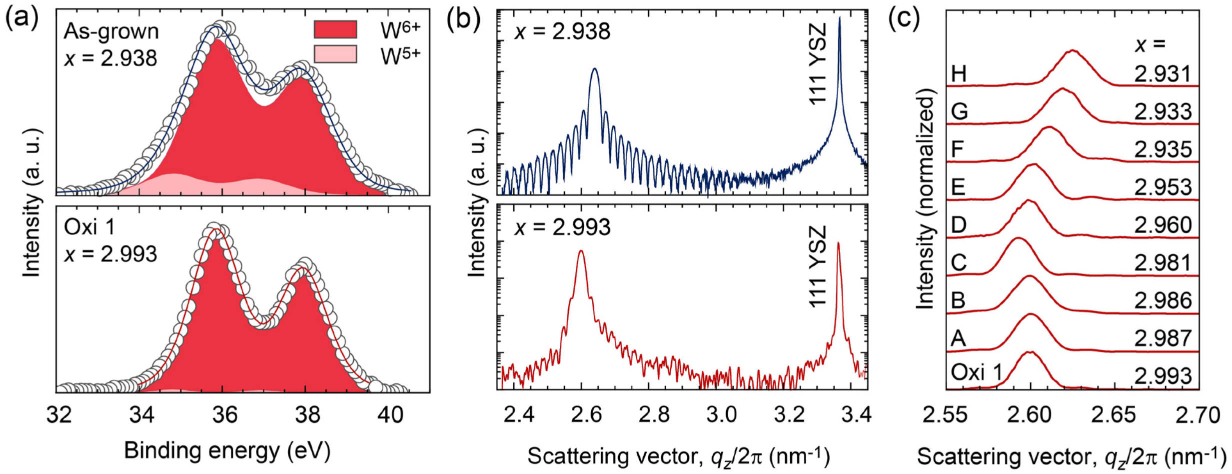

Figure 6-2. XPS and cross-plane crystal lattice of the h-WO$_x$ epitaxial films. (a) XPS spectra of (upper) as-grown and (lower) electrochemically oxidized h-WO$_x$ films. The x values in WO$_x$ were determined as 2.938 (as-grown) and 2.993 (oxidized). (b) Out-of-plane XRD patterns of (upper) as-grown and (lower) electrochemically oxidized h-WO$_x$ films. Intense diffraction peak of 0002 h-WO$_x$ is seen together with 111 YSZ both as-grown and oxidized films. Further, Pendellösung fringes are seen around the diffraction peak of 0002 h-WO$_x$, indicating strong orientation of the films. (c) Change in the out-of-plane XRD patterns of 0002 h-WO$_x$ (linear scale) with x in the electrochemically reduced WO$_x$ films.

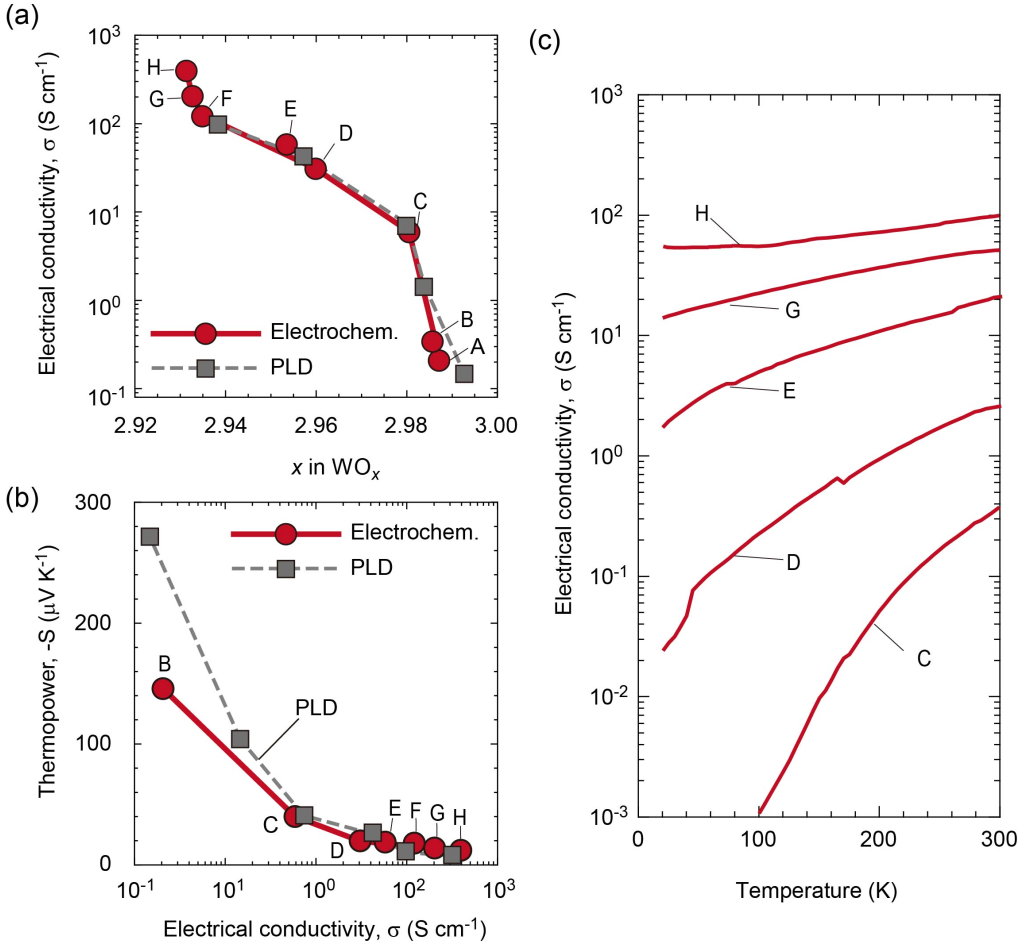

Figure 6-3. **Electronic transport properties of the h-WO$_x$ epitaxial films.** (a) σ (RT), (b) S (RT), and (c) temperature dependence of the σ for the electrochemically reduced WO$_x$ films. Gray solid lines in (a) and (b) indicate the σ and the S of the h-WO$_x$ epitaxial films by the PLD method with modulated oxygen pressure during the film growth, respectively. The electrochemical redox results reproduce the PLD data very well, suggesting the crystal lattice of h-WO$_x$ film was not destroyed during the redox treatment. (c) Temperature dependence of σ of the h-WO$_x$ films. The σ is systematically controlled.

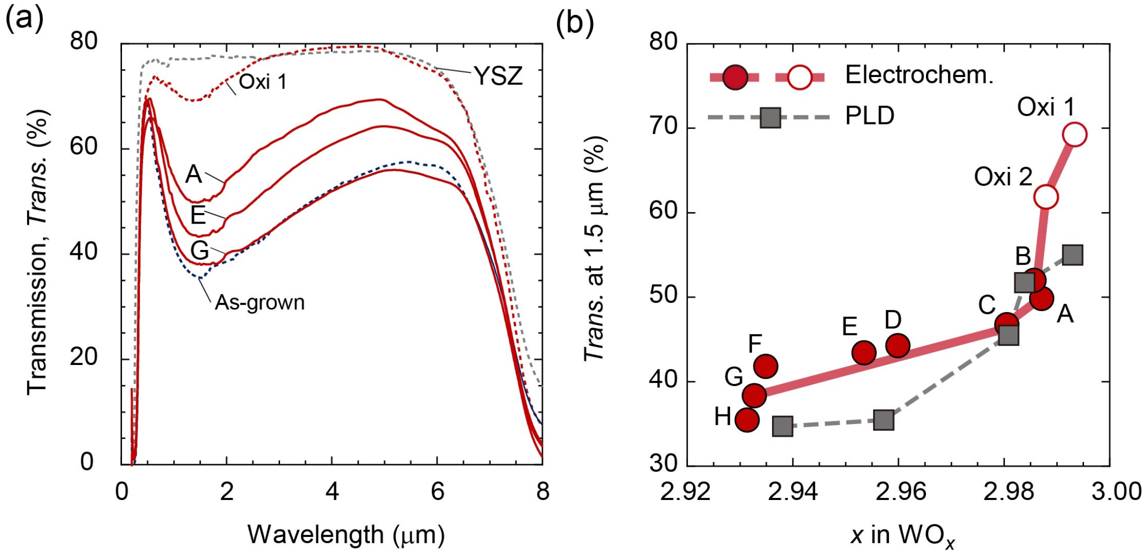

Figure 6-4. Optical properties the h-WO$_x$ epitaxial films. (a) Optical transmission spectra of the *c*-axis oriented h-WO$_x$ film epitaxially grown on (111) YSZ substrate after the electrochemical reduction treatment. Optical transmission spectrum of YSZ substrate and as-grown h-WO$_x$ film are shown for comparison. There is a tiny free electron absorption peaking around 1.5 μm in the fully oxidized film (Oxi 1). The absorption band increases with increasing the degree of reduction, and it approaches that of the as-grown sample. (b) Optical transmission at 1.5 μm as a function of x in WO$_x$.

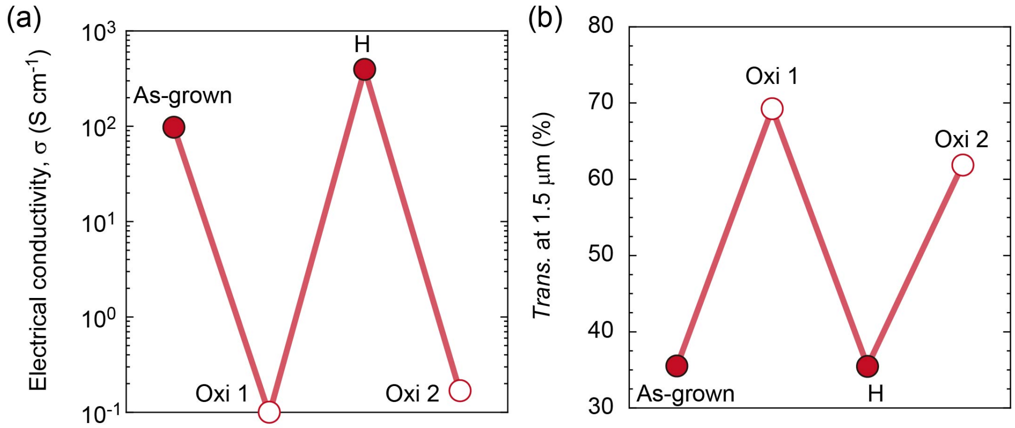

Figure 6-5. Reversible redox modulation of optoelectronic properties of the h-WO$_x$ epitaxial films. (a) σ and (b) optical transmission at 1.5 μm for the h-WO$_x$ epitaxial films. Upon reversible electrochemical redox treatment, the σ is controlled from ~100 S cm^{-1} to ~0.1 S cm^{-1}, and the optical transmission at 1.5 μm is controlled in the range of 35 − 70%.

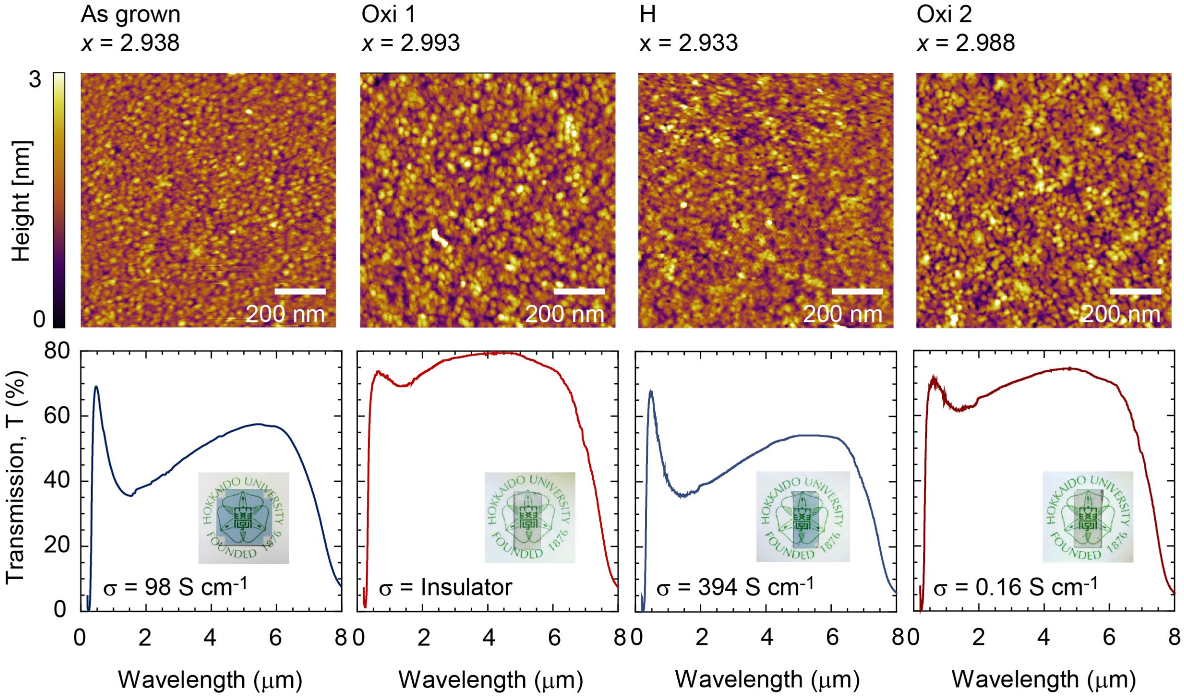

Figure 6-6. Cyclability in the optical property and surface morphology of the h-WO$_x$ epitaxial film. Changes in the optical property and surface morphology of the h-WO$_x$ epitaxial film after repeated electrochemical redox treatments. (From left to right: as-grown, 1st oxidized, 1st reduced, and 2nd oxidized)

References

[1] C. S. Hwang and B. Dieny, *MRS Bull.* **43**, 330 (2018).

[2] W. Huang, L. Yin, F. Wang, R. Cheng, Z. Wang, M. G. Sendeku, J. Wang, N. Li, Y. Yao, and X. Yang, *Adv. Funct. Mater.* **29**, 1902890 (2019).

[3] H. Tan, G. Liu, X. Zhu, H. Yang, B. Chen, X. Chen, J. Shang, W. D. Lu, Y. Wu, and R. W. Li, *Adv. Mater.* **27**, 2797 (2015).

[4] S. Lei, F. Wen, B. Li, Q. Wang, Y. Huang, Y. Gong, Y. He, P. Dong, J. Bellah, and A. George, *Nano Lett.* **15**, 259 (2015).

[5] G. Kim, H. J. Cho, Y.-M. Sheu, and H. Ohta, *J. Phys. Chem. C* **123**, 15419 (2019).

[6] D. Liu, C. Wang, Y. Yu, B.-H. Zhao, W. Wang, Y. Du, and B. Zhang, *Chem* **5**, 376 (2019).

[7] J. S. Lim, J. Lee, B. J. Lee, Y.-J. Kim, H.-S. Park, J. Suh, H.-H. Nahm, S.-W. Kim, B.-G. Cho, and T. Y. Koo, *Sci. Adv.* **6**, eabb8553 (2020).

[8] A. Biswas, C.-H. Yang, R. Ramesh, and Y. H. Jeong, *Prog. Surf. Sci.* **92**, 117 (2017).

[9] K. Nagashima, T. Yanagida, H. Tanaka, and T. Kawai, *Phys. Rev. B* **74**, 172106 (2006).

[10] J. Cao, E. Ertekin, V. Srinivasan, W. Fan, S. Huang, H. Zheng, J. Yim, D. Khanal, D. Ogletree, and J. Grossman, *Nat. Nanotechnol.* **4**, 732 (2009).

[11] P. Krüger, I. Koutiri, and S. Bourgeois, *Phys. Rev. B* **86**, 224102 (2012).

[12] Y. Lee, T. Lee, and A. Soon, *J. Phys. Chem. C* **122**, 21644 (2018).

[13] V. Palermo, I. A. Kinloch, S. Ligi, and N. M. Pugno, *Adv. Mater.* **28**, 6232 (2016).

[14] J. Han, N. M. Pugno, and S. Ryu, *Nanoscale* **7**, 15672 (2015).

[15] T. Soma, K. Yoshimatsu, and A. Ohtomo, *Appl. Phys. Express* **9**, 075801 (2016).

[16] P. M. Wu, S. Ishii, K. Tanabe, K. Munakata, R. Hammond, K. Tokiwa, T. Geballe, and M. Beasley, *Appl. Phys. Lett.* **106**, 042602 (2015).

[17] Q. Yang, H. J. Cho, H. Jeen, and H. Ohta, *Advanced Materials Interfaces* **6**, 1901260 (2019).

[18] Q. Lu and B. Yildiz, *Nano Lett.* **16**, 1186 (2016).

[19] Q. Lu, Y. Chen, H. Bluhm, and B. Yildiz, *J. Phys. Chem. C* **120**, 24148 (2016).

[20] Q. Yang, H. J. Cho, H. Jeen, and H. Ohta, *J. Appl. Phys.* **129**, 215303 (2021).

[21] G. Kim, B. Feng, Y.-M. Sheu, H. J. Cho, Y. Ikuhara, and H. Ohta, *ACS Appl. Electron. Mater.* **2**, 2507 (2020).

[22] G. Kim, B. Feng, S. Ryu, H. J. Cho, H. Jeen, Y. Ikuhara, and H. Ohta, *ACS Appl. Mater. Interfaces* **13**, 6864 (2021).

Chapter 7. Summary

This doctoral research was concerned with clarifying the electron and heat transport properties of WO_x with various atomic arrangements for designing better thermal management and optoelectronic materials. The approach was introducing oxygen vacancies to build a unique WO_x structure without changing the atomic constituents, which may be more economical and simpler for manipulating its functional properties and manufacturing functional devices.

At first, to clearly understand the role of oxygen contents in the functional properties of WO_x, the electrical, optical, and thermal properties of a-WO_x were systematically investigated with varying x from 2.982 to 2.511, which eliminate the effect of structural changes. Optoelectrical properties changed from transparent insulator to dark black semiconductor with increasing W^{5+} concentration, while the κ was slightly enhanced from ~0.9 W m^{-1} K^{-1} to ~1.6 W m^{-1} K^{-1} due to carrier electrons. However, the κ remained very low. As the W^{4+} valence state became dominant, the ρ slightly increased, whereas the low visible transmission was maintained. The results showed that implies the electrons in the W^{5+} valence state, especially in the range of $2.64 < x < 3$, serves as the major factor for optoelectrical properties of WO_x.

The assessment of functional properties of a-WO_x showed that optoelectronic properties can be easily controlled while its κ is difficult to control due to the low vibrational density of states. In order to engineer both heat and electron transport properties, crystallized WO_x films with various atomic arrangement are required to enhance the vibrational density of states. Therefore, the research approach extended to nanostructuring concept such as introducing point defect (0D), defect tunnel (1D), and layer (2D) to simultaneously realize high electron conduction and low heat conduction. Crystallographic analyses revealed that 1D atomic defect tunnels are formed randomly in epitaxial WO_x films on (001) $LaAlO_3$ substrates with introducing oxygen vacancies. The x varied from 2.977 to 2.787, the cross-plane κ of the WO_x films significantly decreased from ~7 W m^{-1} K^{-1} to ~2 W m^{-1} K^{-1} due to phonon scattering from the tunnel while the σ drastically increased from 0.06 S cm^{-1} to ~1500 S cm^{-1} because of an increase in the carrier electrons. High electron conduction and low heat conduction coexisted in these WO_x structures when $x < 2.9$.

The potential of the 1D defect tunnels in WO_x films was investigated further by aligning their long-axis of rectangular grain along the same direction, which would result in different σ along and across the tunnels. Highly oriented 1D defect tunnels were stabilized in WO_x films on (110) LaAlO3 substrates. The crystallographic analyses of the WO_x films revealed that highly dense atomic defect tunnels were aligned one-dimensionally along [001] $LaAlO_3$ single crystal substrate. The anisotropic σ was obtained when x was 2.778, where the σ along the 1D atomic defect tunnels was ~5 times larger than that across the tunnels since the electrons are scattered by 1D defect tunnels.

Despite introducing a high concentration of 1D defect tunnels in the WO_x, the epitaxial structure was maintained. In other words, this structure is highly durable and could perhaps sustain high external lattice strain induced during electrochemical redox treatments, which can reversibly modulate the optoelectronic properties of h-WO_x. h-WO_x, which exhibits the 1D tunnels aligned perpendicular to the surface, was stabilized on (111) YSZ substrates, which were utilized as the solid electrolyte. Upon electrochemical redox treatment at 300 °C with applying ±3 V to the YSZ solid electrolyte, the oxygen content x of h-WO_x was reversibly controlled in the range of $2.93 \leq x \leq 2.99$ without inducing physical damage to the crystal lattice. Simultaneously, the σ was controlled from ~400 S cm^{-1} to an insulator, and the optical transmission at 1.5 μm was controlled in the range of 35 − 70%. This shows that optoelectronic applications of WO_x, which is mainly achieved in a-WO_x, can also be realized in c-WO_x.

The novel contributions from this research will establish a solid foundation for understanding the role of atomic structure on the transport properties of TMOs, which will be of great value for the design concept of thermal management materials and functional optoelectronics devices.

Acknowledgments

The research was conducted under the supervision of professor Hiromichi Ohta at the Research Institute for Electronic Science (RIES) at Hokkaido University from October 2018 to September 2021.

Three years seem to have passed quickly. When I first came here as a research student, everything was awkward and foreign to me, but it has become one of the most familiar places to me now. The warm and passionate teaching of Prof. Hiromichi Ohta was crucial in this regard, and I would like to express my gratitude for his guidance, support, and encouragement. He was always willing to take the time to give me advice and gave me directions on how to address the problems I faced. I still have a lot of rooms for improvements, but I learned the right attitude as a researcher from him, and he has grown me to have a wide perspective. I was so lucky to get the chance to study here, and his teaching definitely provided a stepping stone forward in my life.

I would like to thank Prof. Yuichi Ikuhara (U. Tokyo) and Prof. Bin Feng (U. Tokyo) for spending valuable time to perform the STEM measurement. I would also gratefully appreciate Prof. Yu-Miin Sheu (NYCU), Prof. Tsukasa Katayama (Hokkaido U.), and Prof. Hai Jun Cho (Hokkaido U.) for scientific discussions. In addition, I would like to thank Prof. Isao Tanaka (Kyoto U.) for performing Phonon dispersion calculations. I also would like to give my special thanks to Prof. Hyoungjeen Jeen (Pusan Nat'l U.), who was my previous supervisor. He gave me the opportunity to be here and constantly cheered me up until now. They provided me a lot of advice and thorough guidance during this research, and I couldn't have done my research without their help.

Also, I owe the laboratory members a lot for their help: I really owe you a lot. Dr. Yuqiao Zhang (Professor at Jiangsu U.), Dr. Takaki Onozato (SONY), Dr. Mian Wei, Ms. Doudou Liang (Ph. D. candidate, USTB), Ms. Qian Yang (Ph. D. candidate), Mr. Yuzhang Wu (Ph. D. candidate), Mr. Binjie Chen (Ph. D. candidate), Mr. Yugo Takashima (Honda), Mr. Lizhikun Gong (Ph. D. candidate, IST, Hokkaido Univ.), and all other past and present lab members study, especially, Dr. Onozato and Dr. Zhang for teaching me a lot about the basic handling of equipment in the laboratory.

I thank my boyfriend, sister's family, brother, and friends so much for always encouraging me not to give up. Finally, I would like to express sincere gratitude from the between of my heart to my parents for all they do. They always believe in me and give me endless support. I thank them for always standing by my side and all your sacrifices. I can only do my best in all aspects of my life and hope one day they no longer have to worry about me.

I am grateful to the financial support during my Ph.D. program provided by the Japan Society for the Promotion of Science (JSPS, 2020.04-2021.09) and Asahi Glass Foundation Scholarship (2019.04-2020.03).

Gowoon Kim

Lists of publications

Papers related to the given dissertation

[1] G. Kim*, H. Cho, and H. Ohta*, “Reversible Redox Control of Optoelectronic Properties of Hexagonal Tungsten Oxide Epitaxial Films Grown on YSZ Solid Electrolyte”, *ACS Appl. Electron. Mater.* XX, XXX-XXX (2021)

[2] G. Kim*, B. Feng, S. Ryu, H. J. Cho, H. Jeen, Y. Ikuhara, and H. Ohta*, “Anisotropic electrical conductivity of oxygen-deficient tungsten oxide films with epitaxially stabilized 1D atomic defect tunnels”, *ACS Appl. Mater. Interfaces* **13**, 6864-6869 (2021)

[3] G. Kim*, B. Feng. Y-M. Sheu, H. Cho, Y. Ikuhara and H. Ohta*, “Coexistence of High Electron Conduction and Low Heat Conduction in Tungsten Oxide Epitaxial Film with 1D Atomic Defect Tunnels” *ACS Appl. Electron. Mater.* **2**, 2507-2513 (2020)

[4] G. Kim, H. Cho, Y. Sheu and H. Ohta*, “Electrical, optical and thermal transport properties of oxygen deficient amorphous WO_x ($2.5 < x < 3$) films”, *J. Phys. Chem. C* **123** 15419 (2019) cover image

Other papers

[1] H. Kong, G. Kim, J. Lee, J. Cho, and H. Jeen*, “Effect of thermal annealing on nitrogen implanted epitaxial Fe films”, *Curr. Appl. Phys.* **24**, 7-11 (2021)

[2] Q. Yang, J. Lee, B. Feng, Y. Ikuhara, G. Kim, H. Cho, H. Jeen*, and H. Ohta*, “Unusually large thermopower change from +330 $\mu V\ K^{-1}$ to -185 $\mu V\ K^{-1}$ of brownmillerite $SrCoO_{2.5}$”, *ACS Appl. Electron. Matter.* **2**, 2250-3356 (2020)

[3] H. Cho*, K. Sato, M. Wei, G. Kim, and H. Ohta*, Effect of lattice distortions on the

electron and thermal transport properties of transparent oxide semiconductor $Ba_{1-x}Sr_xSnO_3$ solid solution films", *J. Appl. Phys.* **127**, 115701 (2020). Editor's pick

[4] A. V. Sanchela, M. Wei, J. Lee, <u>G. Kim</u>, H. Jeen, B. Feng, Y. Ikuhara, H. J. Cho, and H. Ohta, "Buffer layer-less fabrication of high-mobility transparent oxide semiconductor, La-doped $BaSnO_3$", *J. Mater. Chem. C* **7** 5797. (2019)

[5] H. Cho, <u>G. Kim</u>, T. Onozato, H. Jeen and H. Ohta, "Thermal conductivity tensor of NbO_2", *Int. J. Heat Mass Transf.* **137** 263 (2019)

[6] <u>G. Kim</u>, E. Ahn, J. Lee, Y. Zang, J. Jang, H. Seo, T. Jeon, J. Cho, H. Ohta and H. Jeen, "Extremely light carrier effective mass in a distorted simple metal oxide", *Adv. Electron. Mater.* **5**, 1800504 (2019).

[7] A. V. Sanchela, M. Wei, H. Zensyo, B. Feng, J. Lee, <u>G. Kim</u>, H. Jeen, Y. Ikuhara, and H. Ohta, "Large thickness dependence of the carrier mobility in a transparent oxide semiconductor, La-doped $BaSnO_3$", *Appl. Phys. Lett.* **112***,* 232102 (2018).

List of presentations

[1] The 82nd JSAP Autumn Meeting, Online, 10th-13th, Sep. 2021 (Oral presentation)

Title: Reversible Redox Control of Optoelectronic Properties of Hexagonal Tungsten Oxide Epitaxial Films Grown on YSZ Solid Electrolyte

[2] 新学術・機能コア若手コラボツア, Online, 18th, Jun. 2021 (Oral presentation)

Title: Tungsten Oxide Epitaxial Films with 1D Atomic Tunnels — Structure and optical-electrical-thermal transport properties —

[3] ICC8 Virtual, Online, 25th–30nd, Apr. 2021 (Oral presentation)

Title: Thermoelectric properties of 1D atomic defect tunnels stabilized tungsten oxide epitaxial film

[4] The 68th JSAP Spring Meeting 2021, Online, 16th–19nd, Mar. 2021 (Oral presentation)

Title: Thermoelectric Properties of Tungsten Oxide Films with 1D Atomic Defect Tunnels

[5] 2021 Electronic Materials and Applications (EMA 2021), Online, 19th–22nd, Jan. 2021(Oral presentation)

Title: Phono-Glass and Electron-Crystal Behavior of WO_x films containing 1D Atomic Defect Tunnels

[6] The 56th Japan Society of Applied Physics Hokkaido Branch Meeting, Online, 9th–11th, Jan. 2021 (Oral presentation)

Title: Anisotropy in the electrical conductivity of oxygen deficient WO_x with 1D atomic defect tunnels

[7] The 21st RIES-Hokudai International Symposium 間 [ma], Online, 10th–11th, Dec. 2020 (Poster presentation)

Title: Large Anisotropy of Electron Transport in Oxygen Deficient Tungsten Oxide Epitaxial Films with 1D Atomic Defect Tunnels

[8] 第14回物性科学領域横断研究会, Online, 4th–5th, Dec. 2020 (Oral presentation)

Title: Anisotropic electron transport of 1D atomic defect tunnels stabilized in epitaxial tungsten oxide films

[9] 2020 Meeting of the Ceramics Society of Japan Tohoku-Hokkaido Branch, Online, 13th–14th, Nov. 2020 (Oral presentation)

Title: Large Anisotropy of Electron Transport in Oxygen Deficient Tungsten Oxide Epitaxial Films with 1D Atomic Defect Tunnels

[10] The 17th Thin Film materials & Devices Meeting, Online, 5th–6th, Nov. 2020 (Poster presentation)

Title: Heat and Electron Transports of 1D Atomic Defect Tunnels Stabilized in WO_x Films

[11] Pacific Rim Meeting on Electrochemical and Solid-State Science (PRiME 2020) Online, 4th–9th, Oct. 2020 (Oral presentation)

Title: High Electron and Low Heat Transports of 1D Atomic Defect Tunnels Stabilized in Tungsten Oxide Epitaxial Films

[12] The 67th JSAP Spring Meeting 2020 (canceled, the presentation has been established) Sophia University, Tokyo, 12nd–15th Mar. 2020

Title: Phonon Glass Electron Crystal behavior in Magneli tungsten oxide

[13] The 55th Japan Society of Applied Physics Hokkaido Branch Meeting, Hokkaido University, 11st–12nd, Jan. 2020 (Oral presentation)

Title: Anomalously low thermal conductivity of Magneli WO_x films showing high electrical conductivity

[14] The 3rd Workshop on Functional Materials Science, Sapporo, Japan, 18th–20th, Dec. 2019 (Poster presentation)

Title: Systematic Clarification of Electron and Heat Transports in Oxygen Deficient WO_x

[15] 2019 MRS Fall Meeting & Exhibit, Boston, USA, 1st–6th, Dec. 2019 (Poster presentation)

Title: Electrical, optical and thermal transport properties of oxygen deficient amorphous WO_x ($2.5 < x < 3$) films

[16] Transparent Oxide and Related Materials for Electronics and Optics (TOEO)-11 Nara, Japan, 7th–9th, Oct. 2019 (Poster presentation)

Title: Systematic Clarification of Electron and Heat Transports in Oxygen Deficient WO_x <Comparison between Amorphous Films and Epitaxial Films>

[17] The 80th JSAP Autumn Meeting 2019, Sapporo, Japan, 18th–21st, Sep. 2019 (Oral presentation)

Title: Electron and hear transports of oxygen deficient WO_x ($2.8 < x < 3$) epitaxial films

[18] The 80th JSAP Autumn Meeting 2019, Sapporo, Japan, 18th–21st, Sep. 2019 (Oral

presentation)

Title: Optical, Electrical and Thermal Transport of Amorphous WO_x ($2.5 < x < 3$) Films

[19] The 19th RIES-HOKUDAI International Symposium 組[So], Jozankei View Hotel, Sapporo, 11th–12th, Dec. 2018 (Poster presentation)

Title: Extremely light carrier effective mass in a distorted simple metal oxide, NbO_2

[20] The International Conference on Electronic Materials and Nanotechnology for Green Environment (ENGE 2018), Jeju, Korea, 11th–14th Nov. 2018 (Oral presentation)

Title: Facile path for electron hopping in epitaxial NbO_2 thin films

[21] The 2nd workshop on Functional Material Science, Busan, Korea, 22nd–23rd Oct. 2018 (Oral presentation)

Title: A facile path for electron hopping in NbO_2

List of awards

[1] Poster Award "Large Anisotropy of Electron Transport in Oxygen Deficient Tungsten Oxide Epitaxial Films with 1D Atomic Defect Tunnels (P59)", The 21st RIES-Hokudai International Symposium 間 [ma], online, 10th-11th, Dec. 10-11, 2020 (poster).

[2] Excellent Presentation Award, "Heat and electron transports of 1D atomic defect tunnels stabilized in tungsten oxide epitaxial films (1A03)", 2020 Meeting of the Ceramics Society of Japan Tohoku-Hokkaido Branch, online, 13th-14th, Nov. 2020 (Oral).

[3] Best Poster Award Nomination, "Electrical, optical and thermal transport properties of oxygen deficient amorphous WO_x ($2.5 < x < 3$) films", 2019 MRS Fall Meeting & Exhibit, Boston, MA, 1st-6th, Dec. 1-6, 2019 (Poster).